Monthly Notices
of the
ROYAL ASTRONOMICAL SOCIETY

MNRAS **449,** 1177–1214 (2015) doi:10.1093/mnras/stv151

Evolutionary stellar population synthesis with MILES – II. Scaled-solar and α-enhanced models

A. Vazdekis,[1,2]⋆ P. Coelho,[3] S. Cassisi,[4] E. Ricciardelli,[5] J. Falcón-Barroso,[1,2] P. Sánchez-Blázquez,[6] F. La Barbera,[7] M. A. Beasley[1,2] and A. Pietrinferni[4]

[1]*Instituto de Astrofísica de Canarias (IAC), E-38200 La Laguna, Tenerife, Spain*
[2]*Departamento de Astrofísica, Universidad de La Laguna, E-38205 Tenerife, Spain*
[3]*Instituto de Astronomia, Geofísica e Ciências Atmosféricas, Univ. de São Paulo, Rua do Matão 1226, 05508-090 São Paulo, Brazil*
[4]*INAF-Osservatorio Astronomico di Collurania, via Mentore Maggini, I-64100 Teramo, Italy*
[5]*Departament d'Astronomia i Astrofísica, Universitat de Valencia, C/Dr. Moliner 50, E-46100 Burjassot, Valencia, Spain*
[6]*Universidad Autónoma de Madrid, Departamento de Física Teórica, E-28049 Cantoblanco, Madrid, Spain*
[7]*INAF – Osservatorio Astronomico di Capodimonte, I-80131 Napoli, Italy*

Accepted 2015 January 20. Received 2015 January 20; in original form 2014 December 12

ABSTRACT

We present models that predict spectra of old- and intermediate-aged stellar populations at 2.51 Å (FWHM) with varying [α/Fe] abundance. The models are based on the MILES library and on corrections from theoretical stellar spectra. The models employ recent [Mg/Fe] determinations for the MILES stars and BaSTI scaled-solar and α-enhanced isochrones. We compute models for a suite of initial mass function (IMF) shapes and slopes, covering a wide age/metallicity range. Using BaSTI, we also compute 'base models' matching the Galactic abundance pattern. We confirm that the α-enhanced models show a flux excess with respect to the scaled-solar models blueward ∼4500 Å, which increases with age and metallicity. We also confirm that both [MgFe] and [MgFe]′ indices are [α/Fe]-insensitive. We show that the sensitivity of the higher order Balmer lines to [α/Fe] resides in their pseudo-continua, with narrower index definitions yielding lower sensitivity. We confirm that the α-enhanced models yield bluer (redder) colours in the blue (red) spectral range. To match optical colours of massive galaxies, we require both α-enhancement and a bottom-heavy IMF. The comparison of globular cluster line-strengths with our predictions match the [Mg/Fe] determinations from their individual stars. We obtain good fits to both full spectra and indices of galaxies with varying [α/Fe]. Using thousands of SDSS galaxy spectra, we obtain a linear relation between a proxy for the abundance, $[Z_{Mg}/Z_{Fe}]_{SS(BaSTI)}$, using solely scaled-solar models and the [Mg/Fe] derived with models with varying abundance ($[Mg/Fe] = 0.59[Z_{Mg}/Z_{Fe}]_{SS(BaSTI)}$). Finally, we provide a user-friendly, web-based facility, which allows composite populations with varying IMF and [α/Fe].

Key words: stars: fundamental parameters – globular clusters: general – galaxies: abundances – galaxies: elliptical and lenticular, cD – galaxies: evolution – galaxies: stellar content.

1 INTRODUCTION

The integrated light emitted by stellar systems such as star clusters and galaxies provide us with the necessary information to understand their fundamental properties, and how these properties arise and evolve. From observables like colours, line-strength indices or full spectral energy distributions (SEDs), we can derive the star formation history (SFH), mean age, metal content, abundance pattern, stellar initial mass function (IMF) and dust properties of these systems.

For a quantitative study of their properties, we require stellar population synthesis models. The method consists in comparing the observables to the predictions of these models (e.g. Tinsley 1980). Stellar population synthesis models are also employed in other type of studies, e.g. to provide the necessary templates for kinematic or redshift measurement, or to determine galaxy stellar masses via mass-to-light ratios (M/L), just to mention two

⋆E-mail: vazdekis@iac.es

applications. Evolutionary population synthesis models, which are regarded nowadays as standard, take into account the contributions of all possible stars, in proportions prescribed by stellar evolution theory (e.g. Tinsley 1980). These models combine at least three main ingredients that determine the quality of the predictions: a prescription for the IMF, a set of stellar evolutionary isochrones and stellar spectral libraries to predict a variety of observables in several bands such as fluxes, colours, M/L or low-resolution spectra (e.g. Bruzual 1983; Arimoto & Yoshii 1986; Guiderdoni & Rocca-Volmerange 1987; Bressan, Chiosi & Fagotto 1994; Fritze-Von Alvensleben & Gerhard 1994; Worthey 1994; Vazdekis et al. 1996; Fioc & Rocca-Volmerange 1997; Kodama & Arimoto 1997; Maraston 1998; Leitherer et al. 1999; Maraston 2005; Conroy & Gunn 2010) and also surface brightness fluctuations (e.g. Liu, Charlot & Graham 2000; Blakeslee, Vazdekis & Ajhar 2001; Liu, Graham & Charlot 2002; Cantiello et al. 2003).

In the last two decades, important advances have been made in the field with the aid of models that predict absorption line-strength indices for single-age, single-metallicity stellar populations (SSPs; e.g. Worthey 1994) and more complex stellar populations, built as compositions of SSPs (e.g. Vazdekis et al. 1996). These models employ fitting functions that relate measured line-strength indices to the atmospheric parameters ($T_{\rm eff}$, $\log g$, [Fe/H]) of the library stars. The most widely used fitting functions are those obtained with the Lick/IDS stellar library (Burstein et al. 1984; Faber et al. 1985; Gorgas et al. 1993; Worthey et al. 1994; Worthey & Ottaviani 1997). The Lick/IDS system comprises definitions of 25 absorption line-strengths in the optical spectral range with varying, low, resolutions (FWHM $>$ 8–11 Å). There are alternative fitting functions in the optical range (e.g. Buzzoni 1995; Gorgas et al. 1999; Schiavon 2007; Tantalo, Chiosi & Piovan 2007) and in other spectral ranges (e.g. Cenarro et al. 2002; Mármol-Queraltó et al. 2008; Cenarro et al. 2009). The majority of these model predictions are implicitly based on a scaled-solar[1] heavy element mixture around solar metallicity. This is due to the fact that these libraries are composed of stars that are imprinted with the abundance pattern of the solar neighbourhood, as a result of their experienced SFH. Such types of predictions have also been developed in other spectral ranges (e.g. Saglia et al. 2002; Vazdekis et al. 2003; Cenarro et al. 2009).

There are a variety of approaches that have been employed in the literature to extract the information contained in spectral line indices. The most popular method is to build key diagnostic model grids by plotting an age-sensitive (e.g. Hβ) versus a metallicity-sensitive indicator (e.g. Mgb, $\langle$Fe$\rangle$), to estimate these parameters (e.g. Rose 1994; Worthey 1994; Vazdekis et al. 1996; Kuntschner et al. 2006; Schiavon 2007), including estimations of the abundance ratios of individual elements (e.g. Trager et al. 2000; Thomas, Maraston & Bender 2003a; Schiavon 2007). There are other methods that employ as many Lick indices as possible and simultaneously fit them in a χ^2 sense (e.g. Vazdekis et al. 1997; Proctor, Forbes & Beasley 2004). An alternative method is the use of principal component analysis (e.g. Covino, Galletti & Pasinetti 1995; Wild et al. 2009).

Unlike colours, these indices are insensitive to the effects of dust extinction (e.g. MacArthur 2005) and allow us to study the age (as a proxy for the SFH) and metallicity, [M/H] (i.e. the total metal content). In addition, they also allow us to study the abundances of various elements from the strengths of these absorption lines (e.g. Rose 1985, 1994; Trager et al. 1998, 2000; Proctor & Sansom 2002; Sánchez-Blázquez et al. 2003; Carretero et al. 2004; Thomas et al. 2005; Schiavon 2007; Conroy & van Dokkum 2012b). In fact, one of the most important results has been the finding that massive early-type galaxies (ETGs) show an overabundance of [Mg/Fe] (e.g. Peletier 1989; Worthey, Faber & González 1992). Such departure from the solar abundance pattern is generally attributed to short formation time-scales ($<$1 Gyr) for the bulk of their stellar populations (see the reviews of e.g. Trager et al. 1998, 2000; Renzini 2006; Conroy 2013, and references therein). Magnesium, an α-element, is ejected into the interstellar mediumby Type-II supernovae resulting from massive stars on time-scales of $\sim$10 Myr, whereas most of the iron is released on time-scales of $\sim$1 Gyr, when SNIa explosions of intermediate-mass stars in binary systems occur. Although other α-elements are expected to follow magnesium, there are exceptions to the rule such as calcium, which nearly tracks Fe (e.g. Vazdekis et al. 1997; Worthey 1998; Saglia et al. 2002; Cenarro et al. 2003; Falcón-Barroso et al. 2003b, Thomas, Maraston & Bender 2003b; Yamada et al. 2006; Worthey, Ingermann & Serven 2011; Conroy & van Dokkum 2012b; Johansson, Thomas & Maraston 2012; La Barbera et al. 2013). These abundances and the abundance ratios of other elements can therefore be used to investigate the star formation time-scales of ETGs (e.g. Conroy, Graves & van Dokkum 2014).

Aiming at obtaining more quantitative determinations, models with varying abundance ratios were developed with the aid of theoretical stellar spectra (Tripicco & Bell 1995; Korn, Maraston & Thomas 2005). The responses obtained for the Lick indices to variations of the individual element abundances, i.e. the so-called response functions, were used to correct the model predictions based on the empirical stellar libraries (e.g. Vazdekis et al. 1997; Tantalo, Chiosi & Bressan 1998; Trager et al. 2000; Thomas et al. 2003a; Tantalo & Chiosi 2004; Schiavon 2007; Chung et al. 2013). These models allowed us to achieve a better understanding of what these line strengths are made of, as none of these rather strong atomic and molecular lines are contributed to by a single element. Although with the use of these indices it has been possible to partially lift the age/metallicity degeneracy affecting the colours, these indices are not completely free from this degeneracy (Worthey 1994; Arimoto 1996).

This degeneracy is due to the fact that an age increase causes an effect on the theoretical isochrone and on line-strength indices that can be mimicked – at constant age – by a metallicity increase. The effects of this degeneracy are stronger when low-resolution indices are used, as the metallicity lines appear blended. For such a reason, alternative indices – that were thought to work at higher spectral resolutions, such as those of e.g. Rose (1985, 1994) and Serven, Worthey & Briley (2005) – have been designed to alleviate the problem.

New means for improving the stellar population analysis have been achieved by predicting full SEDs at moderately high resolution, rather than just a number of indices. Such modelling has been possible with the development of extensive empirical stellar spectral libraries with flux-calibrated spectral response and good atmospheric parameters coverage. Among the most widely employed stellar libraries in the optical range are those of Jones (1999), ELODIE (Prugniel & Soubiran 2001), STELIB (Le Borgne et al. 2003), Indo-US (Valdes et al. 2004) and MILES (Sánchez-Blázquez et al. 2006a) and more recently XSL (Chen et al. 2014). Models that employ such libraries are, e.g. Vazdekis (1999), Schiavon et al. (2002), Bruzual & Charlot (2003), Le Borgne et al. (2004), Vazdekis et al. (2010), Maraston & Strömbäck (2011), Conroy &

[1] Some authors use the term 'solar-scaled' as opposed to scaled-solar, and we regard these terms as interchangeable.

van Dokkum (2012a). There are also empirical libraries in other spectral ranges such as, e.g. Cenarro et al. (2001a,b), Cushing, Raynier & Vacca (2005), Raynier, Cushing & Vacca (2009), that are also implemented in these models (Vazdekis et al. 2003; Conroy & van Dokkum 2012a). Alternatively, theoretical stellar libraries at high spectral resolutions have also been developed for this purpose (e.g. Barbuy et al. 2003; Murphy & Meiksin 2004; Zwitter, Castelli & Munari 2004; Coelho et al. 2005; Martins et al. 2005; Munari et al. 2005; Rodríguez-Merino et al. 2005; Frémaux et al. 2006; Martins & Coelho 2007; Leitherer et al. 2010; Palacios et al. 2010; Kirby 2011; de Laverny et al. 2012; Coelho 2014). Models that make use of these libraries are, e.g. Leitherer et al. (1999), Schiavon, Barbuy & Bruzual (2000), González-Delgado et al. (2005), Coelho et al. (2007), Buzzoni et al. (2009), Lee et al. (2009a), Percival et al. (2009), Maraston & Strömbäck (2011).

These models provide ways to alleviate the main degeneracies hampering stellar population studies. For example, with these SEDs it has been possible to define new indices with enhanced abilities to disentangle the age from the metallicity (e.g. Vazdekis & Arimoto 1999; Bruzual & Charlot 2003; Cervantes & Vazdekis 2009), or even the IMF (e.g. Schiavon et al. 2000; Cenarro et al. 2001a; Vazdekis et al. 2003, 2012; Conroy & van Dokkum 2012a; La Barbera et al. 2013; Spiniello et al. 2014). It is becoming common practice to use these model SEDs with newly developed algorithms that aim at constraining and recovering the SFH by means of full spectrum-fitting approach (e.g. Panter, Heavens & Jimenez 2003; Cid Fernandes et al. 2005; Ocvirk et al. 2006a,b; Chilingarian et al. 2007; Koleva et al. 2009; Tojeiro et al. 2011). This method represents an alternative to the more classical approach of fitting a selected number of line-strength indices (e.g. Trager et al. 1998). Furthermore, these model SEDs have been used in a variety of applications. For example, these SSP SEDs have been shown to improve the analysis of galaxy kinematics for both absorption and emission lines (e.g. Falcón-Barroso et al. 2003a; Sarzi et al. 2006). Models based on empirical libraries are free from the uncertainties in the underlying model atmospheric calculations and tend to provide good fits to both, absorption line-strengths and spectra (e.g. Sánchez-Blázquez et al. 2006a; Yamada et al. 2006; Maraston & Strömbäck 2011; Vazdekis et al. 2012; Conroy 2013) and also photometric data (e.g. Maraston et al. 2009; Peacock et al. 2011; Ricciardelli et al. 2012). However, unlike the models based on theoretical libraries, these models are generally restricted in their SSP parameters coverage, as most of the stars come from the solar neighbourhood, with a characteristic, and limited, elemental abundance ratio coverage (Milone, Sansom & Sánchez-Blázquez 2011; see also fig. 1 in Walcher et al. 2009 which illustrates the effect of the solar-neighbourhood pattern on models based on empirical libraries). The quality of the resulting model SEDs relies to a great extent on the atmospheric parameters coverage of the library.

As most of the stars of these empirical libraries belong to the solar neighbourhood, the resulting model SEDs have a characteristic abundance pattern: at low metallicity, the predicted spectra are enhanced in α-elements, whereas around the solar value the models are nearly scaled-solar (e.g. Edvardsson et al. 1993; McWilliam 1997). In addition, most of these models employ scaled-solar isochrones and therefore they are not self-consistent at low metallicities. These models, which can also be regarded as 'base models', present important limitations for studying massive ETGs (or any other system that deviates strongly from the chemical pattern of the solar neighbourhood), which reside in a high-metallicity regime and show enhanced [Mg/Fe] abundance. It has been shown that by using α-enhanced stellar evolution models (e.g. Salaris, Groenewegen & Weiss 2000) and the stellar theoretical spectra (e.g. Tripicco & Bell 1995; Korn et al. 2005; Coelho et al. 2007), line indices such as Mg*b* and ⟨Fe⟩ are affected. However, it is worth noting that the base models have been successfully applied to these galaxies. In fact, it is possible to obtain a good proxy for the [Mg/Fe] abundance, if appropriate indices are employed for the analysis (Vazdekis et al. 2001b, 2010; Sánchez-Blázquez et al. 2006c; Yamada et al. 2006; de la Rosa et al. 2007; Michielsen et al. 2008; La Barbera et al. 2013). This proxy leads to a linear relation with the abundance ratio estimated with the aid of models that specifically take into account such non-solar element mixtures (e.g. Tantalo et al. 1998; Thomas et al. 2003a; Lee & Worthey 2005; Graves & Schiavon 2008).

There are some examples of models predicting SSP spectra at moderately high resolution with varying abundance ratios. Spectral SSP models that include varying abundance ratios both at the isochrones and stellar spectra have been presented in Coelho et al. (2007), Lee et al. (2009a), Percival et al. (2009). Also Cervantes et al. (2007), Prugniel et al. (2007), Walcher et al. (2009), Conroy & van Dokkum (2012a) present models with varying abundances but considering only the effect of the stellar spectra. There are also examples where only α-enhanced isochrones are employed, ignoring the effects of the stellar spectra in the line strengths (e.g. Weiss, Peletier & Matteucci 1995; Vazdekis et al. 2003). Self-consistent models can only be achieved when both the spectral and the evolutionary effects are correctly taken into account, and thus require the use of both theoretical spectra (e.g. Coelho et al. 2005; Munari et al. 2005), and isochrones with varying [α/Fe] abundance (e.g. Salaris & Weiss 1998; Salasnich et al. 2000; VandenBerg et al. 2000; Pietrinferni et al. 2006; Coelho et al. 2007; Dotter et al. 2008; VandenBerg et al. 2014; Kim et al. in preparation). To our knowledge, the three self-consistent models for a fair range of ages and metallicities available in the literature are Coelho et al. (2007), Lee et al. (2009a) and Percival et al. (2009). However, both these models carry a caveat: the stellar spectral libraries employed are theoretical, and as such they carry wavelength-dependent systematic deviations when compared to observed spectra (Martins & Coelho 2007; Bertone et al. 2008; Coelho 2014). Inspired by the work of Cervantes et al. (2007) and Prugniel et al. (2007), and in order to bring together the predictive power of fully theoretical models and the accuracy of the base models, Walcher et al. (2009) proposed a method to use the predictions of fully theoretical SSP models only differentially.

Here, we further develop our models to predict SSP spectra with varying [α/Fe] ratios based on the MILES library (Sánchez-Blázquez et al. 2006a; Cenarro et al. 2007b). For this purpose, we apply a differential correction to our empirical SSP models which is obtained from the theoretical stellar spectral library of Coelho et al. (2005, 2007). We also employ the scaled-solar and α-enhanced isochrones of BaSTI (Pietrinferni et al. 2004, 2006). This work is the second of the series that we started with Vazdekis et al. (2010, hereafter Paper I), where we presented our base model predictions that were fully based on the MILES library. As the parameter coverage of MILES constitutes a significant improvement over previous empirical stellar libraries, these models are safely extended to intermediate-aged stellar populations and to lower and higher metallicities.

The layout of the paper aims to permit the reader to follow the model construction from the very first steps, through the characterization of the model outputs and finally to provide some illustrative applications. In Section 2, we describe the main model ingredients, which include the IMF, the isochrones and the empirical and theoretical libraries employed here. In Section 3, we describe our approach

for constructing these SSP SEDs. The quality and behaviour of these SSP spectra are assessed in Section 4. In Sections 5 and 6, we show the behaviour of the line-strength indices and broad-band colours as measured on the resulting SSP spectra, respectively. In Section 7, we compare our models to predictions from other authors. In Section 8, we apply these models to data of Galactic globular clusters (GGCs) and ETGs to illustrate the predictive power of these new models. We compare the colours, the full spectra and the line strengths of ETGs with our models. We also calibrate a proxy to estimate the [Mg/Fe] abundance ratio, relying solely on scaled-solar predictions. In Section 9, we present the new features that we have introduced in our web page to make it publicly available these predictions, including more complex models with arbitrary SFHs. Finally, in Section 10 we provide a summary.

2 MODEL INGREDIENTS

In this section, we describe the main ingredients in our new stellar population synthesis models, namely the IMF, the isochrones and the stellar spectral libraries. We summarize the chief aspects of these ingredients that are particularly relevant to this work. We also describe the details and the treatment that have been required for implementing these ingredients in the models, which include new isochrones that were specifically computed for this work.

2.1 IMF

Several IMFs are considered: the two power-law IMFs described in Vazdekis et al. (1996), i.e unimodal and bimodal, both characterized by the logarithmic slope, Γ and Γ_b,[2] respectively, as a free parameter, and the multipart power-law IMFs of Kroupa (2001), i.e. universal and revised. The Salpeter (1955) IMF is obtained by adopting the unimodal case with slope $\Gamma = 1.3$.[3] Although not identical, the Kroupa Universal IMF is very similar to a bimodal IMF with slope $\Gamma_b = 1.3$. An extensive description of these definitions is given in Vazdekis et al. (2003, Appendix A). We set the lower and upper mass cutoff of the IMF to 0.1 and 100 $M_\odot$, respectively. It is worth noting that the very low-mass (VLM) ($<0.6\,M_\odot$) tapered 'bimodal' IMF has been found to be consistent with the line strengths and M/L of massive ETGs (e.g. Ferreras et al. 2013; La Barbera et al. 2013; Spiniello et al. 2014). On the contrary, the single power-law 'unimodal' IMF leads to extremely high M/L values that are not supported by independent gravitational lensing and dynamical estimates (e.g. Treu et al. 2013; Spiniello et al. 2012).

2.2 Isochrones

We employ two sets of theoretical isochrones. The scaled-solar isochrones of Girardi et al. (2000, hereafter Padova00) and Pietrinferni et al. (2004) and the α-enhanced models of Pietrinferni et al. (2006). The latter two will be regarded hereafter as BaSTI.

The Padova isochrones cover a wide range of ages, from 0.063 to 17.8 Gyr, and six metallicity bins ($Z = 0.0004$, 0.001, 0.004, 0.008, 0.019 and 0.03), where 0.019 represents the solar value. The isochrones also include the later stages of stellar evolution, using a simple synthetic prescription for incorporating the thermally pulsing asymptotic giant branch (TP-AGB) regime to the point of complete envelope ejection. The range of initial stellar masses extends from 0.15 to 7 $M_\odot$. The input physics of these models was updated with respect to Bertelli et al. (1994) with an improved version of the equation of state, the opacities of Alexander & Ferguson (1994) and a milder convective overshoot scheme. A helium fraction was adopted according to the relation: $Y \approx 0.23 + 2.25Z$.

We also use here the BaSTI theoretical isochrones.[4] The original sets of models have been supplemented by additional computations specifically performed for this project (see below for more details). A description of the complete BaSTI data base as well as of the adopted physical inputs and numerical assumptions can be found in Pietrinferni et al. (2004, 2006, 2009, 2013) and Cordier et al. (2007). We refer the interested reader to these references. Here, it is sufficient to note that the BaSTI archive is based on an updated physical framework and that it has been extensively tested with many observational constraints based on both resolved (mainly eclipsing binaries and cluster colour–magnitude diagrams) and unresolved stellar populations (see Pietrinferni et al. 2004 and Percival et al. 2009). In this work, we have adopted the non-canonical BaSTI models with the mass-loss efficiency set to $\eta = 0.4$[5] for both the scaled-solar and α-enhanced heavy elements mixture. The initial He mass fraction ranges from 0.245, for the more metal-poor composition, up to 0.303 for the more metal-rich composition, with $\Delta Y/\Delta Z \approx 1.4$. All the metallicity grid points available in the archive have been used. However, in order to better sample the whole metallicity range from very metal-poor to the most metal-rich stellar populations, we have added an additional grid point corresponding to $Z = 0.024$, $Y = 0.279$ (i.e. $[M/H] = +0.15$) for both scaled-solar and α-enhanced mixture. This metallicity is particularly relevant for studying massive ETGs (e.g. La Barbera et al. 2013). Therefore, the BaSTI metallicity grid adopted in present analysis was based on 12 grid points: $Z = 0.0001$, 0.0003, 0.0006, 0.001, 0.002, 0.004, 0.008, 0.0100, 0.0198, 0.0240, 0.0300 and 0.0400. For each metallicity, the isochrone age range covers the interval from 0.03 to 14 Gyr, with a fine age grid.

We note that the atomic diffusion of both helium and metals was properly accounted for when computing the solar model in order to be able to match accurately the helioseismological constraints. The best match to the depth of the convective envelope (0.716 $R_\odot$) of the present solar envelope He abundance ($Y = 0.244$), and of the actual (Z/X) ratio [($Z/X = 0.0244$], lead to an initial He abundance and metallicity ($Y_\odot = 0.2734$, $Z_\odot = 0.0198$), which was adopted for the solar metallicity model set.

We have used here the 'AGB-extended' version of the BaSTI isochrones that account for the AGB stage as provided by Cordier et al. (2007). This phase includes the entire TP-AGB regime through a synthetic-AGB treatment following the technique of Iben & Truran (1978). In this approach, the mass-loss processes are accounted for by using the formulae of Vassiliadis & Wood (1993). The evolution with time of the CO core mass and surface luminosity is accounted for by adopting the analytical relationships

[2] Note that we have changed our notation for the IMF slope from that we used in our previous papers, i.e. μ (e.g. Vazdekis et al. 1996, 2003; Paper I; Vazdekis et al. 2012). We now adopt Γ and Γ_b for the slopes of the unimodal and bimodal IMF shapes, respectively, to be consistent with recent works on the variation of the IMF. Note also that in the new notation we distinguish the slopes of these two IMF shapes as they apply to different functional forms.

[3] In reality, it would be more accurate to use $\Gamma = 1.35$ to match the Salpeter slope.

[4] The BaSTI data base is publicly available at http://basti.oa-teramo.inaf.it/index.html.

[5] We note that η represents the free parameter present in the Reimers mass-loss law (Reimers 1977) adopted in the BaSTI stellar model computations.

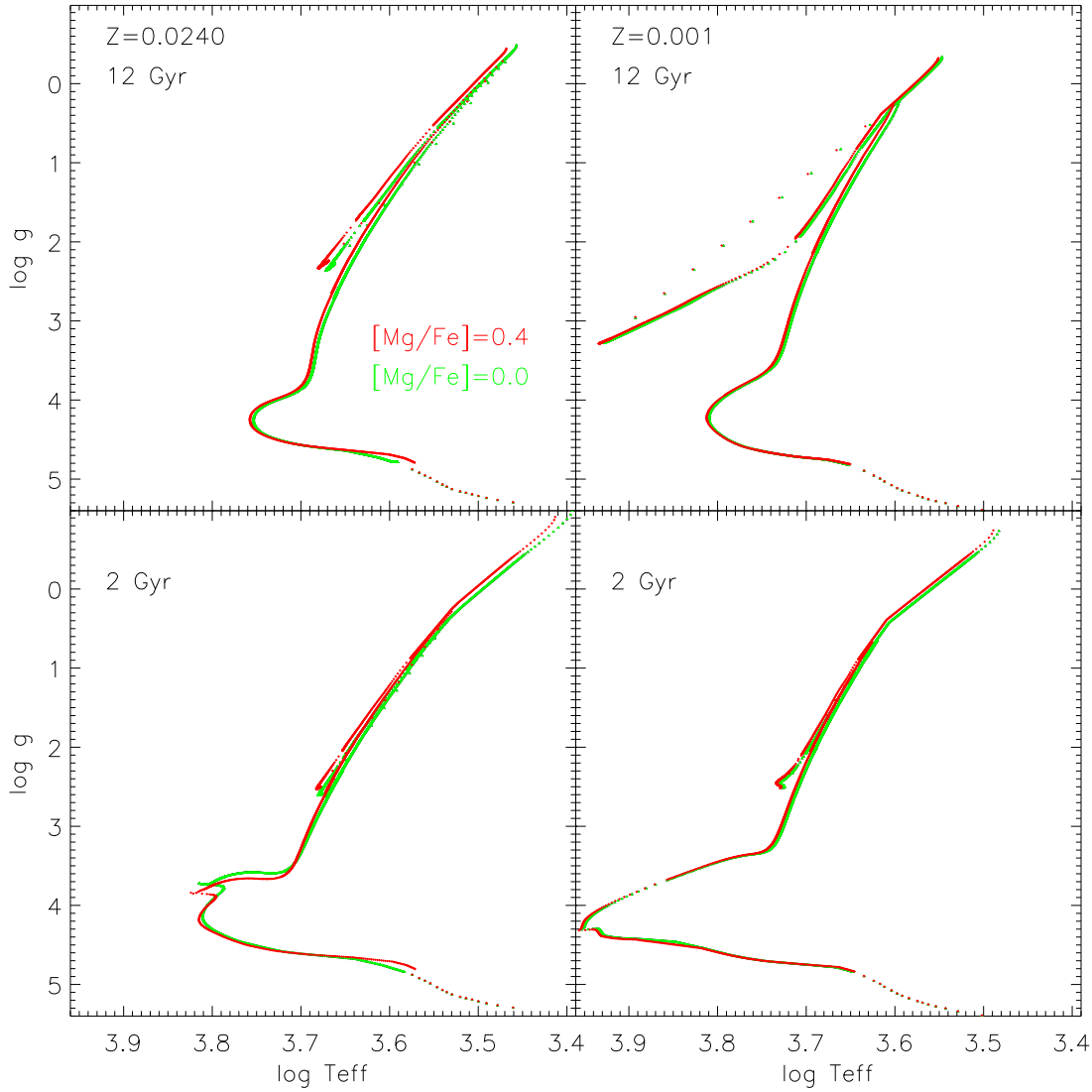

Figure 1. Comparison of α-enhanced ([α/Fe] = +0.4)and scaled-solar BaSTI isochrones. Two representative metallicities $Z = 0.024$ (left) and $Z = 0.001$ (right) and two ages 12 Gyr (top) and 2 Gyr (bottom) are shown.

provided by Wagenhuber & Groenewegen (1998), while the trend with time of the effective temperature is provided according to the relationship of Wagenhuber (1996). We wish to emphasize that our synthetic-AGB treatment does account[6] for the occurrence – and, hence for the related evolutionary effects – of the third dredge-up and hot-bottom burning when appropriate. We notice that this simplified model for the TP-AGB phase has been shown to be adequate for matching several integrated properties in the near-IR as discussed in Cordier et al. (2007). In addition, in order to assess the reliability of the theoretical framework adopted in this work, we would like to call the attention of the reader to the recent analysis performed by Salaris et al. (2014). They presented stellar population synthesis models based on fully evolutionary AGB computations (Weiss & Ferguson 2009, i.e. without the need of adopting analytical relations as in the synthetic-AGB treatment) and compared their model predictions with integrated colours from other models. They found significant discrepancies with results from Marigo et al. (2008)

[6] We would like to emphasize that the claim provided by Marigo et al. (2008) that the AGB-extended version of the BaSTI isochrones does not explicitly account for AGB nucleosynthesis, i.e. the effects of the third dredge-up and hot-bottom burning, in the underlying AGB models, is not correct. The analytical relationships for the trend of the surface luminosity and effective temperature as a function of the He core mass provided by Wagenhuber & Groenewegen (1998) and Wagenhuber (1996) are adopted in the BaSTI synthetic-AGB treatment, do account for the occurrence of these physical processes during the AGB stage. In order to provide a correct description of the situation, we wish to note that the computations by Wagenhuber (1996) were performed without accounting for low-temperature radiative opacities with various C/O ratios – because these opacity tables were not available at that time. Notwithstanding, the effect of the change in the envelope C/O ratio induced by the third dredge-up was mimicked by adopting a radiative opacity at a constant heavy elements distribution, but allowing the global metallicity to change. Cristallo et al. (2007) and Weiss & Ferguson (2009) have shown that, although the use of opacity tables that properly include the enhancements of C is more appropriate, the predictions of the behaviour with time of $T_{\rm eff}$ as provided by fully consistent AGB models are not significantly different from those predicted by models that account for the opacity effects of the third dredge-up by adopting a variable global metallicity but constant C/O ratio.

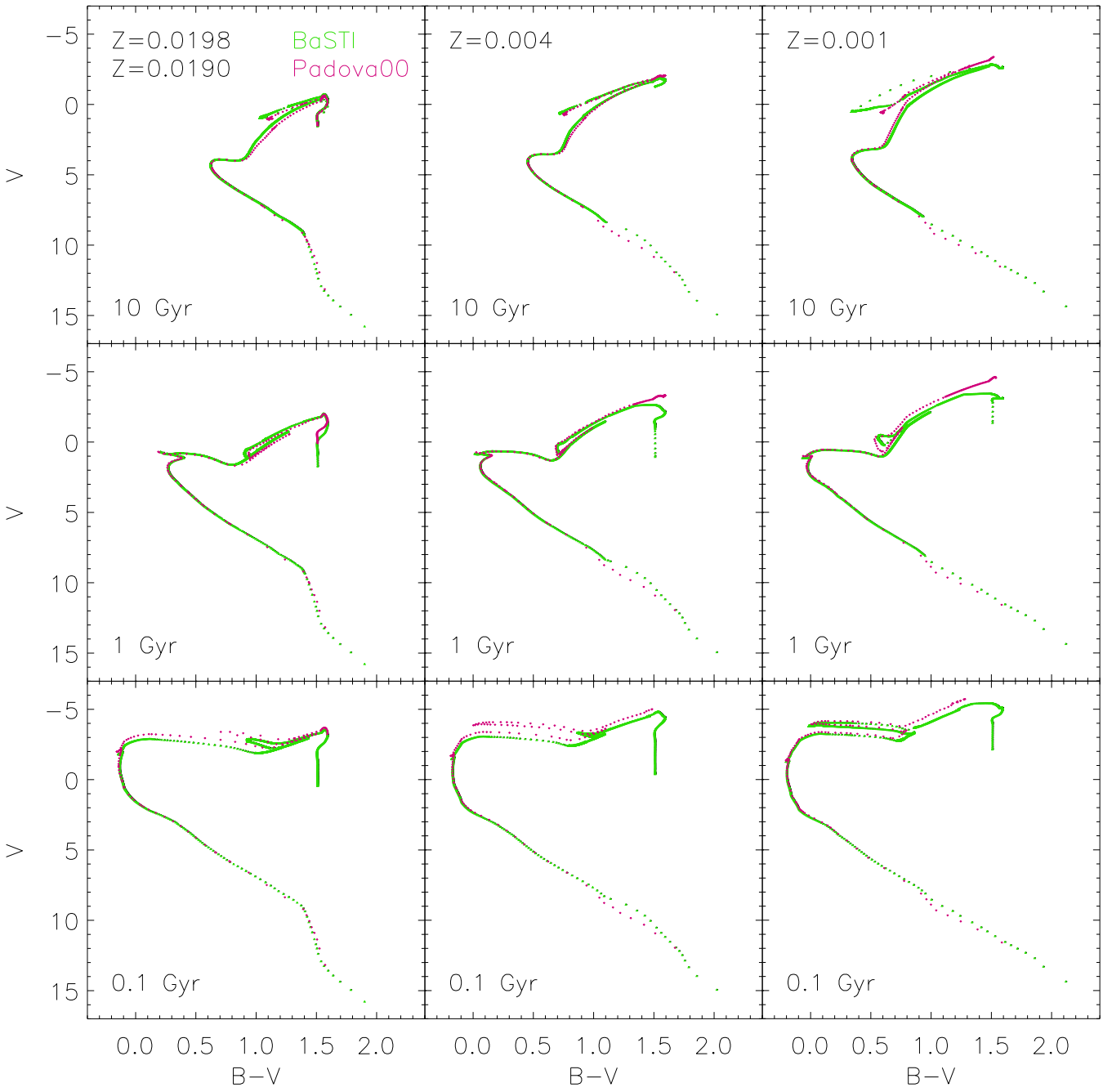

Figure 2. Comparison of the Padova00 and BaSTI isochrones for three representative metallicities ($Z = 0.001$, $Z = 0.004$ and solar), as quoted within the upper panels, and three different ages, 10, 1 and 0.1 Gyr from top to bottom panels. Note that the reference solar metallicity value is slightly different for these two models. There are differences in the RGB, HB and AGB phases as well as in the VLM dwarf stars.

and Maraston (2005),[7] whereas an excellent agreement was found with the BaSTI AGB-extended models.

The lower mass limit in the standard BaSTI isochrones is 0.5 $M_{\odot}$. However, for the aim of this study, we have extended the isochrones to the VLM regime by including additional stellar models down to a lower mass limit of 0.1 $M_{\odot}$. The adopted VLM models are the same presented in Cassisi et al. (2000), which are based on an updated physical framework for the evolutionary computations of VLM stellar models. We have made a significant effort to obtain a smooth transition when passing from the low-mass regime (BaSTI models) to the VLM ones. This has been obtained by computing some additional stellar models in the transition mass regime (around $\approx$0.5–0.6 $M_{\odot}$) by using the same physical inputs adopted for the BaSTI model computations but the same outer boundary conditions used in the VLM stellar model computations (see Cassisi et al. 2000 for more details on this issue). Our temperatures for these stars are cooler than those of Padova00, and warmer than those of Pols et al. (1995), which were implemented in Vazdekis et al. (1996),

[7] A comparison among these population synthesis models and observations has been already performed by Noel et al. (2013), and it was found that these models disagree – being in general too red – with the integrated colours of superclusters for ages between $\sim 10^8$ and $\sim 10^9$ years.

and those of Dotter et al. (2008, see also An et al. 2009). As their temperatures are higher the Padova00, VLM stars are brighter than the ones we employ here for the BASTI models (see fig. 5 in Vazdekis et al. 2012).

In Fig. 1, we plot a set of BaSTI isochrones for two selected metallicities and ages. We see that the higher the metallicity, the greater the difference between the scaled-solar and the α-enhanced models, with the scaled-solar isochrones being slightly cooler than the α-enhanced isochrones (see Pietrinferni et al. 2006). These differences arise since we are comparing the two sets of isochrones at constant global metallicity; when comparing the two sets at constant iron content, the α-enhanced isochrones would appear cooler that the corresponding scaled-solar isochrones as a consequence of their larger global metallicity and, hence, higher opacity at low temperatures. (see e.g. figs 1 and 2 in Coelho et al. 2007 and fig. 1 in Lee, Worthey & Dotter 2009b). A more elaborated discussion on these effects, including those when varying the abundance ratio of individual α-elements can be found in Lee, Worthey & Blakeslee (2010). While there are clearly differences between the two sets of isochrones, it is worth noting that these differences are always small.

We use the theoretical parameters of these two sets of isochrones ($T_{\rm eff}$, $\log g$, $[M/{\rm H}]$) to obtain stellar fluxes on the basis of empirical relations between colours and stellar parameters (temperature, gravity and metallicity), instead of using theoretical stellar fluxes. We mainly use the metallicity-dependent empirical relations of Alonso, Arribas & Martínez-Roger (1996, 1999), respectively, for dwarfs and giants. Each of these libraries are composed of ∼500 stars and the temperature scales are based on the IR-Flux method, i.e. only marginally dependent on model atmospheres. We use the empirical compilation of Lejeune, Cuisinier & Buser (1997, 1998, and references therein) for the coolest dwarfs ($T_{\rm eff} \lesssim 4000$ K) and giants ($T_{\rm eff} \lesssim 3500$ K) for solar metallicity, and also for stars with temperatures above ∼8000 K. We use a semi-empirical approach for these low-temperature stars for other metallicities. For this purpose, we combine these relations and the model atmosphere predictions of Bessell et al. (1989, 1991) and the library of Fluks et al. (1994). We also employ the metal-dependent bolometric corrections given by Alonso, Arribas & Martínez-Roger (1995) and Alonso et al. (1999) for dwarfs and giants, respectively. Finally, we adopt $\mathrm{BC}_{\odot} = -0.12$. By assuming $\mathrm{V}_{\odot} = 26.75$ (Hayes 1985), the solar absolute magnitude is $\mathrm{M}_{\mathrm{V}_{\odot}} = 4.82$, therefore, for the adopted normalization, $\mathrm{M}_{\mathrm{bol}_{\odot}}$ is given by $\mathrm{M}_{\mathrm{V}_{\odot}} + \mathrm{BC}_{\mathrm{V}_{\odot}} = 4.70$.

In this work, the integrated colours and spectral indices based on the BaSTI stellar models are compared to those obtained on the basis of the Padova models. Therefore, we consider it worthwhile to briefly discuss some of the principal differences between the two theoretical evolutionary frameworks. Fig. 2 shows a comparison for three representative metallicities ($Z = 0.001$, Z=0.004 and solar) and three ages (10, 1 and 0.1 Gyr). A detailed comparison between the scaled-solar BaSTI models and the Padova00 isochrones has been performed in Pietrinferni et al. (2004), and we refer the reader to section 6 of this paper for details. Here, it is sufficient to note that there is a systematic offset between the BaSTI and Padova models in the RGB $T_{\rm eff}$ scale, with BaSTI being hotter models at solar metallicity, whereas at lower metallicities the trend is reversed and BaSTI is cooler than Padova00. There are also significant differences in the brightness of the isochrones (at a given age) for ages lower than about 2 Gyr. These differences can be fully understood when accounting for the differences in the adopted physical inputs and in the different treatment of core convective overshooting during the core H-burning stage (see the discussion in Pietrinferni et al. 2004). We also see important differences in the AGB stellar evolutionary phase, as illustrated by the middle panels of Fig. 2. These late evolutionary stages are brighter in the Padova models at 1 Gyr, whereas the BaSTI AGB extends towards cooler temperatures, with such trends depending on the metallicity. This difference is quite well known as these stars reach the temperature regimes where the $B - V$ colour saturates (see e.g. Worthey & Lee 2011). Note that this difference is further emphasized at younger ages. Similarly, the two sets of models show important differences during the core He-burning stage: for old ages (i.e. larger than ∼3–4 Gyr) this is due to both the differences in the adopted physical framework and (mainly) in the adopted efficiency of mass-loss along the RGB stage; while for younger ages the origin of the differences in the 'blue loops' – characteristic of the core He-burning stage of intermediate-mass stars – could be related to many different contributions (physical inputs, treatment of convection, the details of the heavy elements mixtures, etc.) as discussed in detail by Cassisi (2004).

Another interesting feature that is relevant to IMF studies is the difference in effective temperature between these two sets of models for the VLM stars, with the Padova models being hotter in all the panels of Fig. 2. This is related to the different physical inputs to the models – mainly in the equation of state and outer boundary conditions – adopted for computing the two sets of VLM stellar models (see Cassisi et al. 2000 and references therein for more details on this topic).

2.3 Stellar spectral libraries

2.3.1 MILES

The new models presented in this work, for both the scaled-solar and α-enhanced mixture, are computed – in the optical range – on the basis of the MILES stellar spectral library[8] (Sánchez-Blázquez et al. 2006a). This library was prepared carefully to be implemented in our models (Paper I). For a detailed description, we refer the reader to these two papers and also to Cenarro et al. (2007b), for the determination of the stellar parameters. Here, we briefly summarize the most relevant aspects of the library.

The MILES library is composed of 985 stars observed at the INT 2.5m telescope on El Roque de Los Muchachos observatory at La Palma, Spain. Two gratings were employed to cover the full optical range at 2.51 Å (FWHM) resolution, which is constant with wavelength (see Falcón-Barroso et al. 2011 for a full description). The spectra have very high signal-to-noise (S/N) which is usually well above 100, with the exception for the stars that belong to globular clusters (GCs) such as M 71, which were included to improve the parameter space coverage. The spectra were carefully flux-calibrated; each individual star was also observed through a wide slit in order to avoid selective flux losses due to differential refraction effects, in addition to the higher resolution setups used to achieve the blue and red parts of the stellar spectra. Careful attention was also paid to the cleaning of telluric absorptions that were present in the redder part of the spectra.

Our models make use of a subsample of 925 stars from the original library since we removed those stars whose spectra were not properly representative of a given set of atmospheric parameters. These included spectroscopic binaries (identified with SIMBAD), or stars with unexpectedly high signal of variability (according to

[8] The MILES library is publicly available at http://miles.iac.es.

the CDS electronically readable version of the Kholopov et al. 1998 catalogue) for which there were alternative stars in the MILES data base with similar parameters. Other reasons for removing stars were the presence of emission lines, very low S/N in the blue, problems in the continuum and the lack of atmospheric parameters determinations. For this process, each stellar spectrum was compared to a synthetic spectrum of similar atmospheric parameters computed with the interpolation algorithm described in Paper I after exclusion of the targeted star. Finally, 75 stellar spectra with some, milder, problems were retained in the final sample as they were found to be useful for improving the coverage of certain regions of the parameter space. For these stars, we decreased their relative weight in comparison to the other stars.

The parameters for MILES stars were obtained from an extensive compilation from the literature, homogenized by taking as a reference the stars in common with the high-resolution stars of Soubiran, Katz & Cayrel (1998, see Cenarro et al. 2007b). One of the most relevant features of this library is the significant improvement of the parameter coverage in comparison to other widely employed stellar spectral libraries (see fig. 2 in Paper I). MILES spans a fairly wide range in metallicity, including stars with $[M/H] < -2$ as well as supersolar, for the temperature range that is relevant for intermediate and old stellar populations, both for dwarf and giant stars. Note that, unlike in other stellar libraries (see Paper I), MILES includes a number of metal-poor dwarf stars with $T_{\rm eff} > 6000$ K, which are relevant for predicting stellar populations with ages smaller than $\sim$10 Gyr at low metallicities. This library also includes a number of VLM dwarfs, which are relevant when varying the IMF slope. Although not optimized for very young stellar populations (see Paper I), the library has Main Sequence stars as hot as $\sim$30 000 K, mostly around solar metallicity. It also includes giants with temperatures above 6000 K, such as metal-poor horizontal branch (HB) stars, post-AGB stars and variable stars of the type δ Scuti, RR Lyrae or Cepheids along the instability strip.

An important improvement here is the consideration of the [Mg/Fe] estimates for most of the MILES stars, which have been recently determined by Milone et al. (2011). These abundance ratios were obtained through a compilation of values from the literature using abundances from high-resolution spectroscopic studies and from a robust spectroscopic analysis using the MILES spectra. These [Mg/Fe] values were carefully calibrated to a single uniform scale with a typical uncertainty on the estimates of $\sim$0.1 dex. As expected, the MILES library follows the abundance pattern of the Galaxy (see fig. 10 in Milone et al. 2011), although there is some dispersion at any given metallicity. There were 75 stars in the selected MILES subsample for which Milone et al. (2011) could not determine their [Mg/Fe] values (the majority of them have effective temperatures either above $\sim$8000 K or below $\sim$3500 K, and also stars belonging to stellar clusters). To retain these stars for our model computations, we assigned the mean abundance ratio expected for the [Fe/H] value of the star according to the pattern found by Milone et al. (2011) for the field stars. For the cluster stars, we adopted the mean value determined by Milone et al. (2011) for the other stars of the same cluster.

Fig. 3 shows the stellar parameter coverage of the subsample composed of 925 stars selected from the MILES data base. Stars with [Mg/Fe] abundance ratio smaller (larger) than +0.2 are plotted in green (red). Note that we only plot parameters for stars with temperatures below 8000 K, as the abundance estimates for higher temperatures are more uncertain (see for details Milone et al. 2011) and the net effect of the abundance on the spectra is small (see fig. 9 of Sansom et al. 2013). As expected, the stars enhanced in

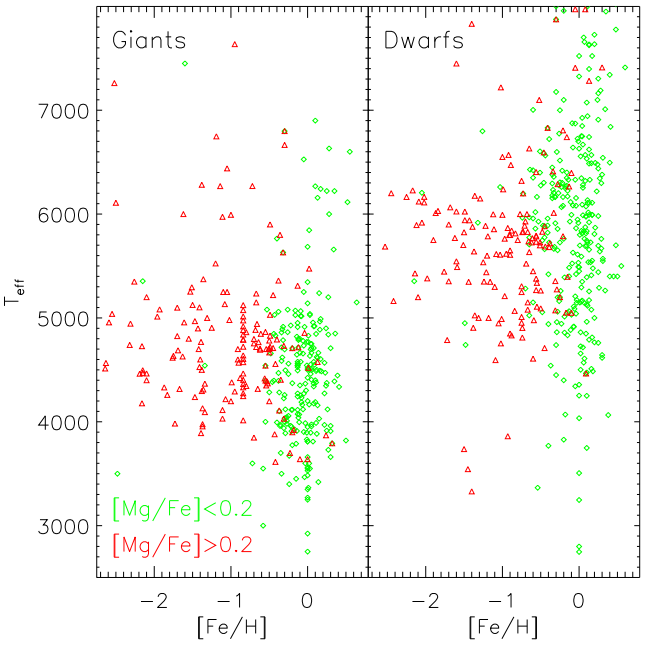

Figure 3. Stellar parameters coverage of the MILES library. Red triangles and green diamonds represent stars with [Mg/Fe] values larger and smaller than 0.2, respectively. For this plot, we split the data base in giants (left-hand panel) and dwarfs (right-hand panel) at $\log g = 3.0$.

[Mg/Fe] also have [Fe/H] $\lesssim -0.5$, whereas the higher metallicity regime is populated with scaled-solar stars. We also see that MILES stars show a good coverage of temperature within the metallicity regime $-0.5 \lesssim$ [Fe/H] $\lesssim +0.2$. Despite a significant decrease in the number of stars for the more metal-poor and metal-rich regimes, there are sufficient stars to compute models with [Fe/H] $\simeq -2.3$ and [Fe/H] $\simeq +0.4$, although within a limited age range. A quantitative analysis of the quality of the models based on the atmospheric parameters coverage of the library stars is shown in Section 4.1.

2.3.2 *Theoretical stellar spectral library*

Theoretical spectra are employed to determine a differential correction to be applied to the reference models computed on the basis of MILES (see Section 3). In order to compute these 'corrected' SSPs, we adopt the theoretical stellar library of Coelho et al. (2005), with the extension to very cool giants and the spectrophotometric calibration presented in Coelho et al. (2007). These stars were computed with PFANT spectral synthesis code, and are based on refined atomic and molecular line lists (e.g. Cayrel et al. 1991; Barbuy et al. 2003). Model atmospheres from Castelli & Kurucz (2003) are adopted for effective temperatures $T_{\rm eff} \geq 3500$ K, and from Plez (1992) for $T_{\rm eff} < 3500$ K. We refer the reader to Coelho et al. (2005, 2007) for more details.

The Coelho et al. (2005) theoretical library covers effective temperatures, $T_{\rm eff}$, between 3500 and 7000 K, surface gravities, $\log g$, between +0.0 and +5.0, iron metallicities, [Fe/H], between −2.5 and +0.5 and α-element over iron abundances, $[\alpha/{\rm Fe}] = +0.0$ and $[\alpha/{\rm Fe}] = +0.4$. The extension to cool giants from Coelho et al. (2007) covers $T_{\rm eff}$ down to 2800 K, $\log g$ between −0.5 and 1.5, [Fe/H] = −0.5, 0.0 and +0.2, and $[\alpha/{\rm Fe}] = +0.0$ and $[\alpha/{\rm Fe}] = +0.4$. The scaled-solar spectra ($[\alpha/{\rm Fe}] = 0.0$) have the solar abundances from Grevesse & Sauval (1998). The α-enhanced spectra ($[\alpha/{\rm Fe}] = +0.4$) adopt a uniform enhancement

[X/Fe] = +0.4 for the elements O, Ne, Mg, Si, S, Ca and Ti, and the other elements follow the solar abundances.

The accuracy of this library has been assessed in Martins & Coelho (2007), who showed that this library had the highest success in reproducing spectral features of observed stars among the theoretical libraries analysed in that work. The spectra have higher spectral resolution and wavelength coverage than MILES, therefore they were convolved with a Gaussian kernel and were resampled to match MILES spectral resolution, dispersion and wavelength coverage.

3 SSP SPECTRAL SYNTHESIS MODELLING

To compute the spectra of single-burst stellar populations, i.e. SSPs, we follow the method described in detail in Paper I. This approach consists of integrating the spectra of the stars along the isochrone taking into account their number per mass bin according to the adopted IMF. In this study, we distinguish and provide three types of models for a given total metallicity, [M/H].[9] The first type of model SSPs are what we call *base models*, which combine scaled-solar isochrones of a given total metallicity with the MILES stars of similar [Fe/H] (rather than [M/H]), irrespective of their [Mg/Fe] abundance ratio. As MILES follows the abundance pattern of the Galaxy, these models are effectively scaled-solar at solar metallicity. However, for lower metallicities these models are not self-consistent in the sense that observed stars are enhanced in [Mg/Fe], whereas the isochrones are scaled-solar. Therefore, the SSP SEDs of Paper I, which combine MILES with the Padova00 isochrones, should be regarded as base models. The second type of models presented here are termed *scaled-solar* as both the stellar spectra and the isochrones are scaled-solar throughout the whole metallicity range. Finally, the third type of models computed here are the *α-enhanced* models, which combine α-enhanced stellar spectra with α-enhanced isochrones. For the scaled-solar and α-enhanced models, which are computed on the basis of the total metallicity, [M/H], we take into account both the recent [Mg/Fe] determinations of Milone et al. (2011) and the [Fe/H] estimates of the individual library stars.

3.1 Base models

The term 'base model' refers to the commonly used approach that is employed to compute SSP models, as we describe in this section. It should not be confused with the terms BaSTI- or Padova00-based models, which refer to the use of a particular set of isochrones used to generate the SSP models. For the base models, we always employ scaled-solar isochrones. We compute here two sets of models that, to be precise, should be termed BaSTI-based base models and Padova00-based base models. For brevity henceforth, we will refer to these models as BasTI base models and Padova00 base models.

The base SSP model spectra are computed according to the following expression

$$S_\lambda(t, [M/\mathrm{H}], \Phi, I_{0.0}) = \int_{m_l}^{m_t} S_{\lambda_V}(m, t, [\mathrm{Fe/H}]) \times F_V(m, t, [\mathrm{Fe/H}]) N_\Phi(m, t)\, \mathrm{d}m, \quad (1)$$

where $S_{\lambda_V}(m, t, [\mathrm{Fe/H}])$ is the empirical stellar spectrum, irrespective of its [Mg/Fe] abundance, normalized in the V band, corresponding to a star of mass m and metallicity [Fe/H], which is alive at the age t of the stellar population. Its spectrum is also characterized by the $T_{\rm eff}$ and $\log g$ parameters as determined by the adopted scaled-solar isochrones, $I_{0.0}$. $F_V(m, t, [\mathrm{Fe/H}])$ is the flux of the star in the V band. For these base models, we assume that [M/H] = [Fe/H]. This is why we write in the left term of this equation [M/H], whereas in the right one we use the [Fe/H] abundance measurement. Therefore, the base models in the low-metallicity regime are not self-consistent since the MILES stars are enhanced in [Mg/Fe], and therefore the true [M/H] value is in reality larger than the adopted [Fe/H] value (see Section 3.2). $N_\Phi(m, t)$ is the number of such stars in the mass bin $(m, m + \mathrm{d}m)$, which depends on the adopted IMF, $\Phi(m)$. The lowest and highest mass stars that are alive at this age are m_l and m_t. Note that m_t is determined by the isochrone.

To normalize the stellar spectra in the V band, we convolve with the filter response of Buser & Kurucz (1978). These spectra are then scaled according to the predicted flux in this band, following the empirical photometric libraries described in Section 2.2. In order to obtain the absolute flux in the V band, we follow the method described in Falcón-Barroso et al. (2011), which is based on the calibration of Fukugita, Shimasaku & Ichikawa (1995):

$$F_V = 10^{-0.4(V + \mathrm{Zp}_V - V_{\alpha\mathrm{Lyr}})}, \quad (2)$$

where Zp_V and $V_{\alpha\mathrm{Lyr}}$ are the adopted zero-point and V magnitude for the reference Vega spectrum, respectively. To compute the zero-point, we used the Hayes (1985) spectrum of Vega with a flux of 3.44×10^{-9} erg cm^{-2} s^{-1} Å^{-1} at 5556 Å. The V magnitude of Vega is set to 0.03 mag, which is consistent with the value adopted by Alonso et al. (1995), i.e. in agreement with our prescriptions to transform the theoretical parameters of the isochrones to the observational plane. This scheme allowed us to achieve absolute magnitudes derived directly from the synthesized SSP spectra, which were fully consistent with those computed from the photometric libraries for the same SSPs. These uncertainties are well below the observational uncertainties ($\lesssim 0.01$ mag) for all ages, metallicities and IMFs. We refer the reader to Falcón-Barroso et al. (2011) for more details on the achieved accuracy.

3.2 Truly scaled-solar and α-enhanced models

To compute both the truly scaled-solar and the α-enhanced SSP spectra, with [α/Fe] = 0.0 and +0.4, respectively, we feed the code with stars according to their estimated [Fe/H] and [Mg/Fe] values. We therefore re-write equation (1) as follows:

$$S_\lambda(t, [M/\mathrm{H}], [\alpha/\mathrm{Fe}], \Phi, I_\alpha) = \int_{m_l}^{m_t} S_\lambda(m, t, [\mathrm{Fe/H}], [\mathrm{Mg/Fe}]) \times F_V(m, t, [\mathrm{Fe/H}], [\mathrm{Mg/Fe}]) \times N_\Phi(m, t)\, \mathrm{d}m. \quad (3)$$

In this case, the isochrone, I_α, is characterized by the [α/Fe] abundance ratio, which in this study can take the value of 0.0 and +0.4. This notation can be generalized to any abundance ratio, including any particular choice of element ratios, by substituting α and [Mg/Fe] by the desired elemental abundance(s) ratio(s) in this equation. Conversely, this notation is not appropriate for the base models, which do not take into account any consideration for the abundance ratios.

Note that the only abundance ratio provided in Milone et al. (2011) is that of [Mg/Fe], but not those corresponding to the other α-elements. Hereafter, we write [Mg/Fe] when referring to the abundance ratio of the stars, which is a measured quantity, whilst

[9] We use [M/H], rather than [Z/H] (as used in Paper I), because Z denotes a mass fraction, and therefore [M/H] is less confusing.

for the models we use [α/Fe]. This is because we use the [Mg/Fe] as a proxy for the [α/Fe] abundance ratio of the star (see below and see also Section 3.3) and because we employ theoretical isochrones with varying abundance for all the α-elements, i.e. [α/Fe].

We take into account the following relation between the iron abundance and the total metallicity:

$$[\mathrm{Fe/H}] = [M/\mathrm{H}] - A \times [\mathrm{Mg/Fe}]. \quad (4)$$

The conversion between [Fe/H] and [Mg/Fe] is dependent on the exact solar chemical mixture adopted. For this study, we adopt $A = 0.75$, in order to be consistent with the theoretical stellar spectra of Section 2.3.2 which follow the solar mixture of Grevesse & Sauval (1998).

For the high-metallicity regime, i.e. with $[M/\mathrm{H}] \geq 0$, where most of the MILES stars have [Mg/Fe] ~ 0.0, we use equation (3) to combine MILES with scaled-solar isochrones to compute scaled-solar SSP spectra of total metallicity $[M/\mathrm{H}] = [\mathrm{Fe/H}]$. Therefore, the resulting model, $S_\lambda(t, [M/\mathrm{H}], 0.0, \Phi, I_{0.0})$, does not differ significantly from the corresponding base model, $S_\lambda(t, [M/\mathrm{H}], \Phi), I_{0.0})$, around solar metallicity. Note that in this case only MILES library star spectra are employed to compute these models.

To synthesize an α-enhanced SSP spectrum with [Mg/Fe] $= +0.4$ and total metallicity, [M/H], we first compute a reference SSP spectrum, $S_{\lambda_{\mathrm{MILES}}}(t, [M/\mathrm{H}], 0.0, \Phi, I_{0.4})$, which combines an α-enhanced isochrone, $I_{0.4}$, with MILES scaled-solar stars. We use the BaSTI data base for this purpose. Note that this reference model is not self-consistent as the abundance ratios of the isochrones and the stellar spectra do differ. In addition, using the same α-enhanced isochrone we employ the theoretical stellar spectral library to compute two fully theoretical SSP spectra: one scaled-solar and the other α-enhanced, $S_{\lambda_{\mathrm{theo}}}(t, [M/\mathrm{H}], 0.0, \Phi, I_{0.4})$ and $S_{\lambda_{\mathrm{theo}}}(t, [M/\mathrm{H}], 0.4, \Phi, I_{0.4})$, respectively. With these models, we obtain a differential correction as follows:

$$\gamma_\lambda(t, [M/\mathrm{H}], \phi) = \frac{S_{\lambda_{\mathrm{theo}}}(t, [M/\mathrm{H}], 0.4, \Phi, I_{0.4})}{S_{\lambda_{\mathrm{theo}}}(t, [M/\mathrm{H}], 0.0, \Phi, I_{0.4})}. \quad (5)$$

This correction is then applied to the reference model, $S_{\lambda_{\mathrm{MILES}}}(t, [M/\mathrm{H}], 0.0, \Phi, I_{0.4})$, thereby giving a semi-empirical, MILES-based, self-consistent,[10] α-enhanced SSP spectrum

$$S_\lambda(t, [M/\mathrm{H}], 0.4, \Phi, I_{0.4}) = S_{\lambda_{\mathrm{MILES}}}(t, [M/\mathrm{H}], 0.0, \Phi, I_{0.4}) \times \gamma_\lambda(t, [M/\mathrm{H}], \Phi). \quad (6)$$

The key steps of the method are illustrated in Fig. 4.

For low metallicities, i.e. with $[M/\mathrm{H}] < 0.4$, where the MILES stars have [Mg/Fe] $\sim +0.4$, we use equation (3) to compute fully consistent models employing the MILES stellar spectra and α-enhanced isochrones, with no aid from theoretical stellar spectra. The MILES stars are selected to have [Mg/Fe] $= +0.4$ and [Fe/H] $= [M/\mathrm{H}] - 0.3$, according to equation (4). To compute the scaled-solar models, we follow a similar approach to that employed above for obtaining an α-enhanced SSP spectrum at high metallicity. However, in this case we apply a differential correction, $\gamma_\lambda(t, [M/\mathrm{H}], \Phi)$, that allows us to transform the reference MILES-based model with [α/Fe] $= +0.4$, $S_{\lambda_{\mathrm{MILES}}}(t, [M/\mathrm{H}], 0.4, \Phi, I_{0.0})$ to a self-consistent SSP spectrum with [α/Fe] $= 0.0$, $S_\lambda(t, [M/\mathrm{H}], 0.0, \Phi, I_{0.0})$.

For intermediate metallicities, namely $[M/\mathrm{H}] = -0.35$ and $[M/\mathrm{H}] = -0.25$, where most of the MILES stars have [Mg/Fe] ~ 0.2, we obtain for each [M/H] metallicity and each [α/Fe] abundance two SSP spectra using the two approaches described above. On one hand, we compute self-consistent scaled-solar SSP models that are fully based on MILES making use of the stars that have [Mg/Fe] ~ 0.0 and [Fe/H] $= -0.35$ and [Fe/H] $= -0.25$, respectively. Similarly, for the corresponding α-enhanced models we select stars with [Fe/H] $= -0.65$ and -0.55, respectively. Note that at such low [Fe/H] abundances, we take the advantage that most of the stars of MILES have [Mg/Fe] $\sim +0.4$. On the other hand, for

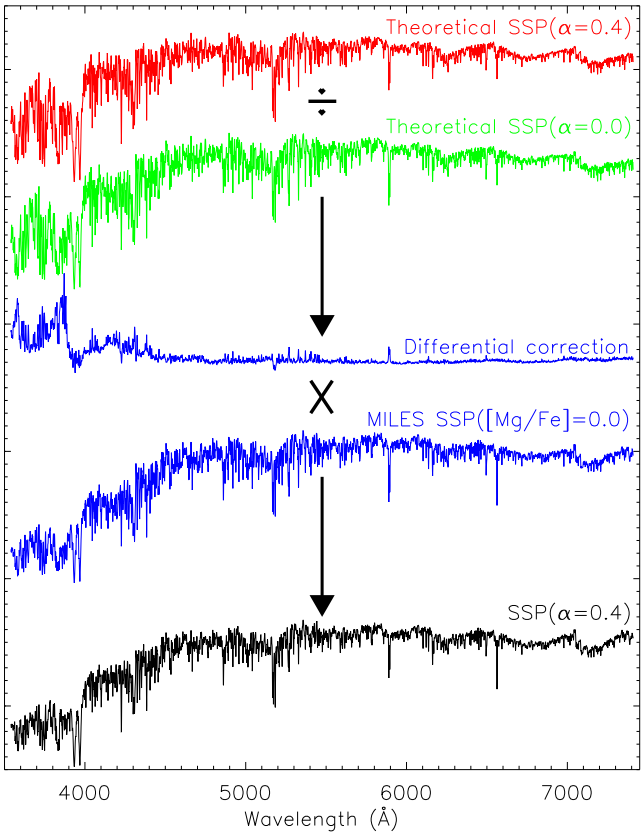

Figure 4. The method followed for computing an α-enhanced SSP spectrum with $[M/\mathrm{H}] = +0.06$. Fully theoretical α-enhanced ([Mg/Fe] $= +0.4$; shown in red) and scaled-solar (shown in green) SSP spectra, both computed with an α-enhanced isochrone, are employed to obtain a differential correction (in blue). This correction is applied to a reference SSP spectrum (also shown in blue), computed with MILES scaled-solar stars and the same α-enhanced isochrone. Therefore, we obtain a self-consistent SSP spectrum (shown in black) that is based on MILES, yet incorporates the [α/Fe] abundance ratio effects through this theoretical differential correction. All the models have $[M/\mathrm{H}] = +0.06$, 10 Gyr and Kroupa Universal IMF. See the text for a detailed description.

[10] It is worth noticing that, being similar, the theoretical stellar spectra adopt a uniform enhancement for all the α-elements, whereas the isochrones employ a different mixture for these elements, which on average yields the same enhancement. The variation of the abundance of individual α-elements has been shown to affect the temperature of the stars (see Lee et al. 2010 for an extended discussion). In addition, as described in Section 2.3.1, we only take into consideration the [Fe/H] and [Mg/Fe] (which is used as a proxy for the overall α-enhancement) estimates that are available for the MILES stars. Therefore, our models cannot be regarded as fully self-consistent as this is only possible for fully theoretical models that combine theoretical stellar spectra and isochrones computed with exactly the same element partition. With these important caveats in mind, our models are hereafter regarded as self-consistent (although not fully self-consistent) in the sense that the average α-enhancement value of the main ingredients of these models is similar.

each of these two [M/H] and two [α/Fe] values, we also compute a reference model based on MILES as well as two models based on the theoretical stellar spectral library. The latter are used to obtain the differential correction that allows us to bring the reference model on to the desired [α/Fe] abundance ratio. The use of these two self-consistent SSP models for each [M/H], [α/Fe] combination, allows us to significantly increase the total number of the MILES stars that are employed for the computation of the final SSP spectrum, which, therefore, has a higher quality than either of the above two SSP spectra, separately. It is worth reiterating that we employ this approach as our isochrones only have two possible [α/Fe] values, i.e. 0.0 and +0.4, whereas the MILES stars mostly have [Mg/Fe] $\sim$ +0.2. Finally, the last step consists of combining these two SSP spectra using equal weights. This equal-weighting is motivated by the fact that the quality parameters of these two SSP spectra (described in Section 4.1) are very similar for the vast majority of the cases, with differences being smaller than $\sim$10 per cent.

Our approach differs from other methods that apply a differential correction on the individual stellar spectra before synthesizing the SSP spectra (e.g. Prugniel et al. 2007; Conroy & van Dokkum 2012a). In our approach, $\gamma_\lambda(t, [M/H], \phi)$ is obtained from the SSP spectra calculated specifically for this purpose, without modifying the stellar spectra in our models, similar to the method proposed in Cervantes et al. (2007) and Walcher et al. (2009). This differs from the differential models built in Walcher et al. (2009) in that all our intermediate SSP spectra, either fully theoretical or reference MILES-based, are computed with the same population synthesis code. We also differ from, e.g. Conroy & van Dokkum (2012a) and Cervantes et al. (2007), in that we employ α-enhanced isochrones to obtain the α-enhanced SSP spectra. Our models also differ from the fully theoretical SSP SEDs of, e.g. Coelho et al. (2007), in that we always use MILES as our input library either completely, or in the form of the reference models. To our knowledge, this is the first time that SSPs using the differential approach and empirical stellar spectra have been built self-consistently.

Fig. 5 shows the flux ratios obtained by dividing fully theoretical (i.e. no MILES stars have been used here) SSP spectra versus the corresponding models computed with MILES (i.e. with no aid of theoretical stellar spectra) for the same SSP parameters. These ratios correspond to two representative metallicity and abundance ratio regimes, where it is possible to compute self-consistent SSP models based solely on the MILES stars: low-metallicity, α-enhanced and high-metallicity, scaled-solar. The two flux ratios show a large-scale variation of the continuum in the blue spectral region. These residuals include relevant features, which are related to carbon and some also to nitrogen, such as CNO at $\sim$3860 Å, Ca II H–K lines around $\sim$3950 Å, CN at $\sim$4150 Å, Ca at $\sim$4227 Å, CH at $\sim$4300 Å and C_2 at $\sim$4670 Å (see Tripicco & Bell 1995). Note that all these residuals are emphasized in the flux ratio obtained for the high-metallicity regime. These features are attributed, at least in part, to possible differences in the CN abundance between the theoretical and the MILES stars. Note that the CNO group is an important contributor to the total metal content and integrated opacity in a stellar photosphere, whose patterns do not necessarily follow the α-elements, iron-peak elements or global metallicity, but have their own significant contributions (e.g. McWilliam et al. 2008). Martins & Coelho (2007) find for the C-dominated features that the difference between the theoretical and empirical stars is emphasized for stars cooler than $\simeq$ 4500 K. These stars have a large impact on the old SSPs represented in Fig. 5.

We also see in Fig. 5 significant residuals for all the hydrogen lines, e.g. Hδ at $\sim$4100 Å, Hγ at $\sim$4340 Å, Hβ at $\sim$4860 Å, Hα at $\sim$6563 Å. This is a well-known problem in the theoretical models; the modelling of these lines with the assumption of local thermodynamic equilibrium (LTE) is able to reproduce the wings, but cannot match the core of the Balmer lines which form in the chromosphere and are not accounted for in the theoretical stellar spectra (see Martins & Coelho 2007).

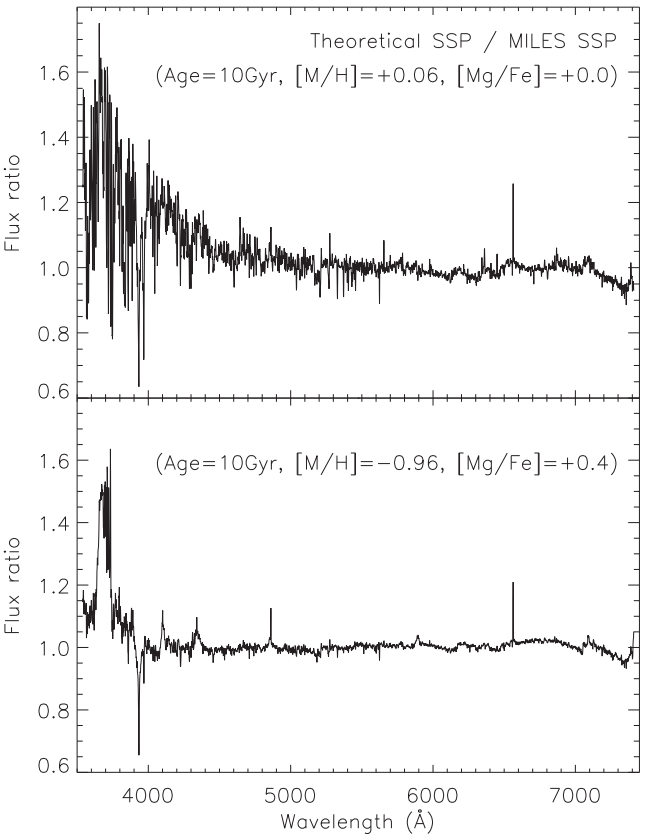

Figure 5. Flux ratio obtained by dividing an SSP SED computed with theoretical stellar spectra by the corresponding SSP model computed with MILES stars. In the top panel, the models are scaled-solar and have [M/H] = +0.06, whereas in the lower panel the models are α-enhanced with [M/H] = −0.96. All the models have 10 Gyr and a Kroupa Universal IMF.

Residuals for many metallic lines are seen along the whole spectral range in the high-metallicity regime. There are also large-scale residuals redward of $\sim$6000 Å, which are associated with molecular bands (mainly TiO). The contribution from these bands is only relevant for cool stars ($\leq$4500 K), but is a contribution that increases very rapidly with decreasing temperature. The modelling of these bands is challenging in part due to an incomplete knowledge of the molecular (and line) lists. Difficulties also arise since there may be differences between the temperature scales of the theoretical and empirical stars (see a discussion in Martins & Coelho 2007 and Coelho 2014).

We are aware that our method is not completely free from these residuals that are related to the use of the theoretical stellar spectra. However, their effects on our models are minimized as we only employ a differential correction in passing from, e.g. a scaled-solar to an α-enhanced abundance ratio. This approach avoids most of the uncertainties coming from the prescriptions adopted in the theoretical models such as the treatment of convection, turbulence, N-LTE effects, incomplete line lists, etc. See Coelho et al. (2007) for a detailed discussion on these differences, including a comparison of the resulting line-strength indices.

Finally, the very large residuals seen at wavelengths smaller than ∼3800 Å are artificial in the sense that they are a result of the stellar spectra calculations performed by Coelho et al. (2005) who only included the first 10 Hydrogen Balmer transitions. This results in artificially high fluxes in the wavelength range λλ 3650–3790 Å in stars of spectral types F and G, and artificial peaks centred around 3700 Å in the differential spectra computed from integrated light models. Obviously, this problem is far more severe for the young and/or metal-poor stellar populations. For this reason, we do not recommend the use of the spectral range blueward of ∼3800 Å for our model predictions that make use of the differential correction, i.e. the scaled-solar SSPs at low metallicities, and the α-enhanced SSPs at high metallicities.

3.3 Stellar spectra interpolation scheme

To compute each requested star spectrum, following equation (1), we use the local interpolation algorithm described in Vazdekis et al. (2003, Appendix B) and Paper I. For a given set of stellar atmospheric parameters, θ_0 (i.e. $5040/T_{\rm eff}$), $\log g_0$, $[{\rm Fe/H}]_0$, we interpolate the spectra of adjacent stars. The code identifies the MILES stars whose parameters are enclosed within a given box around the point in parameter space. If no star is found, this box is enlarged in each of these directions until suitable stars are found. This is done by dividing the original box into eight cubes, all with one corner at that point. This scheme is particularly useful for minimizing biases in presence of gaps and asymmetries in the distribution of stars around the point. The larger the density of stars around the requested point, the smaller the box. The sizes of the smallest boxes are determined by the typical uncertainties in the determination of the parameters according to Cenarro et al. (2001b). In each of the boxes, the stars are combined taking into account their parameters and the S/N of their spectra. Stars with similar parameters and higher S/N are given more weight according to a Gaussian function that is applied on each parameter axis.

Finally, the combined spectra in the different boxes, with stellar parameters close to the requested ones, are used to obtain the final MILES-based synthetic spectrum. In order to obtain the required atmospheric parameters, we employ a system of linear equations. Note that in some cases, usually in scarcely populated regions of parameter space, when a mathematical but unphysical (i.e. with at least one star weighting negatively) solution is found, we simply combine these stars according to the same weighting scheme applied previously for the individual boxes. This generally provides a star with parameters very close to those initially requested. We refer the reader to Vazdekis et al. (2003) for a full description of the algorithm. In this work, we have further minimized these unphysical cases by repeating the whole process after varying the initial set of parameters (θ_0 and $\log g_0$) in steps of 1 K and 0.1 dex for temperature and gravity, respectively, until a solution is found. We only allow a very modest deviation of these two parameters, i.e. 10 per cent of the initial box size, as estimated for that parametric point. We do not vary $[{\rm Fe/H}]_0$ as in doing so we could obtain solutions that would be biased towards the solar metallicity direction, particularly for the lowest and highest metallicity bins covered by the models.

We have extended this three-dimensional interpolation algorithm to be able to synthesize the star spectra taking into account the [Mg/Fe] parameter, as a proxy for [α/Fe]. However, we are constrained within the limits imposed by the library coverage of this parameter. For this reason, following the abundance pattern of MILES (Milone et al. 2011), at low metallicities our α-enhanced models are fully based on MILES, whereas for obtaining truly scaled-solar models we require first MILES-based reference models (that are then modified by theoretical differential corrections). At high metallicities, we make use of the reference models to obtain our α-enhanced predictions, whereas the scaled-solar models are fully based on MILES. Therefore, our approach, which makes use of the [Fe/H] and [Mg/Fe] estimates available for the stars of MILES, is fully optimized to exploit the potential of this library (and other empirical libraries).

To synthesize a stellar spectrum with given $[{\rm Mg/Fe}]_o$ and $[{\rm Fe/H}]_o$, we run our three-dimensional interpolator twice: in one case, $\alpha_{\rm l}$, we restrict the data base to stars with $[{\rm Mg/Fe}] \leq [{\rm Mg/Fe}]_o + \Delta[{\rm Mg/Fe}]$ and in the other, $\alpha_{\rm h}$, we use the stars with $[{\rm Mg/Fe}] \geq [{\rm Mg/Fe}]_o - \Delta[{\rm Mg/Fe}]$. $\Delta[{\rm Mg/Fe}]$ represents a fraction of the typical uncertainty in the determination of this parameter according to Milone et al. (2011). By adopting larger $\Delta[{\rm Mg/Fe}]$ values, we increase the number of stars involved in the process, but at the expense of increasing the probability of obtaining two stars with lower or higher [Mg/Fe] values than requested. After performing several tests, where we varied $\Delta[{\rm Mg/Fe}]$ for a representative set of stellar parametric regions, we adopted $\Delta[{\rm Mg/Fe}] = +0.05$. Note that this corresponds to approximately half the typical uncertainty in the determination of this abundance (see Milone et al. 2011). To estimate the [Mg/Fe] abundance of these stars, i.e. $\alpha_{\rm l}$ and $\alpha_{\rm h}$, we take into account the [Mg/Fe] estimates for all the stars that were involved in their calculation through the three-dimensional interpolation scheme. We then apply the same weights obtained during this process, which depend on their proximity to θ_0, $\log g_0$, $[{\rm Fe/H}]_0$. Note that these three stellar parameters are already in place for $\alpha_{\rm l}$ and $\alpha_{\rm h}$ through this interpolation. Finally, we combine them to obtain the desired stellar spectrum with $[{\rm Mg/Fe}]_{\rm o}$. In those cases where $\alpha_{\rm l}$ and $\alpha_{\rm h}$ stars have either lower or higher abundance ratio than $[{\rm Mg/Fe}]_{\rm o}$, we choose the star whose abundance value is the closest to the requested one. We note that such cases only occur in poorly populated parametric regions (e.g. at metallicity $[M/{\rm H}] = +0.4$ or $[M/{\rm H}] = -2.3$).

4 SSP SPECTRA

Table 1 summarizes the spectral properties of the newly synthesized SSP SEDs. The nominal resolution of the models is FWHM = 2.51 Å (Falcón-Barroso et al. 2011). This resolution is constant along the whole spectral range λλ 3540.5–7409.6 Å. The models have flux-calibrated response and are cleaned from telluric absorption residuals (Sánchez-Blázquez et al. 2006a). For computing the SEDs, we have adopted a total initial mass of 1 $M_\odot$. See also the caveats in Table 1 and Section 3.2 regarding the spectral range blueward of ∼3800 Å.

Table 1. Spectral properties of the model SEDs.

Spectral range	λλ 3540.5[a]–7409.6 Å
Spectral resolution	FWHM = 2.51 Å (σ = 64 km s^{-1} at 5000 Å)
Linear dispersion	0.9 Å pix^{-1}
Continuum shape	Flux-scaled
Telluric absorption	Cleaned
Units	$F_\lambda/L_\odot$Å$^{-1}M_\odot{}^{-1}$, $L_\odot = 3.826 \times 10^{33}$erg s^{-1}

Note. [a]Unsafe blueward of 3800 Å for the scaled-solar models with $[M/{\rm H}] < 0.06$ and α-enhanced models with $[M/{\rm H}] > -0.4$ (see Section 3.2).

Table 2. SSP parameter coverage.

IMF	
Mass range	0.1–100 $M_\odot$
IMF shape	Unimodal, Bimodal, Kroupa Universal[a], Kroupa Revised[a]
Unimodal IMF slope	$0.3 \leq \Gamma \leq 3.3$[b] (Salpeter IMF [c] if $\Gamma = 1.3$)
Bimodal IMF slope	$0.3 \leq \Gamma_b \leq 3.3$
Age range (Gyr)	
BaSTI-based models	0.030–14.0
Padova00-based models	0.063–17.8
Total metallicity ([M/H])	
BaSTI-based models	-2.27^{d},$-1.79^{e,f,g}$,$-1.49^{h,i,j,k,l}$,$-1.26^{m,n,o,p,q}$,-0.96^{r},−0.66,−0.35,−0.25,+0.06,+0.15,+0.26,$+0.40^{d}$
Padova00-based models	-2.32^{d},$-1.71^{s,t}$,−1.31,−0.71,−0.41,+0.0,+0.22
Abundance ratio ([α/Fe])	
Base models	MILES pattern
Scaled-solar[u]	+0.0
α-enhanced[u]	+0.4

Notes. [a]Same unsafe models as for bimodal IMF with $\Gamma_b = 1.3$.
[b]Unimodal IMF models unsafe for $\Gamma > 2.3$.
[c]Same unsafe models as for unimodal IMF with $\Gamma = 1.3$.
[d]Unsafe models.
[e]Unimodal BaSTI base models unsafe for $t < 0.09$.
[f]Bimodal BaSTI base models unsafe for ($t < 0.1$,$\Gamma_b < 2.3$), ($t < 0.09$,$2.3 \leq \Gamma_b \leq 2.5$), ($t < 0.08$,$2.8 \leq \Gamma_b \leq 3.0$), ($t < 0.06$,$\Gamma_b = 3.3$).
[g]Scaled-solar and α-enhanced models unsafe.
[h]Unimodal BaSTI base models unsafe for $t < 0.07$.
[i]Bimodal BaSTI base models unsafe for ($t < 0.07$,$\Gamma_b < 2.8$), ($t < 0.06$,$\Gamma_b = 2.8$), ($t < 0.05$,$\Gamma_b = 3.3$).
[j]Bimodal scaled-solar models unsafe for ($t < 0.08$,$\Gamma_b \leq 2.5$), ($t < 0.07$,$2.8 \leq \Gamma_b \leq 3.0$), ($t < 0.06$,$\Gamma_b = 3.3$).
[k]Bimodal α-enhanced models unsafe for ($t < 0.08$,$\Gamma_b \leq 2.8$), ($t < 0.07$,$3.0 \leq \Gamma_b \leq 3.3$).
[l]Unimodal scaled-solar and α-enhanced models unsafe for $t < 0.08$.
[m]Unimodal BaSTI base models unsafe for $t < 0.04$.
[n]Bimodal BaSTI base models unsafe for ($t < 0.04$,$\Gamma_b < 2.8$).
[o]Bimodal scaled-solar models unsafe for ($t < 0.07$,$\Gamma_b \leq 1.8$), ($t < 0.06$,$2.0 \leq \Gamma_b \leq 3.0$), ($t < 0.05$,$\Gamma_b = 3.3$).
[p]Bimodal α-enhanced models unsafe for ($t < 0.07$,$\Gamma_b \leq 2.0$), ($t < 0.06$,$2.3 \leq \Gamma_b \leq 3.0$), ($t < 0.05$,$\Gamma_b = 3.3$).
[q]Unimodal scaled-solar and α-enhanced models unsafe for $t < 0.07$.
[r]Unimodal scaled-solar and α-enhanced models unsafe for $t < 0.05$.
[s]Bimodal Padova00 base models unsafe for ($t < 0.075$,$\Gamma_b < 2.5$), ($t < 0.07$,$2.5 \leq \Gamma_b \leq 3.0$).
[t]Unimodal Padova00 base models unsafe for $t < 0.075$.
[u]See the caveats in Table 1 for the spectral range blueward of ∼3800 Å.

4.1 Quality of the SSP spectra

Table 2 lists the covered SSP parameters and also gives the ranges where these predictions cannot be considered safe.

To estimate the reliability of the synthesized SSP spectra, we follow the quantitative approach described in Paper I. For each SSP calculation, we use the same interpolation scheme described in Section 3.3, which synthesizes a representative stellar spectrum for a given set of atmospheric parameters. We compute a normalized quality parameter Q_n following equations 4– 6 of Paper I. Essentially, the higher the density of stars around the requested parametric point of each star along the isochrone, the higher the quality of the SSP spectrum. Q_n is determined by the MILES library, either when the model is computed on the basis of this library alone or when we make use of the MILES reference model. Our quality parameter is normalized with respect to a minimum acceptable value, which comes from a poor, but still acceptable, parameter coverage. We refer the interested reader to Paper I for a full description of the method. The only difference in this work is that in the process of synthesizing each requested stellar spectrum we obtain two values for this parameter, which correspond to the two stars required by our extended interpolation algorithm to match the [Mg/Fe] abundance ratio. We simply combine these values in the same way we did for these stars.

The reliability of the scaled-solar and α-enhanced SSPs with bimodal and unimodal IMFs is assessed in Figs 6 and 7, respectively. Each panel shows how Q_n varies with the SSP age and total metallicity. SSPs with Q_n values above 1 can be considered of sufficient quality, and therefore they can be safely used. We use the same scale for all the panels of these two figures. The figures show that the Q_n values corresponding to the scaled-solar and α-enhanced SSPs are very similar. The subtle differences seen between the upper and lower panels are attributed to differences in the temperatures of the selected stars along the isochrones, i.e. scaled-solar versus α-enhanced), and the [Fe/H] metallicity according to equation (4).

Although not shown, the Q_n values of the SSP models computed with a Kroupa Universal and Kroupa revised IMFs are similar to those obtained for a bimodal IMF with slope 1.3. The quality of the scaled-solar models is lower than that obtained for the base models, i.e. above 5 (see fig. 6 of Paper I). This is because in the computation of truly scaled-solar models we select stars according to both [Fe/H]and [Mg/Fe], whereas for the base models we only take into account [Fe/H]. In summary, the base models, either based on Padova00 or BaSTI have in general higher quality than the corresponding scaled-solar and α-enhanced models.

As expected, the higher Q_n values are obtained at solar metallicity. Q_n reaches a value of ∼4 for stellar populations in the range 1–10 Gyr for the SSP models with standard IMF slope (i.e. the left-hand panels of Figs 6 and 7).

We also see that the quality of the bimodal models is slightly higher than that computed with a single power-law IMF. This is

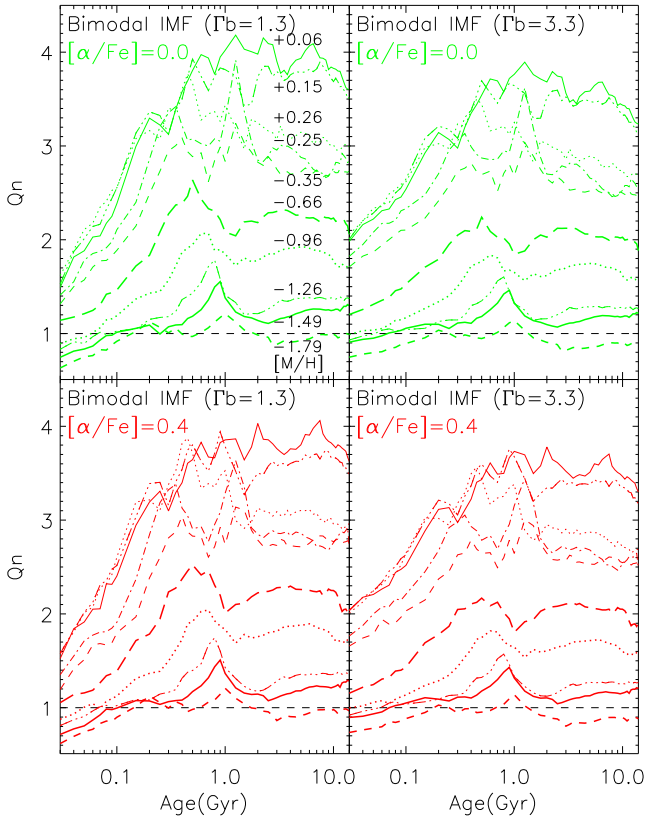

Figure 6. Reliability of the SSP spectra synthesized with a bimodal IMF with slope $\Gamma_b = 1.3$ (i.e. Kroupa-like; left-hand panels) and $\Gamma_b = 3.3$ (right-hand panels), for scaled-solar (upper panels) and α-enhanced (lower panels) models. The SSP age increases from left to right, whereas the total metallicity, $[M/H]$, is shown as different line types and thicknesses as given in the first panel. Only Q_n values above 1 are acceptable, as indicated by the horizontal black dashed line.

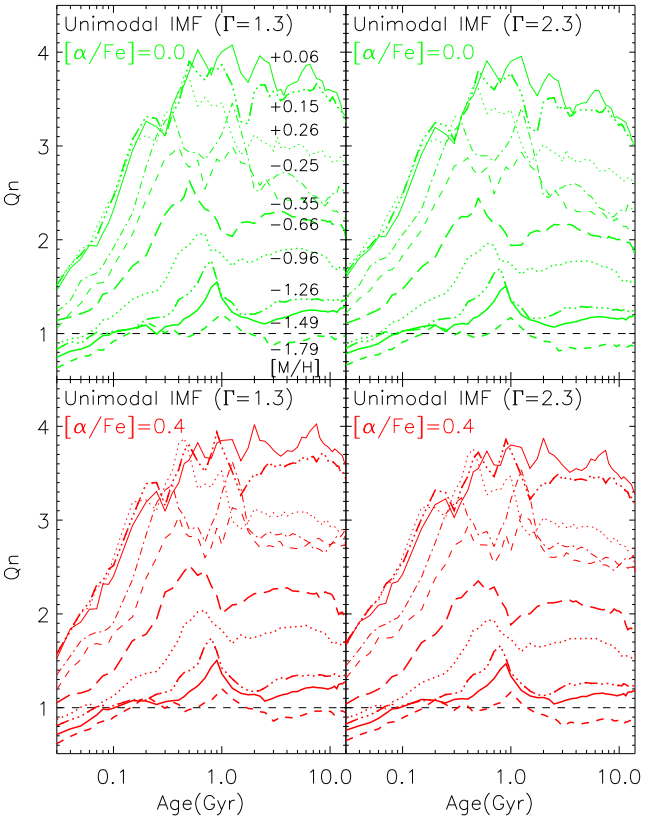

Figure 7. Same as in Fig. 6 for models with unimodal IMF with two slopes ($\Gamma = 1.3$, i.e. Salpeter, and $\Gamma = 2.3$).

due to the small number of VLM dwarfs with temperatures below ∼3500 K. This also explains the decay in quality for ages above ∼10 Gyr, as well as the drop seen for the models with a bottom-heavy IMF. Note that, as expected, this drop is more pronounced for the unimodal SSP models. Note also that the models with bimodal IMF and slope 3.3 yield very similar values to those obtained with unimodal IMF and slope 2.3. This is due to the fact that the relative fraction of dwarfs with masses below 0.5 $M_\odot$ is very similar for these two IMFs (see La Barbera et al. 2013).

Finally, the models with a *unimodal* IMF with $\Gamma > 2.3$ are unsafe due to an emphasized contribution of VLM stars with temperatures cooler than 3500 K, which are scarce in the MILES library. We refer the interested reader to Vazdekis et al. (2012) for the details regarding this limitation. Despite the claim of a steepening of the IMF slope with galaxy velocity dispersion, such extremely bottom-heavy IMF models do not seem to be required for fitting even the most massive galaxies, always with $\Gamma < 2.3$ (e.g. La Barbera et al. 2013; Spiniello et al. 2014).

The variation of the Q_n values with age at a given metallicity originates from the varying number density of stars with temperature, such as the turn-off stars, which become cooler with increasing age. This is illustrated by looking at the number density of stars around solar metallicity (i.e. along a vertical line in the right-hand panel of Fig. 3). For ages smaller than 1 Gyr, we also see a decrease in quality due to a decrease in the number of stars with high temperatures.

These figures also show that the derived quality depends on metallicity. In general, the more we depart from solar, the lower the Q_n value. Unlike the base models (see fig. 6 of Paper I), the SSPs with supersolar metallicity show higher Q_n values than the models with $[M/H] = -0.35$ and -0.25 shown here. This is because at these intermediate metallicities the required reference models, either with $[\alpha/Fe] = +0.0$ ($S_{\lambda_{MILES}}(t, [M/H], 0.0, \Phi, I_{0.4})$) or $[Mg/Fe] = +0.4$ ($S_{\lambda_{MILES}}(t, [M/H], 0.4, \Phi, I_{0.0})$), are composed of significantly fewer stars, since the majority have $[Mg/Fe] \simeq +0.2$. For the base model, we neglect this parameter and therefore all these stars are taken into account in the interpolation scheme. The drop in quality is more pronounced for lower metallicities. Overall, the very youngest models are not reliable for metallicities below $[M/H] \sim -1.0$. The minimum acceptable metallicity for the α-enhanced and scaled-solar models is reached for models with $[M/H] = -1.49$. Note that this limit is lower for the base models, which are safe for $[M/H] = -1.79$ (BaSTI) with ages above ∼0.1 Gyr and for $[M/H] = -1.71$ (Padova00) with ages above ∼0.08 Gyr. Finally, we also see that the α-enhanced and scaled-solar predictions are unsafe for ages younger than ∼0.07 Gyr. In Table 2, we provide more detailed information on which regions of parameter space (age, metallicity, IMF slope and IMF shape) cannot be considered fully safe.

Models outside the safe ranges discussed here should not be considered suitable for detailed spectroscopic studies that employ line strengths or a full spectrum-fitting approach. However, these models might be still useful, with caveats, for some applications such as, e.g. broad-band colours or for more complex populations, which are dominated by SSPs within the safe ranges. We also computed scaled-solar and α-enhanced models with $[M/H] = +0.4$ and

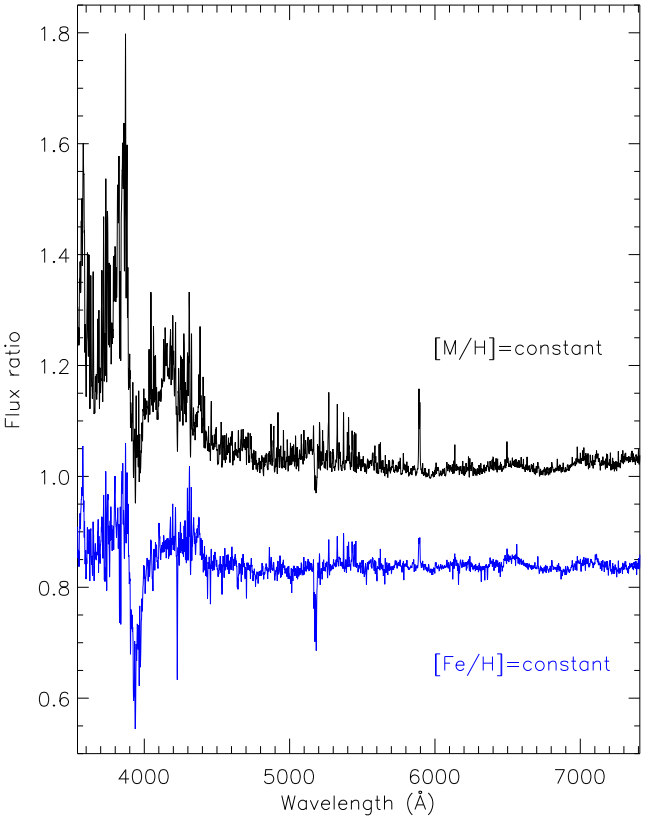

Figure 8. Flux ratios obtained by dividing an α-enhanced versus a scaled-solar SSP model with constant iron content ([Fe/H] $= -0.25$, in blue), and constant total metallicity ([M/H] $= +0.06$, in black). Both flux ratios correspond to models with 10 Gyr and Kroupa Universal IMF.

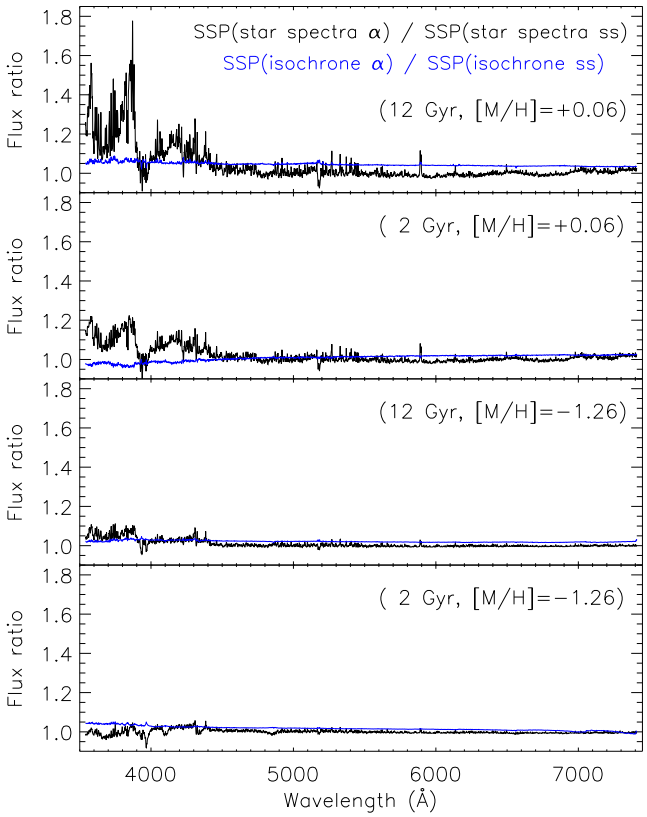

Figure 9. Flux ratios obtained by dividing two SSP spectra computed with the same isochrones but in one case employing α-enhanced spectra and in the other scaled-solar stellar spectra, shown in black. The ratios resulting from dividing two SSP spectra computed with the same stellar spectra but varying the abundance of the isochrones are shown in blue. The results for two total metallicity values (+0.06 and −1.26) and two ages (2 and 12 Gyr) are shown as quoted within the panels.

−2.3, which are unsafe, but that could help us to visualize trends with metallicity of e.g. line strengths.

4.2 Effects of varying the abundance on the SSP spectra

The effects of varying the α-elements abundance ratio at constant total metallicity, [M/H], and at constant [Fe/H] abundance can be assessed from the flux ratios shown in Fig. 8. When the total metallicity is held constant, we see a significant increase in flux at wavelengths shorter than about 4500 Å. This behaviour is also seen when dividing stellar spectra with varying [Mg/Fe], both for empirical stars from the MILES library and for theoretical stellar spectra. We refer the reader to the extensive study performed in Sansom et al. (2013) for more details (see also Cassisi et al. 2004). This excess of blue flux is attributed to the fact that the α-enhanced element mixture has a decreased iron abundance, and therefore lower opacity, with respect to the scaled-solar model of similar total metallicity (irrespective of the exact value of the term multiplying the [Mg/Fe] abundance in equation 4). This is confirmed by the modest excess in blue flux seen in the bottom spectral ratio of Fig. 8, which corresponds to models with similar [Fe/H] abundance.

In addition, we see similar spectral features blueward of ∼4500 Å in both the spectral ratios, although generally these are less pronounced when [Fe/H] is held constant. These residuals are mainly related to the Ca II H–K and Ca I features around ∼3950 Å and ∼4227 Å, respectively, the CN molecular absorptions at ∼4150 Å and in the complex blueward of ∼3900 Å and the CH at ∼4300 Å and also within this blue complex. These residuals likely originate in intrinsic differences between the C, N and O and Ca abundances between the MILES stars and the theoretical stellar spectra of Coelho et al. (2005). In our SSP model computation, we only have considered the [Mg/Fe] and [Fe/H] estimates for the MILES stars, as the measurements for the other elements are incomplete for these stars. However, there are indications of such varying abundance patterns among the MILES and the theoretical stars. For example, applying the relation between [C/Fe] and [Fe/H] of Takeda & Honda (2005), i.e. [C/Fe] $= -0.21$[Fe/H]$+0.014$, derived for a sample of 160 FGK dwarfs/subgiants, with metallicities around the solar value, we obtain [C/Fe] $\sim +0.07$ for [M/H] $= +0.06$ and [α/Fe] $= +0.4$, whilst the theoretical stellar spectra adopt a scaled-solar abundance for carbon. Moreover, unlike in the theoretical stellar spectra, for which [O/Fe] tracks [Mg/Fe], observationally the abundances of these two α-elements are slightly decoupled around solar metallicity (e.g. Soubiran & Girard 2005). In addition, the CNO group represents an important fraction of the total metallicity, contributing significantly to the integrated opacity in a stellar photosphere (see the extensive discussion in Sansom et al. 2013).

Fig. 8 also shows that the Fe lines at, e.g. ∼5270 and 5335 Å, are deeper in the scaled-solar models than the α-enhanced models (positive residuals in the ratios plotted). This happens also at fixed [Fe/H], as noted in Barbuy et al. (2003) and Coelho et al. (2005): Mg is an important electron donor and as such can act to lower

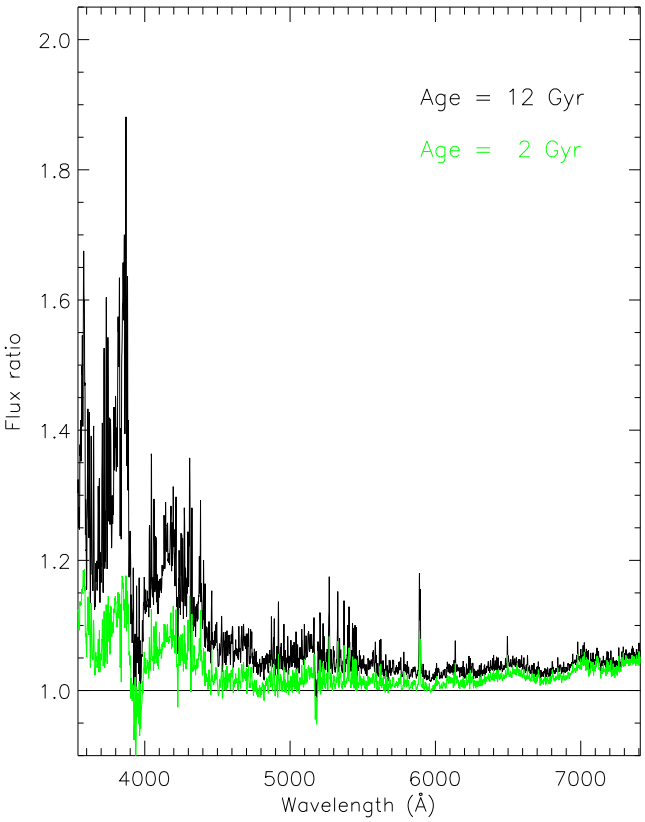

Figure 10. Flux ratios obtained by dividing α-enhanced versus scaled-solar SSP spectra of 2 Gyr (green) and 12 Gyr (black). All the flux ratios correspond to models with solar (total) metallicity and Kroupa Universal IMF.

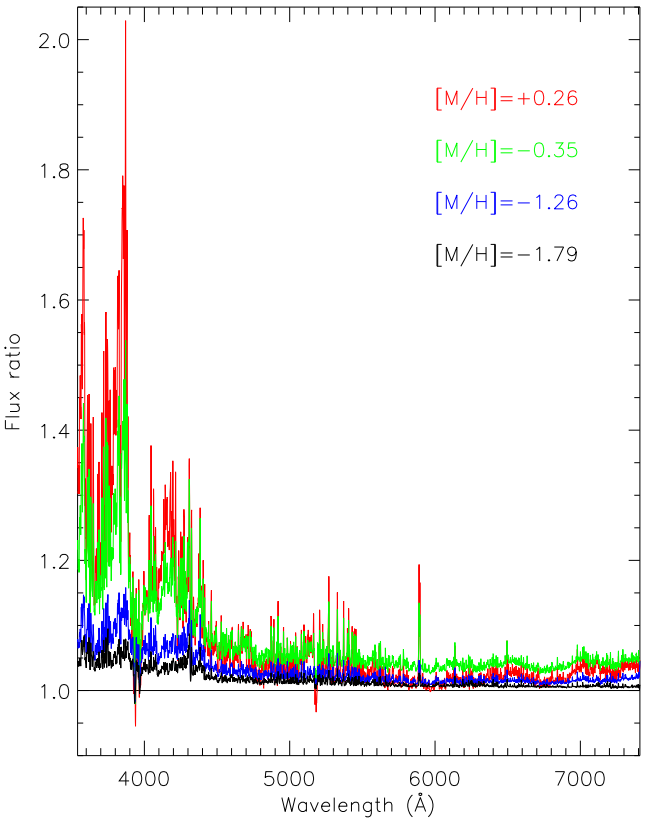

Figure 11. Flux ratios obtained by dividing α-enhanced by scaled-solar SSP spectra with constant total metallicity. The flux ratios are shown for four metallicity values: $[M/H] = -1.79$ (black), -1.26 (blue),-0.35 (green) and $+0.26$ (red). All the flux ratios correspond to models of 10 Gyr with a Kroupa Universal IMF.

the true continuum. This effect is also seen for the Na I doublet at ∼5895 Å (see e.g. Vazdekis et al. 1997; Coelho et al. 2007) and, to a lesser degree, in the variations of the molecular features redward of ∼6000 Å. In general, these features, although weaker, are also present in the flux ratio obtained when [Fe/H] is kept constant. The exception here is the Mg feature at ∼5175 Å, where the [Mg/H] abundance of the two SSP spectra differ by −0.3 dex. See Section 5 for more details.

In Fig. 9, we separate the effects of the isochrones from those of the stellar spectra on our SEDs. We show the results for two ages (2 and 12 Gyr) and two total metallicities with $[M/H] = +0.06$ and -1.26. For each age and metallicity, we compute SSP spectra with two different isochrones (α-enhanced and scaled-solar), but without changing the abundance ratios of the stellar spectra. In addition, we also show the flux ratios obtained when using the same isochrones, but varying the abundance ratios of the stellar spectra. The flux ratios obtained indicate that the effects of the stellar spectra are significantly more relevant than the isochrones, particularly for solar metallicity and old stellar populations, confirming the previous findings by Coelho et al. (2007, section 6.4) and Lee et al. (2009a). The impact of the stellar spectra is mostly seen in the excess of flux in the blue, the strengths of many features and, to a lesser degree, on some molecular bands. However, the effects of the isochrones are mostly reflected in the continuum over the whole spectral range covered by the models. Although smaller than the effects of the stellar spectra, the impact of the isochrones is significant for the SSPs of 2 Gyr. Note also the small difference in flux between the two flux ratios.

Fig. 10 shows the flux ratios obtained by dividing SSP spectra with the same total metallicity (solar), but with two different [α/Fe] abundances, for two ages (2 and 12 Gyr). We see that the impact on the spectra due to the [α/Fe] abundance is significantly greater at old ages. Such behaviour is expected since the SSPs with 2 Gyr include hotter stars, for which the effects of varying the [α/Fe] abundance are considerably smaller (see fig. 9 of Sansom et al. 2013).

Finally, Fig. 11 illustrates the effects of varying the [α/Fe] abundance as a function of the total metallicity, [M/H], while keeping constant the age. We see both a larger excess in blue flux and a larger line feature residuals, for higher metallicities. As was the case when varying the SSP age, this behaviour is also expected when varying the metallicity since the stellar temperatures decrease with increasing metallicity.

5 LINE-STRENGTH INDICES

In this section, we study the behaviour of the line-strength indices predicted by our new models. We measure the indices on the synthesized SSP spectra at resolution 8.4 Å (FWHM) to match the resolution of the LIS-8.4 Å system that was introduced in Paper I. Unlike the Lick/IDS system (Worthey & Ottaviani 1997), all these indices are measured with the same resolution on a flux-scaled response.

To illustrate the main behaviours and differences of our models, we first compare a number of representative line strengths from our

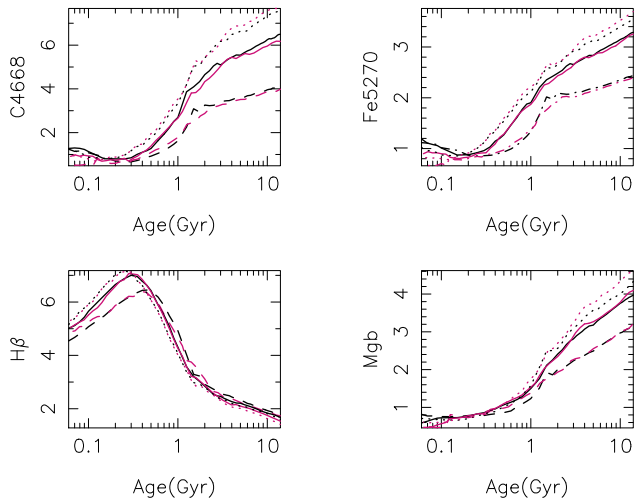

Figure 12. Base models with two different isochrones; black are BaSTI and magenta lines are Padova00. Three different metallicities are plotted for BaSTI (Padova00), $[M/H] = -0.35(-0.40)$, $+0.06(0.00)$ and $+0.26(+0.22)$, with dashed, solid and dotted lines, respectively. All the models have a Kroupa Universal IMF. Note that whereas the models based on the BaSTI isochrones reach ages as young as 30 Myr, the Padova00-based models stop at 63 Myr (see Table 2). All the index measurements were obtained in the LIS-8.4 Å system (Paper I), i.e. at FWHM = 8.4 Å and flux-calibrated response.

base models computed with the Padova00 and BaSTI isochrones. In the following subsections, we compare the predictions from our scaled-solar and α-enhanced models for a larger number of commonly used line indices, which include those of Lick. We have organized these indices according to their sensitivities to relevant parameters of the stellar populations.

5.1 Line strengths of the base models

Fig. 12 shows the predictions of some line-strength indices as a function of age for the base models, computed with BaSTI and Padova00 isochrones. The predictions are shown for three different metallicities. As can be seen, the differences found using these two sets of isochrones are very small. For old stellar populations, the BaSTI models give index values that are slightly higher for the Balmer lines (around 0.1–0.2 Å for old stellar populations), and slightly lower for the three metallicity indices shown in the figure. Note that the given $[M/H]$ values are slightly higher for BaSTI than for Padova00. Therefore, when comparing the BaSTI model predictions to observational data, we expect the derived ages and metallicities to be slightly higher than when using the Padova00 model predictions. There are also differences for intermediate-aged stellar populations where the AGB contribution is relevant, due to the differences in the treatment of this late evolutionary stage (see Section 2.2).

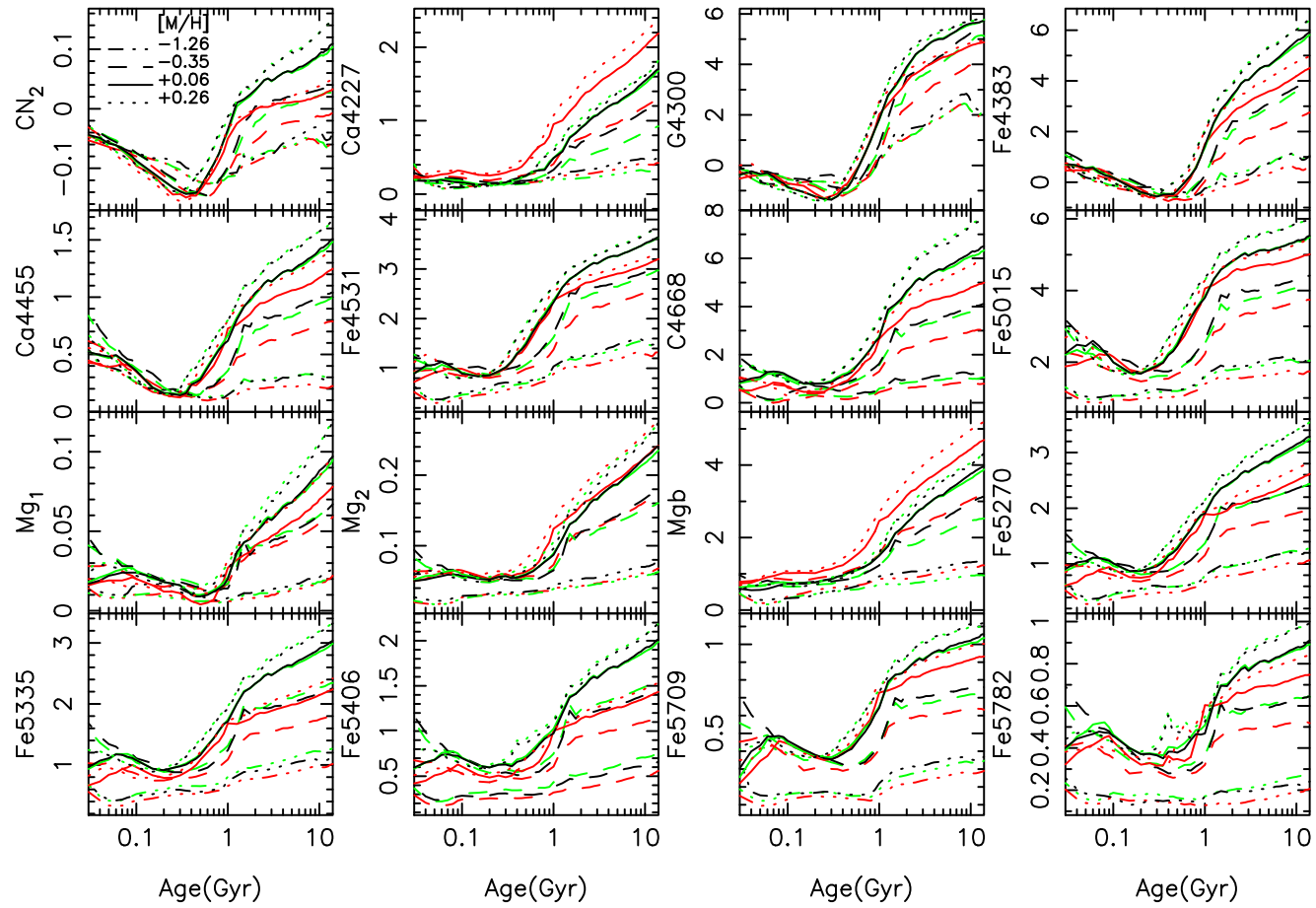

Figure 13. Variations of a representative set of Lick line-strength indices with age for four different metallicities, $[M/H]=-1.26$ (dot–dashed line); $[M/H] = -0.35$ (dashed line) $[M/H] = 0.0$ (solid line) and $[M/H] = +0.26$ (dotted line). Colours represent three different models built with the BaSTI isochrones; red: α-enhanced models, green: scaled-solar models and black: base models. As in Fig. 12, all the index measurements are performed in the LIS-8.4 Å system, i.e. at 8.4 Å (FWHM) and flux-calibrated response.

5.2 Line strengths with varying abundance ratios

Fig. 13 shows the predicted time evolution of our BaSTI-based SSP models for a selection of line-strength indices measured from the scaled-solar, α-enhanced and base models. All these models are computed with a Kroupa Universal IMF. We have plotted the results for four different metallicities. Perhaps, most readily seen in this set of plots is that, for the majority of indices, the effect of the different [α/Fe] ratios is largest at old ages. For some indices (e.g. Mg_1, Fe 5015, Fe 5335, Fe 5406, Fe 5709, Fe 5782), differences also appear at very young ages (<0.1 Gyr), with these differences increasing at high metallicities. These differences come from the influence of supergiant stars at these young ages.

The base models have the abundance pattern of the Milky Way (MILES) stars, although the isochrones are scaled-solar. Therefore, at low metallicities ($[M/H] < -0.4$), the base models are more similar to the α-enhanced models, while at high metallicities they are almost identical to the scaled-solar models.

As expected, those indices sensitive to Fe (Fe 4383, Fe 4531, Fe 5015, Fe 5270, Fe 5335, Fe 5406, Fe 5709 and Fe 5782) show lower values in the α-enhanced models than in the scaled-solar models. This occurs because the models are built at constant metallicity and, therefore, the α-enhanced models have a lower Fe content (i.e. $[M/H] - 0.3$, according to equation 4). Note however that the effect on the Fe 5015 index is relatively smaller in comparison to the other Fe-sensitive indices, as a result of its sensitivity to Ti abundance, which is enhanced in the α-enhanced models (Lee et al. 2009a; Johansson et al. 2012). The same applies to Fe 4531 for which we also see that the α-enhanced model lines are closer to the corresponding base model lines (see also fig. 9 in Lee et al. 2009a) This behaviour is also seen for fixed [Fe/H], as Mg, i.e an important electron donor, tends to lower the true continuum (Barbuy et al. 2003; Coelho et al. 2005).

It is worth noting that, while Mg*b* is higher in the α-enhanced models than the scaled-solar models, as expected due to its sensitivity to the Mg abundance, the same is not true for Mg_1 and Mg_2. In fact, the Mg_1 indices are stronger in the scaled-solar models at all metallicities. It is known that Mg_1 has a greater sensitivity to C than Mg. In the α-enhanced models, all the non-α elements are depleted relative to the scaled-solar models, including C. This behaviour of Mg_1 is similar to that of the CN_2 and C_2 4668 indices, which have higher sensitivities to variations of N and C abundances, respectively.

Similar to the case for Mg*b*, Ca 4227 is also much stronger in the α-enhanced models than in the scaled-solar models, as expected due to the sensitivity of this index to variations of Ca. Note that Ca 4227 is also anticorrelated with the CN feature that affects its blue pseudo-continuum, hence the Ca 4227 index decreases in strength in the scaled-solar models. As with the Mg*b* index, the predictions of the α-enhanced models are similar to those of the base models at low metallicities. This is as expected due to the high [α/Fe] of the base models at low metallicities (reflecting the intrinsic MILES abundance pattern). The Ca 4455 index, however, does not depend on the Ca abundance, and behaves more like an Fe index (e.g. Tripicco & Bell 1995; Lee et al. 2009a).

Finally, in Fig. 14 we make use of these new model predictions to probe the sensitivity of the combined [MgFe] and [MgFe]′ indices to the α-enhancement. We confirm the results of Thomas et al. (2003a). These authors employed models that predict the strengths of a number of line indices with varying abundances by implementing response functions derived from theoretical spectra. We conclude that these two indices can be safely used to estimate the total metallicity, [M/H], of stellar populations with non-solar [Mg/Fe] abundance ratios.

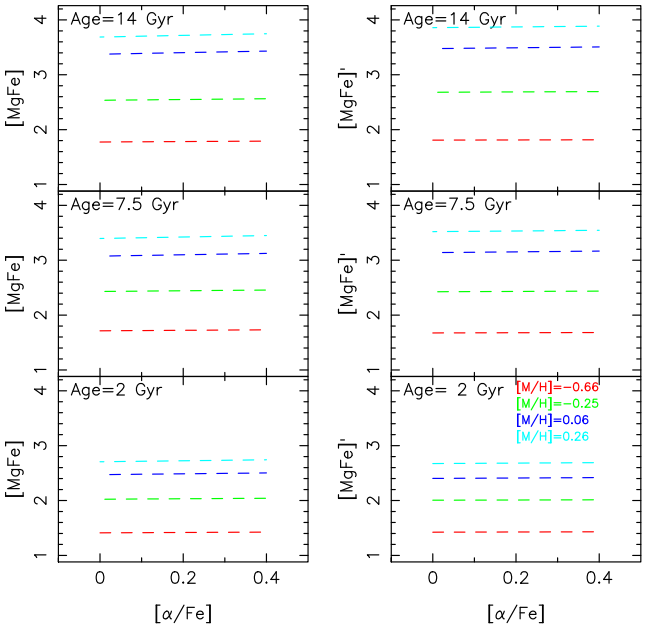

Figure 14. [MgFe] (left-hand panels) and [MgFe]′ (right-hand panels) indices as a function of [α/Fe], for SSP models with three different ages (14, 7.5 and 2 Gyr) from top to bottom panels, and four different metallicities ($[M/H] = -0.66, -0.25, +0.06$ and $+0.26$, in red, green, blue and cyan, respectively. All the models have a Kroupa Universal IMF. Note that the two indices are almost insensitive to this abundance ratio.

5.3 Age-sensitive line-strength indices

Fig. 15 shows the variation of different age-sensitive indices with age predicted by our models. The sensitivity of the Hβ index to α-enhancement is much less than that of the higher order Balmer lines (Hδ and Hγ). This is particularly true at high metallicities, where the base, scaled-solar and α-enhanced models have similar values. The dependence of $H\beta_o$ on [α/Fe] ($\sim$0.2 Å at solar metallicity and old ages) is higher than that of Hβ (almost negligible), confirming the result of Cervantes & Vazdekis (2009). Also the dependence of Ca II H–K on [α/Fe] is very strong, especially for old ages. This dependence also increases with metallicity. Note that Ca is another α-element and, therefore, in the adopted theoretical stellar spectra is also enhanced in the α-enhanced models. Similar behaviour is seen for the D 4000 break. These variations are expected given the residuals obtained in Fig. 8 (see also Section 4.2). Note also the increase in the strength of all the Balmer indices for the models with the oldest ages and the lowest metallicity, i.e. $[M/H] = -1.26$. This effect is due to the increased contribution of the HB stars at such old ages and low metallicities (e.g. Lee, Yoon & Lee 2000).

Fig. 16 illustrates the effects of α-enhancement on various Balmer line index definitions. The figure shows the pseudo-continua and feature bandpass definitions for the four indices of Worthey & Ottaviani (1997), (i.e. $H\delta_A$, $H\delta_F$, $H\gamma_A$, $H\gamma_F$), one of the Hγ indices of Vazdekis & Arimoto (1999) ($H\gamma\sigma_{200}$, i.e. the one that is suitable for the resolution of the LIS-8.4 Å system) and the standard and optimized index definitions for the Hβ feature of Trager et al. (1998) (Hβ) and Cervantes & Vazdekis (2009) ($H\beta_o$), respectively.

Fig. 16 confirms the claim of Thomas et al. (2003a) that the higher order Balmer lines are more sensitive to the α-enhancement than

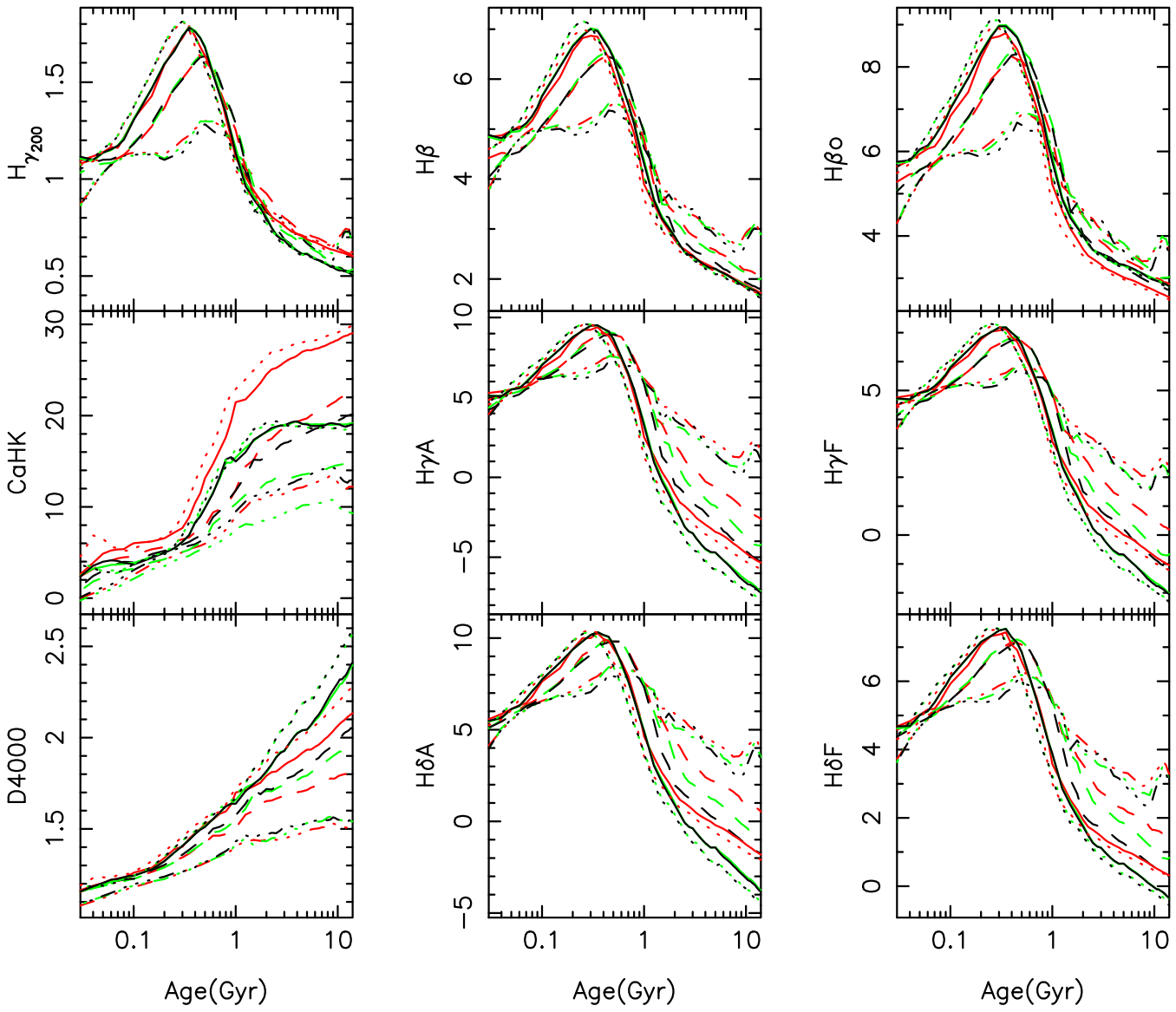

Figure 15. Predicted variation of various age-sensitive line-strength indices in the LIS-8.4 Å system as a function of age for four different metallicities, $[M/H] = -1.26, -0.35, +0.06$, and $+0.26$ (dot–dashed, dashed, solid and dotted line, respectively). Red line: α-enhanced models, green: scaled-solar models and black: base models. All the models have a Kroupa Universal IMF.

Hβ_o. However, we see that such an effect is mostly caused by the sensitivity of the surrounding pseudo-continua of the Hδ and Hγ lines to the abundance ratio, which is significantly lower for the Hβ index (see also figs 17 and 18 in Lee et al. 2009a). Essentially, the narrower the index definition, the smaller the sensitivity of the index to the α-enhancement. For example, Hγ_A has a larger dependence on the α-enhancement than Hγ_F, while H$\gamma\sigma_{200}$ has the lowest sensitivity to this parameter as shown in Fig. 15.

Fig. 16 also shows two small, but significant, residuals (between ∼4850 Å and ∼4900 Å) seen in emission in this flux ratio, affecting the Hβ and Hβ_o index definitions (see also the spectra of figs 12, 13 and 14 in Lee et al. 2009a). One of these residuals (i.e. the bluest) affects the feature bandpass of the two indices, whereas the second (the reddest) is placed within the red pseudo-continuum corresponding to the Hβ index. We see that the very small sensitivity of the Hβ index to the [α/Fe] abundance ratio is due to the fact that the reddest residual compensates in part the contribution to the feature bandpass from the bluest residual. However, the red pseudo-continuum of the Hβ_o index is located in a valley within this flux ratio, which has a similar flux level to the blue pseudo-continuum. Therefore, the Hβ_o index includes the full effect of the residual affecting the bandpass of this index. This residual corresponds to Fe-peak elements, including Chromium, that affect the red wing of the Hβ absorption.

The higher sensitivity of Hβ_o to [α/Fe] was first shown in Cervantes & Vazdekis (2009), also employing the Coelho et al. (2005) model stellar spectra. However, these authors also found the opposite behaviour, i.e. a larger sensitivity of the Hβ index to [α/Fe] than Hβ_o, when using the Munari et al. (2005) stellar spectra to obtain the differential correction. This disagreement possibly originates in differences in the line lists adopted for computing these two sets of theoretical stellar spectra.

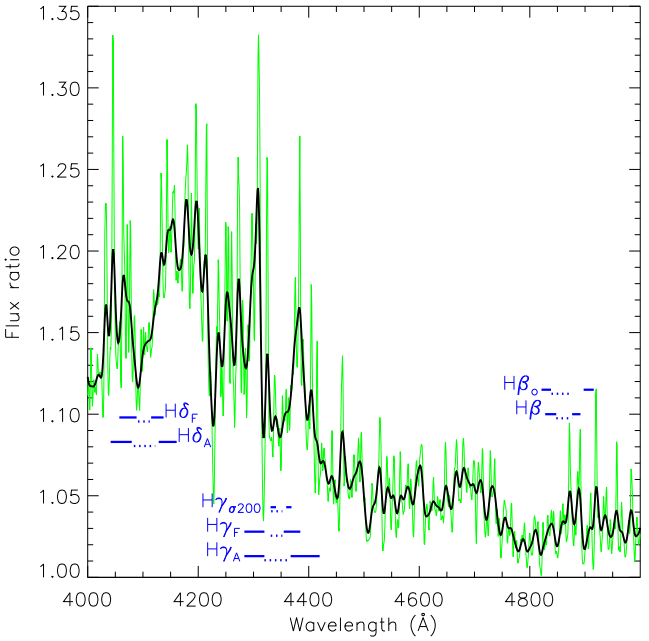

Figure 16. Flux ratio obtained by dividing an α-enhanced SSP model by a scaled-solar SSP model, with age 10 Gyr, $[M/\mathrm{H}] = +0.06$ and Kroupa Universal IMF, in the spectral region covered by Hδ, Hγ and Hβ. The flux ratio is shown at two resolutions FWHM = 2.51 Å (i.e. the nominal resolution of the models) and 8.4 Å (i.e. the LIS-8.4 Å system), in thin green and thick black lines, respectively. The pseudo-continua and feature bandpasses of various index definitions for these features are shown in blue solid and dotted lines, respectively.

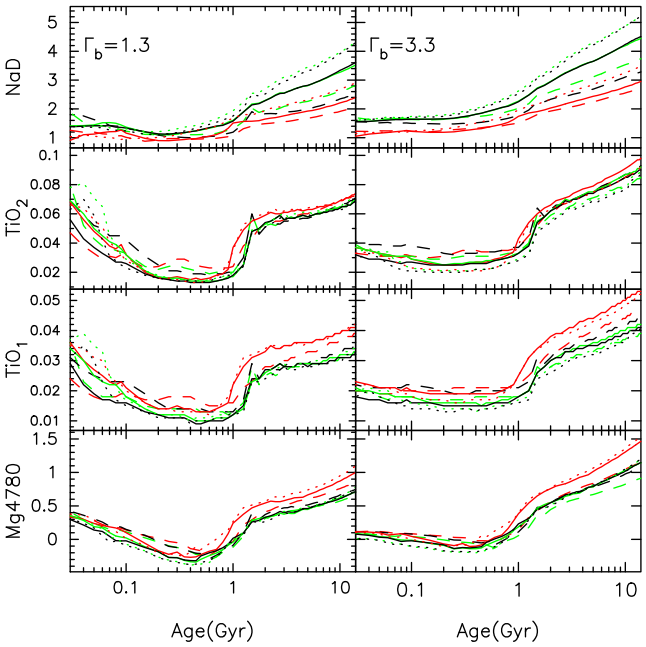

Figure 17. Variation of some IMF-sensitive indices with age of SSPs with a bimodal IMF with slope $\Gamma_b = 1.3$ (left-hand panels) and $\Gamma_b = 3.3$ (right-hand panels) for the three different models presented here; α-enhanced (red), scaled-solar (green) and base (black). The index measurements are shown for three different metallicities with different line-styles: $[M/\mathrm{H}] = -0.35$ (dashed), $[M/\mathrm{H}] = +0.06$ (solid) and $[M/\mathrm{H}] = +0.26$ (dotted). All the index measurements are in the LIS-8.4 Å system.

5.4 IMF-sensitive line-strength indices

Fig. 17 shows the variation of four gravity-sensitive indices (La Barbera et al. 2013) with age for the three models presented here (i.e. base, scaled-solar and α-enhanced models). The figure shows the index measurements for SSPs with a bimodal IMF with slope $\Gamma_b = 1.3$, similar to Kroupa Universal, and $\Gamma_b = 3.3$, i.e. a bottom-heavy IMF. These values cover the range of bimodal IMF slopes required to match Sloan Digital Sky Survey (SDSS) ETGs with velocity dispersions in the range 100–300 km s^{-1} (La Barbera et al. 2013). The index measurements are shown for three different metallicities. The two TiO indices show the highest sensitivities to the IMF, whereas the NaD index shows the lowest sensitivity to this parameter. However, the NaD index does show the largest sensitivity to $[\alpha/\mathrm{Fe}]$, whereas the $\mathrm{TiO_2}$ index is almost insensitive to this abundance ratio. These results are in agreement with recent works that employ either a different set of model stellar spectra than the ones used here, e.g. Spiniello et al. (2014), or fully empirical evidence based on stacked galaxy spectra from the SDSS (La Barbera et al. 2013).

The highest sensitivity to the IMF is seen for the models with the oldest ages. For models with $\Gamma_b = 1.3$, we find a plateau, with only a modest increase with age, for ages between 2 and 10 Gyr for the $\mathrm{TiO_1}$ and $\mathrm{TiO_2}$ indices and, to a lesser degree, for Mg 4780. For this age regime, these indices mostly depend on the IMF, whereas for older populations there is also a dependence on age (see La Barbera et al. 2013). Interestingly, the α-enhanced models show a slightly larger dependence on metallicity in comparison to the scaled-solar and base models. We also find that the $\mathrm{TiO_2}$ index, and the other IMF-sensitive indices, which show little sensitivity to the age for the standard IMF slope (i.e 1.3), become more sensitive to this parameter for larger IMF slopes, such as those shown in the right-hand panels of Fig. 17.

Another interesting aspect is the high values of the $\mathrm{TiO_1}$ and $\mathrm{TiO_2}$ indices for ages below 0.1 Gyr for the models with $\Gamma_b = 1.3$, index values which are similar to those obtained for ages around ∼8 Gyr. This behaviour is attributed to the influence of supergiant stars at these young ages. Such an increase is likely to continue to even younger ages where the contribution of this evolutionary phase peaks at around 10 Myr. Similar behaviour is seen for other IMF-sensitive features such as the Ca II triplet around ∼8500 Å and the CO bandhead at 2.3 μ (e.g. Mayya 1997). It is not surprising to see that there is no such increase at these young ages for the bottom-heavy IMF models. The steeper the IMF, the larger the fraction of mass locked in low-mass stars. In principle, it could be appealing to consider that the high TiO values observed in massive ETGs, which suggest a bottom-heavy IMF (e.g. La Barbera et al. 2013), may result in part by a contribution from such young stellar populations. However, such a contribution would have a significant impact on the measurements of other line indices in the optical range which is not seen.

6 COLOURS

In this section, we focus on the photometric predictions from our new set of models. To derive the synthetic colours, we adopt Vega magnitudes for the Johnson bands, *B* and *V* (Buser & Kurucz 1978; see also Falcón-Barroso et al. 2011 for further details on our definition of Vega magnitudes) and the AB system for the SDSS filters: *u*, *g*, *r* and *i*.

6.1 Synthetic *u* and *i* magnitudes

The MILES spectral range (3540.5–7409.6 Å) does not fully cover the wavelength range spanned by the *u* and the *i* SDSS filters, as the *u* passband starts at ∼3005 Å and the *i* band extends up to 8605 Å. Therefore, in order to have reliable synthetic magnitudes in these bands, we need to correct for the missing flux blueward and redward of the MILES spectral range. We do this by using a similar methodology to that adopted in Ricciardelli et al. (2012), which consists of computing the magnitude in the part of the filter covered by the model and then correcting it for the missing flux.

To obtain the missing flux blueward of the starting point of MILES, i.e. between 3005 and 3540.5 Å, we use new model SEDs that employ the NGSL stellar library, as prepared in Koleva & Vazdekis (2012) and Vazdekis et al. (in preparation). These models, which are computed with the same code used here, extend the spectral range down to ∼1680 Å. Thus, for a given MILES SSP, the *u* magnitude is obtained from the flux through the *u* filter redward 3540.5 Å and then correcting this value by the missing flux obtained from the corresponding NGSL-based SSP. Note that the missing flux correction in the blue is $\lesssim$25 per cent for most of the SSPs covered here. Strictly speaking, this flux correction is only valid for the base models, which are of the same type as these newly synthesized NGSL-based SSP spectra. However, the difference in flux due to abundance variations is far smaller than our correction for the missing flux.

The same approach is used for calculating the missing flux in the *i* filter, but this time using our published models extension, MIUSCAT (Vazdekis et al. 2012). For the MIUSCAT models, we employ the Indo-US stellar library Valdes et al. (2004) to fill-in the gap left in between the MILES range (Paper I) and Ca II triplet range (Vazdekis et al. 2003). Since the effects of the α-enhancement on the continuum redwards of the *V* band is small (as shown by the flux ratios of Figs 10 and 11), the extension based on MIUSCAT is appropriate for this specific purpose.

6.2 Base models with varying isochrones

Fig. 18 shows the comparison between the broad-band colours based on Padova00 (magenta lines) and BaSTI (black lines) isochrones for the base models. Metal-poor models based on BaSTI tend to have bluer colours in all bands with respect to the Padova00 models, by up to 0.2 mag for the lowest metallicity considered here ($[M/H] = -1.26$). For solar and supersolar metallicities, a significant offset between the two sets of models is seen only in the $r-i$ colour, where the BaSTI models are bluer by ∼0.02 mag for old populations and by ∼0.04 mag for young populations. Overall, the agreement is good for the old stellar populations, whereas for younger ages, these colour differences reflect the differing prescriptions for AGB stars.

6.3 Scaled-solar versus α-enhanced SSP models

The comparison between base, scaled-solar and α-enhanced models is shown in Fig. 19 for the SDSS colours. No significant differences are observed between the base models and the scaled-solar ones, with the exception of the $u-g$ colour for the most metal-poor SSPs. Such difference must be attributed to the fact that at such low metallicity the MILES stars are α-enhanced. Conversely, α-enhancement has a remarkable impact on the resulting broad-band colours, having a differential effect on the different spectral ranges (see also Coelho et al. 2007). The α-enhanced models are bluer in the blue (by ∼0.2 mag in $u-g$ and ∼0.05 mag in $g-r$ for old populations) and redder in the red (by ∼0.02 mag in $r-i$) with respect to the base models, as one can also infer from the flux ratio of the two SSP spectra (Fig. 11). Note that the best agreement between the base and α-enhanced models is reached at low metallicities.

7 COMPARISON WITH OTHER MODELS

We compare the effect of varying [α/Fe] in our models with predictions from other synthetic stellar population models in the literature. We focus on some widely employed models that are based on empirical stellar spectral libraries, i.e. Conroy & van Dokkum (2012a, hereafter CvD12), Thomas, Maraston & Johansson (2011, hereafter TMJ11) and Schiavon (2007, hereafter S07). Note that while CvD12 provide full SEDs at varying abundance ratios, TMJ11 and S07 provide line strengths of Lick spectral features. We note however that whereas the predictions of TMJ11 are given at the nominal resolution of MILES, the models of S07 are provided in the Lick/IDS system (Worthey & Ottaviani 1997).

Fig. 20 compares the ratio of α-enhanced ($[\alpha/Fe] = +0.4$) to scaled-solar SSPs for our models and those of CvD12, at a fixed age of 13.5 Gyr, and for the same (Salpeter) IMF. The CvD12 models are computed at fixed [Fe/H]. Therefore, in order to perform a meaningful comparison, we have computed our α-enhanced SSP for a total metallicity of $[M/H] = +0.3$ (i.e. [Fe/H] ∼ 0.0, see equation 4), and taken its ratio with the scaled-solar model. Note also that both our models and the CvD12 models have the same spectral resolution (i.e. that of MILES) in the spectral range considered here (from ∼3500 to 7400 Å). The overall effect of increasing α-enhancement is similar in the CvD12 models and our models, reflected by the fact that the flux ratios in the figure have a similar large-scale behaviour, and similar 'absorption' and 'emission' residual features (e.g. for Mg and Fe lines, respectively). While the average flux ratio is about one for CvD12 models, it is less than one for our models. This occurs because we adopt α-enhanced isochrones for our α-enhanced model predictions, whereas CvD12 always use scaled-solar isochrones. Note however that the impact of the isochrones on the line indices is significantly less than the impact of the stellar spectra on the indices; see Fig. 9.

It is evident that the ratios of different features in the two curves in Fig. 20 are not precisely the same, indicating that the two sets of models differ to some extent in the relative effect of [α/Fe] on different spectral features. This is not surprising since the theoretical stellar spectra employed by CvD12 differ from those used in our models (see Section 2.3.2). In particular, CvD12 obtained their differential corrections using theoretical stars computed with the ATLAS12 code for model atmospheres and the SYNTHE spectrum synthesis package (Kurucz 1970, 1993; ported to LINUX by Sbordone et al. 2004) and line list provided by Kurucz. Another relevant difference is that our differential corrections are obtained from SSP spectra computed with theoretical stellar spectra (see Section 3.2), whereas the differential corrections of CvD12 were obtained from individual stars. Finally, as mentioned above, CvD12 employ scaled-solar isochrones for both their scaled-solar and α-enhanced predictions, whereas we employ α-enhanced isochrones for our α-enhanced model predictions. However, we note that the choice of isochrones has a small impact on the index predictions.

Some of the model differences seen in Fig. 20 are quantified in Fig. 21, where we compare the effect of [α/Fe] on the Mg and Fe lines for our models and also for those of S07, TMJ11 and CvD12.

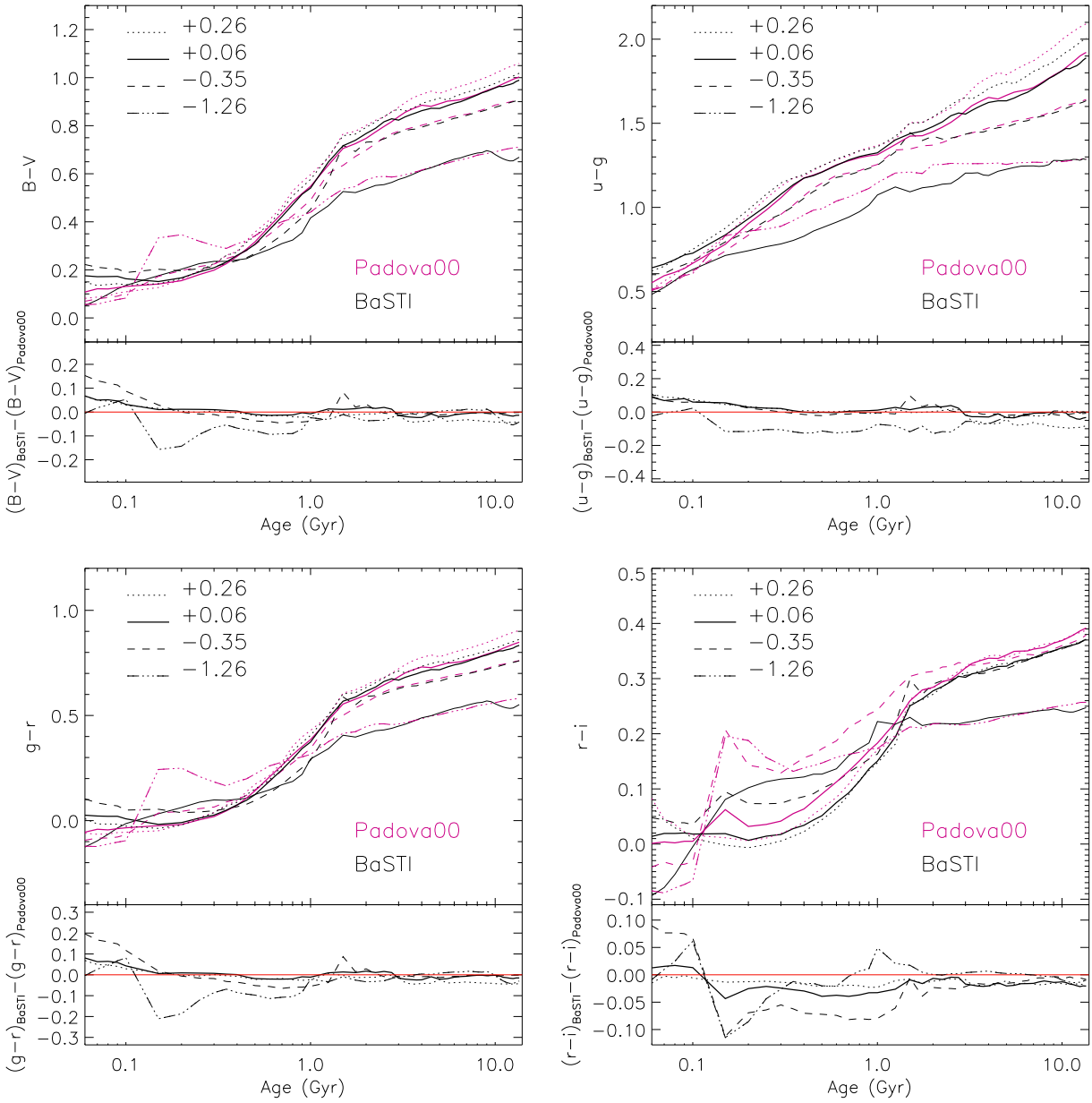

Figure 18. Dependence of broad-band colours on the isochrones adopted. Colours are displayed as a function of age for four different metallicities: $[M/H] = -1.26$ (dot–dashed line), -0.35 (dashed line), $+0.06$ (solid line) and $+0.26$ (dotted line). The magenta lines indicate the models computed with the Padova00 isochrones, whereas the black lines show the models based on BaSTI. The $B-V$ colour (upper-left panel) is computed in the Vega magnitude system, whereas the SDSS colours $u-g$ (upper-right), $g-r$ (lower-left) and $r-i$ (lower-right) are computed in the AB system. The residual colours are also shown in each panel. All the models have a Kroupa Universal IMF.

Similarly, Fig. 22 shows the behaviour of the line strengths of some representative Balmer lines (upper panels) and IMF-sensitive (lower panels) indices as a function of the total metallicity indicator [MgFe]′, for the different models. Each arrow in a given panel represents an individual model, with the black arrows connecting scaled-solar to $[\alpha/Fe] = +0.4$ SSP model line strengths, at fixed [Fe/H]. Since our models and those of TMJ11 are computed at fixed total metallicity, the comparison at fixed [Fe/H] is performed by increasing both $[M/H]$ and $[\alpha/Fe]$ in these models, using equation (4), with A = 0.75 and 0.94 (see Thomas et al. 2003a) for models and the TMJ11 models, respectively. Our models, the TMJ11 models, and the CvD12 models all have the same native (MILES) spectral resolution, while the S07 line strengths are given at the Lick/IDS resolution (see table 7 of S07).[11] For a given age, metallicity, and $[\alpha/Fe]$, we have determined the behaviour of the S07 line strengths at the MILES resolution, by smoothing our models to match the Lick/IDS resolution for each spectral feature, and then estimating the corresponding variation of its line strength at this resolution.

It is evident in Fig. 21 that the arrows corresponding to the various models do not have the same starting point in the index–index diagrams. These significant offsets among the predictions of the

[11] But note that the stellar library used in the S07 models is of higher resolution than the Lick/IDS (Jones 1999).

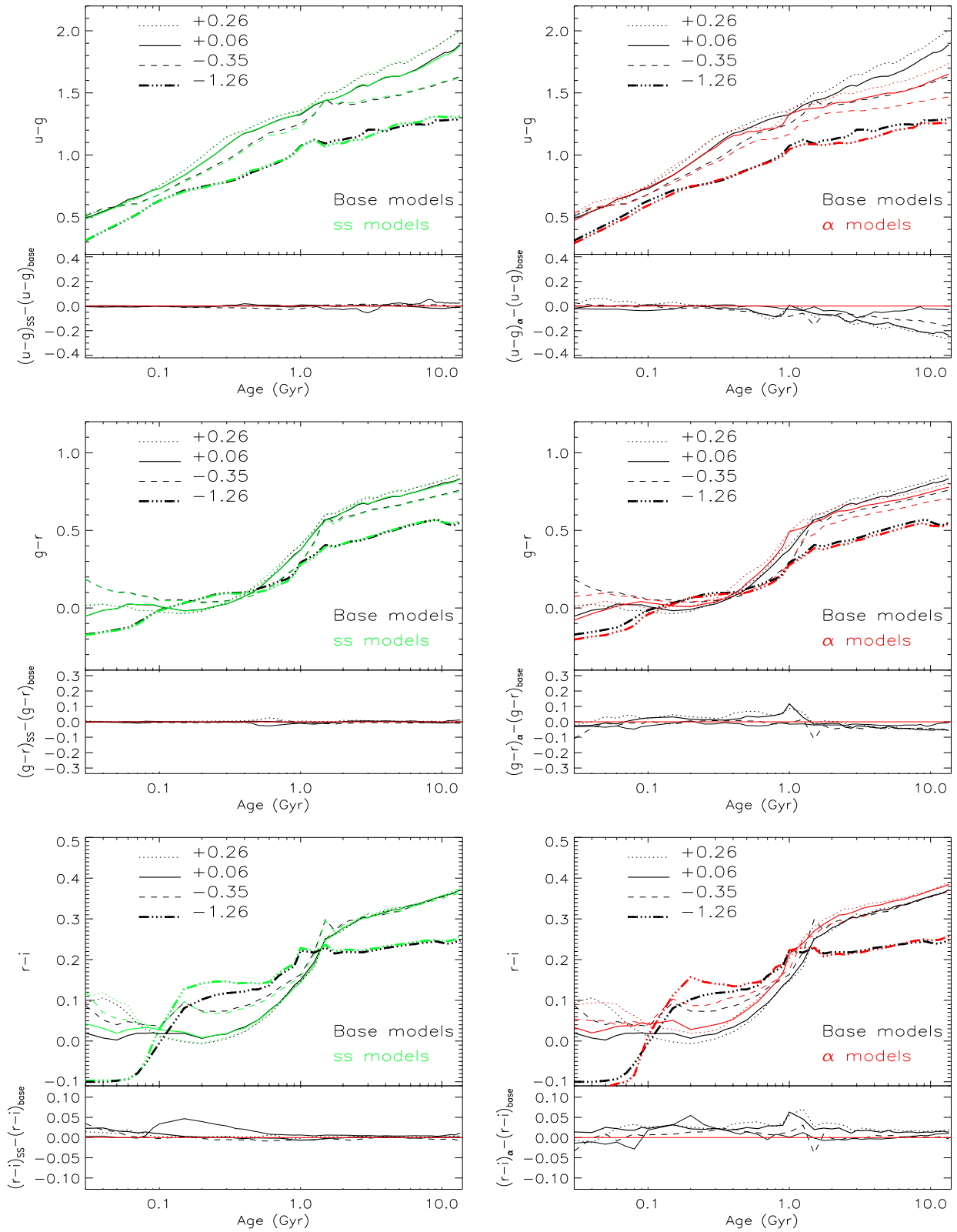

Figure 19. Left-hand panels: comparison between colours in the SDSS bands of scaled-solar models (green lines) and the base models (black lines). Right-hand panels: comparison between α-enhanced models (red lines) and base models (black lines). The colour variation is shown as a function of age for four different metallicities: $[M/\mathrm{H}] = -1.26$ (dot–dashed line), $[M/\mathrm{H}] = -0.35$ (dashed line), $[M/\mathrm{H}] = +0.06$ (solid line) and $[M/\mathrm{H}] = +0.26$ (dotted line). The residual colours are also shown in each panel.

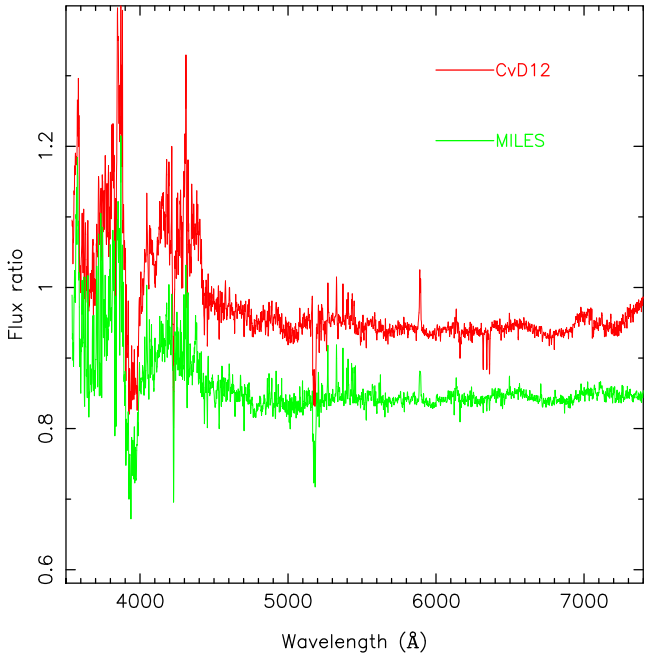

Figure 20. Ratio of α-enhanced to scaled-solar models, at fixed [Fe/H] = 0.0, for our models (green) and the Conroy & van Dokkum (2012a, red) SSP models with an age of 13.5 Gyr and a Salpeter IMF. The green curve has been arbitrarily shifted downwards by 0.1 in order to allow a better visual comparison with the red curve.

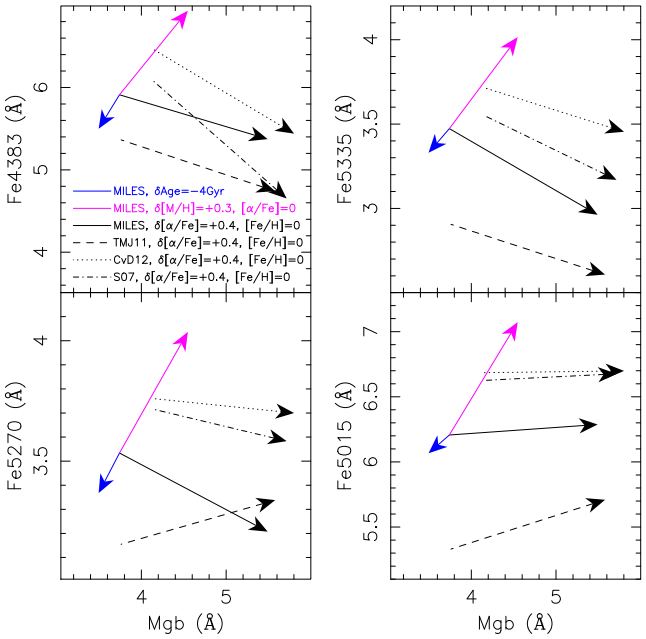

Figure 21. Line strengths for different Fe lines (Fe 4383, Fe 5270, Fe 5335 and Fe 5015; from top to bottom, and left to right) are plotted as a function of Mg*b* ($\lambda \sim 5177$ Å). Black arrows, plotted with different line types, show the effect of changing [α/Fe], at fixed [Fe/H] = 0.0, for SSP models with the same age of 13.5 Gyr and the same (Salpeter) IMF, from different authors, i.e. this work (solid), Thomas et al. (2011, dashed), Conroy & van Dokkum (2012a, dotted), and Schiavon (2007, dot–dashed), as labelled in the top-left panel. The blue and magenta arrows show, as reference, the effect of decreasing age by 4 Gyr and increasing total metallicity by +0.3 dex (for [α/Fe] = 0.0), respectively, in our SSP models.

various models at scaled-solar abundance are, however, expected. These offsets reflect different model ingredients (e.g. the isochrones) and different values for the solar metallicity (see Section 2) among other aspects of the model construction. For instance, our (Mg, Fe and Balmer lines) model predictions for an SSP with [M/H] = 0.0, age of 13.5 Gyr, and [α/Fe] = 0.0, would be matched by the CvD12 models with an ∼3.5 Gyr younger age, and slightly lower (∼0.05 dex) total metallicity. Such differences strongly suggest that relative ages are more robust than absolute ages in the models (e.g. Gibson et al. 1999; Vazdekis et al. 2001a; Schiavon et al. 2002, Mendel, Proctor & Forbes 2007). Note also that such differences decrease with decreasing age. However, a detailed discussion on the origin of these offsets between the models is beyond the scope of this paper. In the following, we focus on the relative responses of the various models to variations of the [α/Fe] abundance ratios (i.e. on the arrow directions, not their absolute values).

Fig. 21 shows that the Mg*b* index increases with [α/Fe], reflecting its strong sensitivity to [Mg/Fe]. The degree of increase is larger, by ∼0.2 Å, in our models and in those of TMJ11, relative to the S07 and CvD12 models. All the iron lines show a mild dependence on [α/Fe] at fixed [Fe/H], as these lines are believed to be mostly sensitive to Fe abundance (see e.g. S07, but also the discussion in Barbuy et al. 2003; Coelho et al. 2005 about the effect of electron donors such as Mg on the continuum). While this does seem to be the case, Fig. 22 shows that differences exist among model predictions. All models agree that Fe 5335 decreases with [α/Fe] (the amount of decrease being slightly stronger for our, relative to other, models). The behaviour of Fe 5270 is more model dependent, as this index remains constant with [α/Fe] for the CvD12 models, increases for TMJ11, and decreases in our models and in those of S07. The Fe 4383 decreases with [α/Fe] in all models, with a milder variation for our models and TMJ11, relative to the CvD12 and S07 models. Note that, because of a possible dependence on Mg abundance (Korn et al. 2005), the Fe 4383 index might not be as clean an Fe indicator as the Fe 5270 and Fe 5335 indices (see S07). Indeed, Fig. 21 indicates that this index does not behave differently than the other Fe lines. Finally, Fe 5015 is expected to have some sensitivity to the abundance of α-elements, in particular to [Mg/Fe] and [Ti/Fe] (Korn et al. 2005). However, no significant dependence of this index on [α/Fe] is seen in our models, CvD12, or the S07 models, while Fe 5015 actually increases with [α/Fe] in the TMJ11 models.

Fig. 22, which includes the results for a number of age- and IMF-sensitive indices, shows several interesting features:

Hβ line – TMJ11, S07 and our models point to little dependence of Hβ on [α/Fe] at fixed [Fe/H]. In contrast, the CvD12 models predict that Hβ increases significantly with α-enhancement. Although the origin of this discrepancy is unclear, one should notice that Hβ decreases with velocity dispersion in ETGs (see Section 8.2), and at fixed velocity dispersion, as seen in the stacked spectra of La Barbera et al. (2013). Hβ also mildly decreases with [Mg/Fe], by less than ∼0.1 dex[12] from [Mg/Fe] ∼ 0.1 to [Mg/Fe] ∼ 0.3. This seems to point to a genuine mild dependence of this index on enhancement, as predicted by S07, TMJ11 and our models. We return to this issue in Section 8.2.3.

Higher order Balmer lines – all the models agree in that Hδ_F should increase with [α/Fe], although the amount of increase is larger for

[12] We have estimated this amount of variation using the [Mg/Fe] stacked spectra of ETGs, for the two highest velocity dispersion bins, defined in La Barbera et al. (2013, see their fig. 7).

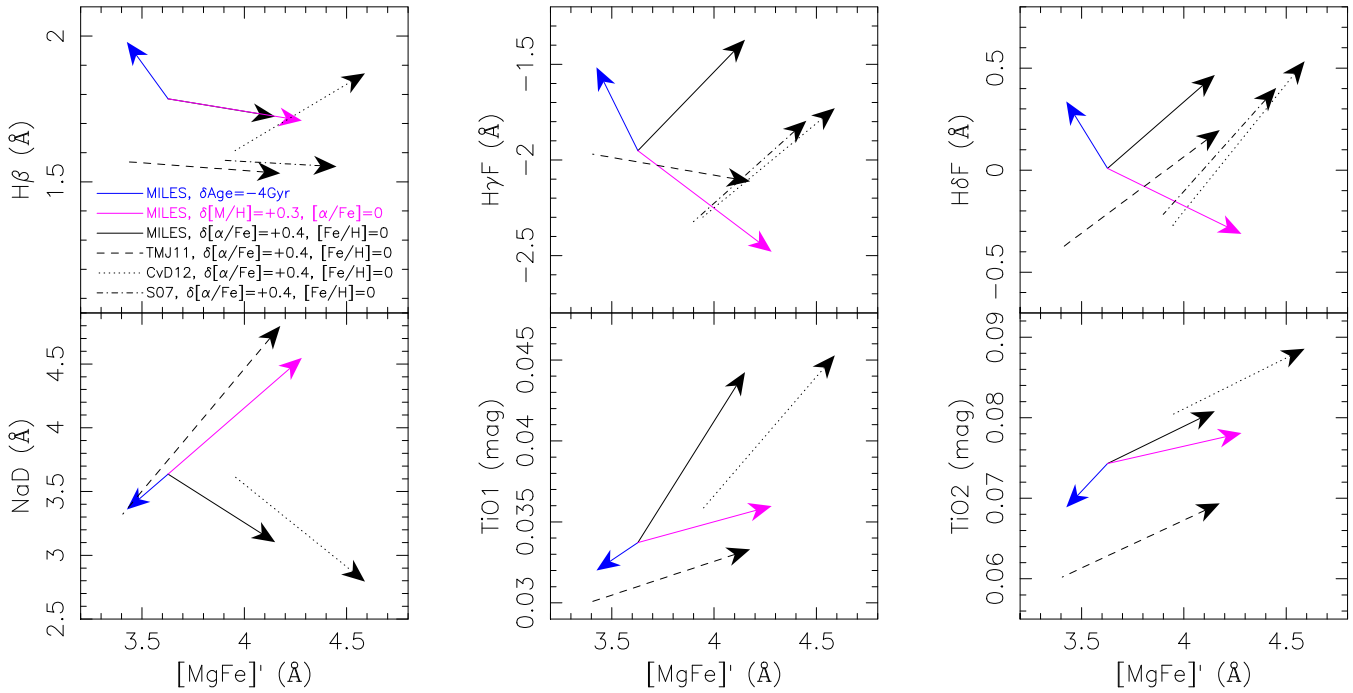

Figure 22. Same as Fig. 21 but plotting the line strengths of representative Balmer lines (top) and IMF-sensitive features (bottom) as a function of the total metallicity indicator [MgFe]′. Note that the IMF-sensitive line-strengths are not provided by the S07 models.

CvD12 and TMJ11 than for our models and S07. For Hγ_F, TMJ11 predict that this index should have little dependence on [α/Fe], while our, S07 and the CvD12 models predict an increase of Hγ_F with [α/Fe].

TiO IMF-sensitive features – we compare in Fig. 22 some representative IMF-sensitive features, i.e. NaD, TiO1, and TiO2, for which we can compare three different models (TMJ11, CvD12, and ours). A comparison between the CvD12 models and the base models from Vazdekis et al. (2012) for other IMF-sensitive features has recently been performed by Spiniello et al. (2014). The bottom panels in Fig. 22 show that all models agree on the prediction that TiO features should increase with [α/Fe]. This holds at either fixed [M/H] or fixed [Fe/H], as TiO bands are quite insensitive to total metallicity for old ages (see magenta arrows in the figure, showing the effect of varying [M/H] by +0.3 at fixed age). Also, both the CvD12 and our models agree that TiO2 should be less sensitive to [α/Fe], (when comparing the response to [α/Fe] with that to age, i.e. black and blue arrows in the figure) than TiO1, making it a better IMF indicator than TiO1. The reader should be warned, however, that neither TiO1 nor TiO2 show any significant variation with [Mg/Fe] in ETGs at fixed velocity dispersion (see La Barbera et al. 2013). Interestingly, although not plotted here, we find that the sensitivity of TiO2 to [α/Fe] is significantly smaller when a bottom-heavy IMF is adopted for computing the models. This is the case both for our models and also the CvD12 models.

NaD IMF-sensitive feature – this feature is found to decrease with [α/Fe] at fixed [Fe/H] in agreement with the CvD12 models. In our models, NaD also decreases with [α/Fe] at fixed total metallicity, while at high [α/Fe] the increase of NaD with [M/H] is milder than at scaled-solar (see top-left panel of Fig. 17). The net effect is that NaD decreases with [α/Fe], at either fixed [Fe/H] or [M/H]. It has been recently pointed out that an increase of total metallicity and [Na/Fe] (by +0.3 dex) might be able to explain the high NaD line strengths observed in massive ETGs (Jeong et al. 2013), with no need for a bottom-heavier IMF in these galaxies. As noted by Jeong et al. (2013), this result is based on the predictions from the TMJ11 models. Our new models support the prediction that NaD decreases with α-enhancement as in the CvD12 models. This suggests that it is necessary to invoke another source (e.g. IMF) in order to increase the model line strengths sufficiently to match the high NaD of massive ETGs. However, some caveats should be noted. For example, the NaD feature can be contaminated by interstellar absorption, although we note here that for low-velocity-dispersion ETGs with a Kroupa-like IMF (and selected to have low internal dust) our base model predictions for the NaD match exactly the observed strengths for this index (see La Barbera et al. 2013). In addition, we find that NaD increases, rather than decreases, with [Mg/Fe] at fixed velocity dispersion in massive ETGs. This is possibly due to a correlated variation of [Na/Fe] and [Mg/Fe] abundances in these systems (La Barbera et al. 2013).

In summary, Fig. 22 shows that although differences remain among predictions from different models on the dependence of the Balmer lines on [α/Fe], our new models agree well with the expectations from most models compared here, i.e. that Hβ remains constant (as in S07 and TMJ11), Hγ_F increases (as in CvD12 and S07), and Hδ_F increases (for all models) with [α/Fe]. Also, our models agree remarkably well with CvD12 models on the expected sensitivity of commonly used IMF-sensitive features (TiO1, TiO2, and NaD) to [α/Fe].

8 COMPARISON WITH GCs AND ETGs

8.1 Galactic globular clusters

In Fig. 23, we compare selected line-strength indices measured from our scaled-solar and α-enhanced model SEDs with those measured from the GGC libraries of Schiavon et al. (2005) and Kim et al. (in preparation). Both the model SEDs and GGC data have been

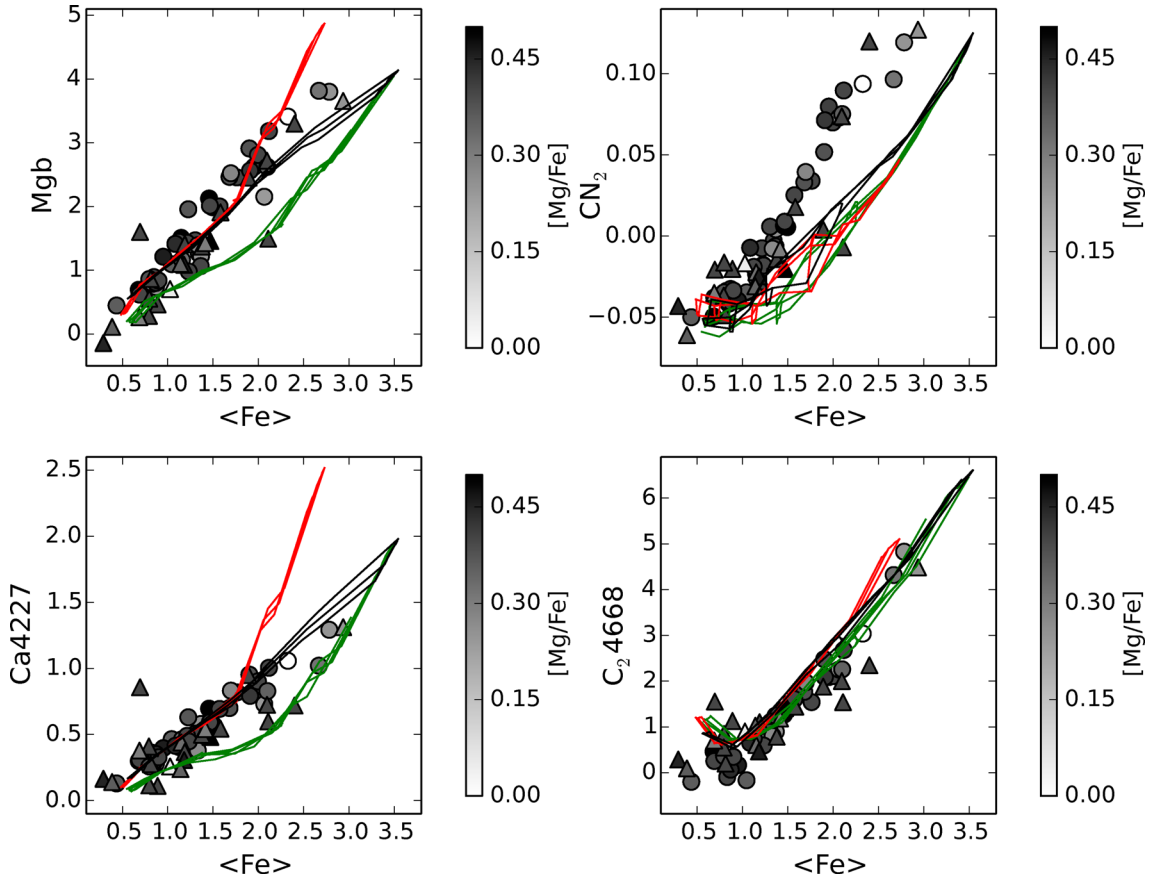

Figure 23. Comparison of selected line-strength indices measured from our scaled-solar (green), α-enhanced (red) and base (black) model SEDs with those measured from the GGC libraries of Schiavon et al. (2005) (circles) and Kim et al. (in preparation, triangles). Both the model SEDs and GC data have been smoothed to match a common LIS resolution of 5 Å (FWHM). Models with metallicities $-2.27 \leq [M/H] \leq +0.06$, ages $8 \leq t \leq 14$ Gyr and Kroupa Universal IMF are shown. Clusters are colour-coded by [Mg/Fe] taken from the compilation of Roediger et al. (2014) supplemented with data from Johnson et al. (2005, NGC 6205), Behr (2003, NGC 6341), Kacharov, Koch & McWilliam (2013, NGC 6864), Rodgers & Harding (1990, [Ca/Fe]: NGC 6981), Kraft et al. (1998, NGC 7006).

smoothed in order to achieve a common LIS resolution of 5 Å (FWHM).

The use of GGCs to test SSPs is particular useful; the majority of the GGCs in these two libraries have well-defined CMD-derived ages, and metallicities ([Fe/H]) and light element abundances such as [Mg/Fe], [C/Fe], [N/Fe] and [Ca/Fe] obtained from high-resolution spectroscopy (see e.g. Roediger et al. 2014 for a useful compilation of these quantities).

For all the indices shown in Fig. 23, at low metallicities ($[M/H] < -1.0$) the α-enhanced and base models are very similar. This is to be expected since the uncorrected MILES library stars for the base models in this regime are α-enhanced to a level similar to that of the α-enhanced models. Additionally, at the lowest metallicities the index predictions for the scaled-solar models also converge towards the base- and α-enhanced models. Such behaviour is not surprising as the sensitivity to the α-enhancement decreases with decreasing metallicity (see Fig. 11). This shows that the use of base models is also appropriate for studying metal-poor GGCs.

The typical [Mg/Fe] for GGC stars is $\sim$+0.4 (Roediger et al. 2014) and this is in good agreement with location of the majority of the GGCs in the Mg*b*–⟨Fe⟩ panel of Fig. 23. Most of the GGCs lie on the model [Mg/Fe] = +0.4 locus. A couple of the most metal-rich GGCs (e.g. NGC 6528 and NGC 6553) lie between the scaled-solar and α-enhanced grids suggesting [Mg/Fe] $\sim$ +0.2 to +0.3 which is consistent with the high-resolution [Mg/Fe] measurements of +0.25 ± 0.11 (Carretta et al. 2001; Coelho et al. 2001) and +0.32 ± 0.08 (Barbuy et al. 1992), respectively. Our result for these two clusters is also in good agreement with Lee et al. (2009b, see their fig. 13).

[Ca/Fe] is also enhanced in the majority of GGCs ($\sim$+0.3; Roediger et al. 2014) and this reflected in the location of GGCs in the Ca 4227–⟨Fe⟩ panel of Fig. 23. [Ca/Fe] in GGCs is typically $\sim$0.1 dex lower than [Mg/Fe] for a given cluster and this is well reproduced in the figure. The fact that [Mg/Fe] and [Ca/Fe] in GGCs behave similarly when compared to the α-enhanced grids is both reassuring and not surprising – both Mg and Ca are α-elements. However, as pointed out by Roediger et al. (2014), the lack of any correlation between [Mg/Fe] and [Ca/Fe] in GGCs seems to suggest that, while both are indeed α-elements, they are possibly produced in different nucleosynthetic sites. Interestingly, [Ca/Fe] does not seem to directly track [Mg/Fe] in massive galaxies (e.g. Vazdekis et al. 1997; Trager et al. 1998; Cenarro et al. 2003; Thomas et al. 2003a; Conroy 2013).

In terms of other indices, CN_2 (and CN_1 – not shown) is clearly stronger in the GGCs than the models, and the inclusion of α-enhanced SEDs does not improve the situation. It is well established that GGCs (e.g. Burstein et al. 1984; Cannon et al. 1998; Roediger et al. 2014) and extragalactic GCs (e.g. Burstein et al. 1984; Brodie & Huchra 1991; Kuntschner et al. 2002; Strader et al. 2003; Beasley et al. 2004; Cenarro et al. 2007a; Schiavon et al. 2013)

show enhanced CN when compared to solar neighbourhood stars. Fig. 23 provides support for the early results of Lee & Worthey (2005, see also Burstein et al. 1984), which found a significant discrepancy when comparing Ca4227, CN_1, CN_2 and NaD index strength from their α-enhanced SSP models and data for GCs in the Milky Way and in M 31. This shortcoming of the current generation of α-enhanced SSP models can be understood when taking properly into account the phenomenon of multiple populations (MPs) in GGCs (see Gratton, Carretta & Bragaglia 2012; Piotto et al. 2012; Cassisi & Salaris 2013, and references therein for detailed reviews on this topic).

Essentially, the MP phenomenon is related to the presence in each individual GC of two (almost coeval) stellar generations, the first one born with a canonical α-enhanced heavy element distribution, the second generation characterized by anticorrelated CN–ONa abundance patterns, and by moderate (and – only – in a few cases very large) He enhancement. Due to the impact on the SED of molecular bands associated with both C and N (see the detailed discussion made by Sbordone et al. 2011 and Cassisi et al. 2013), one might anticipate that the light-element (anti) correlations characteristic of the second generation stars in GGCs will affect the strength of specific indices such as CN_1 and CN_2. This issue has been explored by Coelho, Percival & Salaris (2011) given certain assumptions[13] about the chemical abundance patterns of second generation stars. These authors found that – regardless of the exact value of the He enhancement – as a consequence of the stronger CN and NH molecular bands in the spectra of second generation stars CN indices are significantly affected. Variations of the order of ∼0.08 mag were seen between the CN indices predicted for a pure first-generation stellar population and those predicted for population of pure second-generation stars (with extreme values for the light-element anticorrelations).

Finally, unlike CN indices, the $C_2$4668 index of the GGCs is in good agreement with the model grids. As evidenced by the superposition of the scaled-solar, α-enhanced and base models, it is clear that this index has little sensitivity to the α-abundance.

In summary, we conclude that the LIS Mg*b* and iron indices of the GGCs are well reproduced by the α-enhanced MILES models. Good agreement is also found for Ca 4227 in GGCs. The model CN indices are largely insensitive to the α-abundance, and fail to reproduce the high CN values seen for GGCs at a given metallicity. The model C_2 4668 index is also insensitive to the α-abundance, but unlike CN reproduces the behaviour of the GGC C_2 4668 measurements.

8.2 Early-type galaxies

8.2.1 ETG colours

A strong constraint on the reliability of our models comes from the optical colours of nearby ETGs. Current stellar population models, both based on theoretical stellar spectra and empirical libraries, still have difficulties in reproducing the optical colour distribution of ETGs, with theoretical models showing the strongest discrepancies (Maraston et al. 2009; Conroy & Gunn 2010; Ricciardelli et al. 2012).

[13] They adopted extreme – although still realistic – light-element chemical patterns in order to maximize the possible expected impact of these chemical peculiarities on SSP modes.

In Fig. 24, we present the colour distribution in the SDSS bands of a sample of z∼0.04 ETGs, as selected in Ricciardelli et al. (2012). These data are compared with our scaled-solar and α-enhanced SSP models for a range of metallicities and ages assuming a Kroupa Universal IMF. The scaled-solar models (upper panels) have the same difficulties as highlighted in Ricciardelli et al. (2012) for the base models. This behaviour is expected since the scaled-solar models are very similar to the base models in the high-metallicity regime required to fit luminous ETGs (see Fig. 19), a region where the MILES stars have approximately scaled-solar abundance ratios (see Fig. 3). The colours for the scaled-solar models are too red in $g-r$ and too blue in $u-g$ and $r-i$. This is a problem that cannot be solved by superimposing a young stellar population on top of the main population, since this would shift the whole set of colours to the blue and thereby worsen the mismatch with the $u-g$ and $r-i$ colours.

As shown in Section 6.3, the α-enhanced models are bluer in the blue bands, and redder in the red, as seems to be required by the data. Indeed, the comparison with the α-enhanced models (lower panels of Fig. 24) show a much better agreement with data in the $g-r/r-i$ plane. However, the shift to the blue in $u-g$ appears too dramatic to reconcile the model with these data, suggesting that an α-enhancement of $[\alpha/\mathrm{Fe}] = +0.4$ (as in the models presented here) is too high when compared to the observed colours of ETGs. However, the best solutions obtained with these models are more consistent than those obtained with the scaled-solar models. It is also worth recalling here that our models with varying abundance ratio do not extend to the blue end of the u filter response, where we used our NGSL-based base model predictions. The α-enhanced models point to old ages in the colour–colour diagrams, whereas the scaled-solar models require significantly younger ages for the $u-g$ versus $g-r$ diagram.

To explore the effect of more complex SFHs, we perform a set of Monte Carlo (MC) simulations, where we allow all the stellar population parameters to vary: age, metallicity and IMF slope (using the bimodal parametrization). We adopt three-burst SFHs, where the mass fraction involved in each burst is also a free parameter. The resulting predictions for 10 000 MC simulations are shown in Fig. 25 for scaled-solar models (upper panels), for α-enhanced models (middle panels) and for a random combination of the two (lower panels). The mixture of scaled-solar and α-enhanced models gives better results as the solutions obtained for the two colour–colour diagrams are more consistent each other. The improvement in the $u-g/g-r$ plane with respect to the case where only SSPs are used, is mainly due to the contribution of young stars and metal-poor populations. Nevertheless, the models have difficulties in reproducing the part of the diagram lying at high $u-g$. The match in the $r-i/g-r$ plane also improves significantly. Indeed, we see a clear reddening of $r-i$, that is due to both the use of α-enhanced models and to varying the IMF slope (see section 6.1 in Ricciardelli et al. 2012). The obtained solutions are consistent with recent studies based on absorption line strengths, which find steeper IMF slopes $[\alpha/\mathrm{Fe}]$ values around ∼0.2 and old ages for massive ETGs (e.g. Conroy & van Dokkum 2012b; La Barbera et al. 2013; Spiniello et al. 2014).

8.2.2 Full spectrum fitting

The solar-scaled and α-enhanced model SEDs can be used in full spectral-fitting techniques that can, in principle, improve the overall fits to data and be used to derive (in particular) the [Mg/Fe]

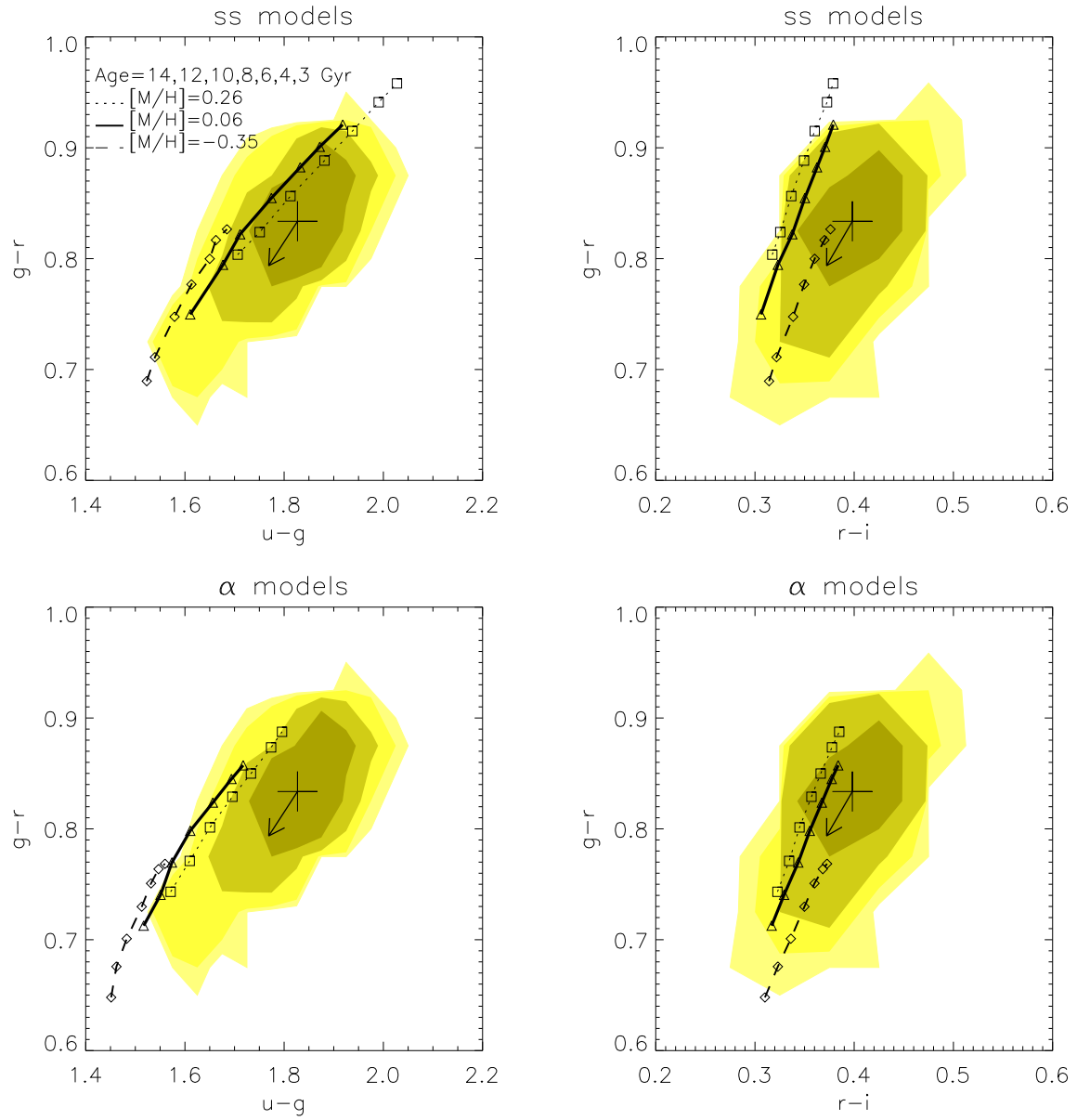

Figure 24. Observed colour distribution in the SDSS bands of a sample of ETGs at $z \simeq 0.04$. The contours enclose 20, 40, 60 and 95 per cent of the galaxies. The cross indicates the location of the median colours. The synthetic colours derived from scaled-solar models (upper panels) and α-enhanced models for a Kroupa Universal IMF are overplotted. Only SSP models with ages in the range 3–13.5 Gyr and metallicities: −0.35, +0.06, +0.26 have been considered.

overabundance observed in massive galaxies. We have attempted to follow this approach by using the penalized pixel-fitting stellar kinematics extraction (pPXF) routine developed by Cappellari & Emsellem (2004). We carried out this exercise on data for Virgo galaxies published in Yamada et al. (2006). We perform our spectral fits on two ETGs, one relatively low-mass (NGC 4489), and the other a giant elliptical (NGC 4365) which have scaled-solar and [Mg/Fe]-enhanced abundances, respectively.

At first, we tried to perform spectral fits over large wavelength ranges (e.g. more than 1000 Å), but we were unable to reproduce the [Mg/Fe] values and trends within galaxies reported by Yamada et al. (2006). This is not surprising given the fact that the information contained in relevant Mg- and Fe-sensitive features gets diluted with increasing wavelength range (e.g. Walcher et al. 2009). We therefore turned to fit only those regions where we expected the effect to be most noticeable (i.e. the Mg*b*–Fe 5335 range; see for example Figs 10 and 11). We therefore performed the fit within the range λλ 4800–5500 Å. The results of this exercise are shown in Figs 26 and 27. Each figure shows our attempts to fit the observed spectrum using (i) scaled-solar models only, (ii) α-enhanced models only and (iii) a combination of the two using the same age and metallicity for the two populations. In Fig. 26 we see that, for NGC 4489 – a low velocity dispersion galaxy – pure scaled-solar and the mixed models reproduce the spectrum fairly well, although pPXF has some preference for the true scaled-solar models. Fits with α-enhanced models only cannot match all the observed absorption features. The case of the massive galaxy NGC 4365 ($\sigma = 245$ km s^{-1}) is different (see Fig. 27). Here, α-enhanced models are preferred over the scaled-solar models. It is important to note that the higher velocity dispersion of this galaxy makes it harder to identify any mismatches with the templates, as can been seen in the residual spectra.

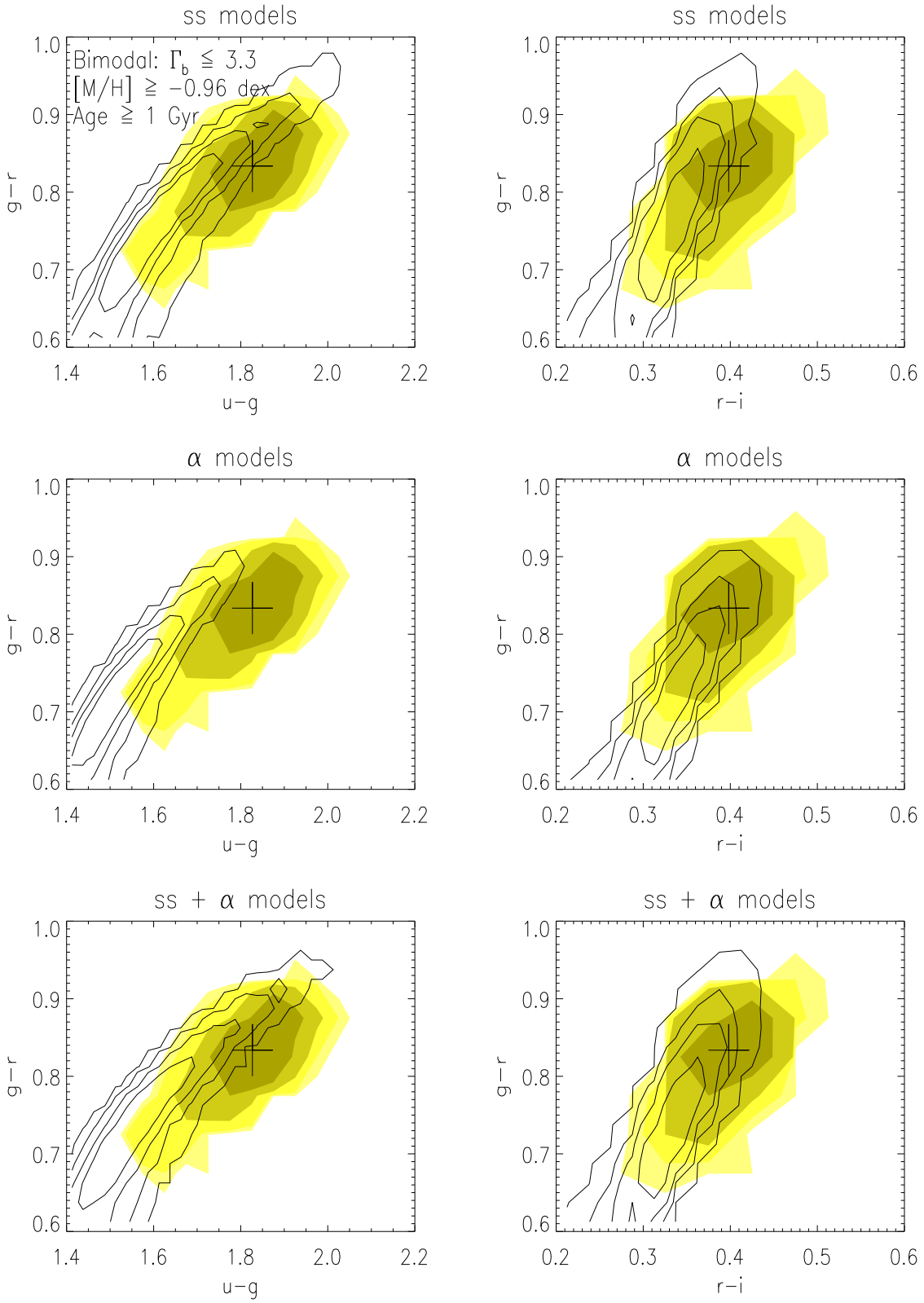

Figure 25. The same ETG colour distributions of Fig. 24 are compared with the predictions from composite stellar population models. The black contours enclose 20, 40, 60 and 95 per cent of the MC simulations of multiple bursts models, where age, metallicity, IMF (bimodal) slope and strength of the bursts are allowed to vary. The upper panels show the predictions for the scaled-solar model, the middle panels display those of α-enhanced models, whereas the bottom panels show the predictions from MC simulations where a random combination of the two set of models is considered.

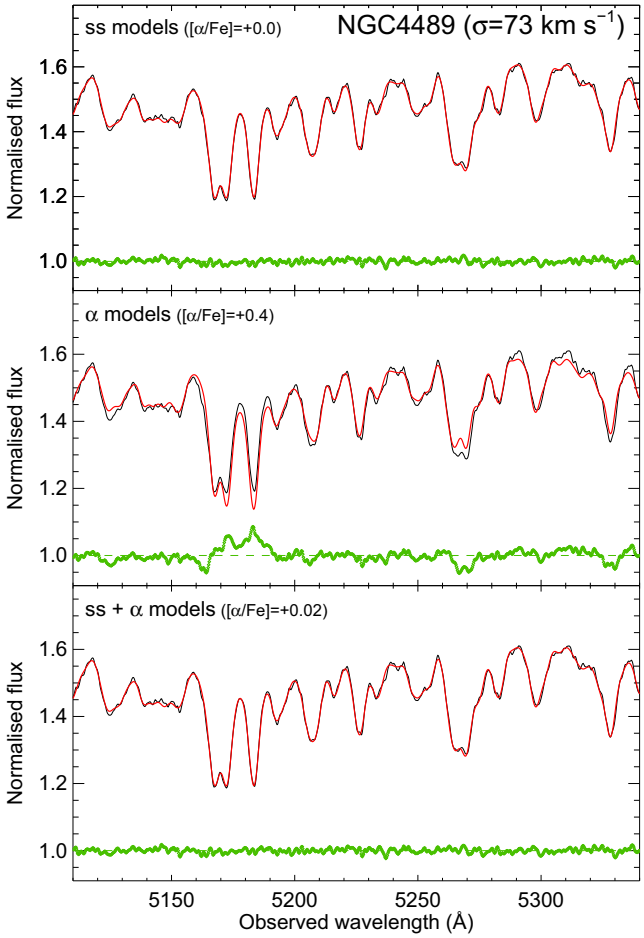

Figure 26. Spectral fitting of the low-velocity-dispersion galaxy NGC 4489. The upper panel shows the fit obtained with scaled-solar models. The middle panel shows the fit obtained with the α-enhanced models with [Mg/Fe] $= +0.4$. The bottom panel shows the fit with both set of models included in the data base. The residuals are shown (in green), keeping the same scale.

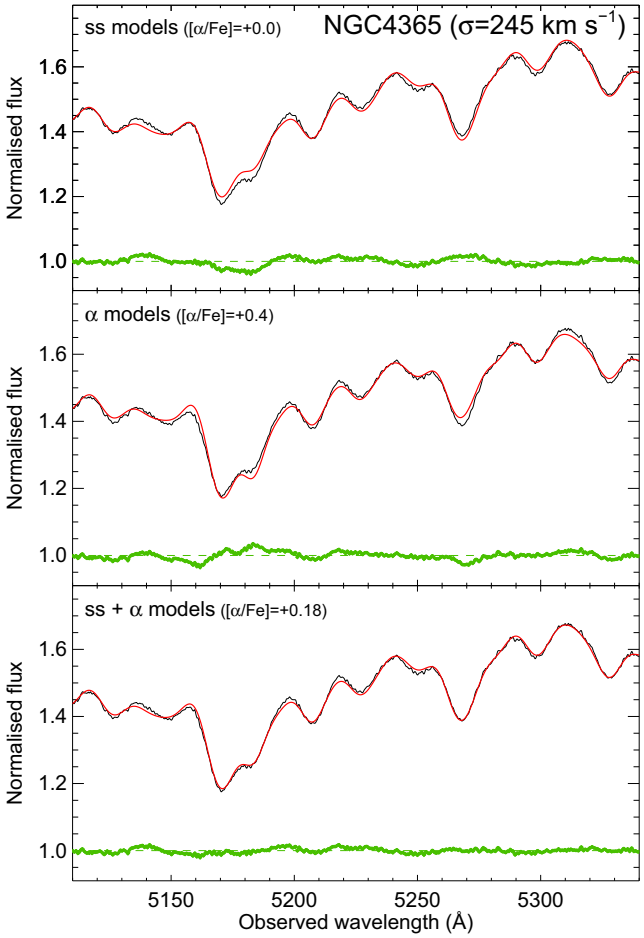

Figure 27. Spectral fitting of the giant elliptical galaxy NGC 4365. See Fig. 26 for the details on the panels.

The overall conclusion from this exercise is that our models together with full-spectral fitting can be used to estimate the [Mg/Fe] enhancement. However, the spectral fits are sensitive to the wavelength range employed to estimate the α-enhancement. Short-wavelength regions around the main spectral features (e.g. Mg*b*, Fe 5270) are preferred over long baselines (see also the discussion in Walcher et al. 2009; Cezario et al. 2013 on the dependence of spectral fitting results with the wavelength range).

8.2.3 Line indices

Fig. 28 shows three classical index–index diagrams with the predictions of the three models, base, scaled-solar and α-enhanced. Overplotted are the index measurements in the LIS-8.4 Å system for the ETG sample of Sánchez-Blázquez et al. (2006b). The model grids obtained when plotting Hβ_o against Mg*b*, ⟨Fe⟩ and [MgFe] indices, which are sensitive to Mg, Fe and total metallicity, respectively, provide similar age/metallicity solutions for the most massive galaxies, i.e. those galaxies with the largest abundance ratios and largest [MgFe] index values.

We see that most of the massive galaxies fall below the horizontal line corresponding to the oldest stellar population (14 Gyr) of the scaled-solar model grids. The same applies to the base model grids, which at high metallicities have an approximately scaled-solar [Mg/Fe] abundance ratio. However, the locus of these galaxies falls in between the lines corresponding to the oldest SSPs of the scaled-solar and the α-enhanced models, consistent with old ages, total metallicity above solar and an abundance ratio around [Mg/Fe] $\sim +0.2$. Note that we only employed models with a Kroupa Universal IMF for the grids of Fig. 28 as our present purpose is not fit these galaxies, but rather to illustrate the advantages of the new models presented here. We could have obtained slightly younger ages for the most massive ETGs had we employed grids with steeper IMF slopes, according to the relation between the slope and the velocity dispersion according to Ferreras et al. (2013), La Barbera et al. (2013) and Spiniello et al. (2014); see also the results we show and discuss shortly in Fig. 29.

It also is worth noting in Fig. 28 (top panel) that the scaled-solar line that corresponds to solar metallicity, i.e. the third vertical line starting from the right, is very similar to that corresponding to the base model. Similar behaviour is seen for the more metal-rich lines with $[M/H] = +0.15$ and $+0.26$, although in these cases the lines corresponding to the base models are slightly shifted towards the solar metallicity value with respect to the scaled-solar models. We attribute this small difference to the fact that many of the MILES stars have [Mg/Fe] values slightly below scaled-solar at these high metallicities (Milone et al. 2011). For lower metallicities, the vertical lines corresponding to the base models are shifted towards a

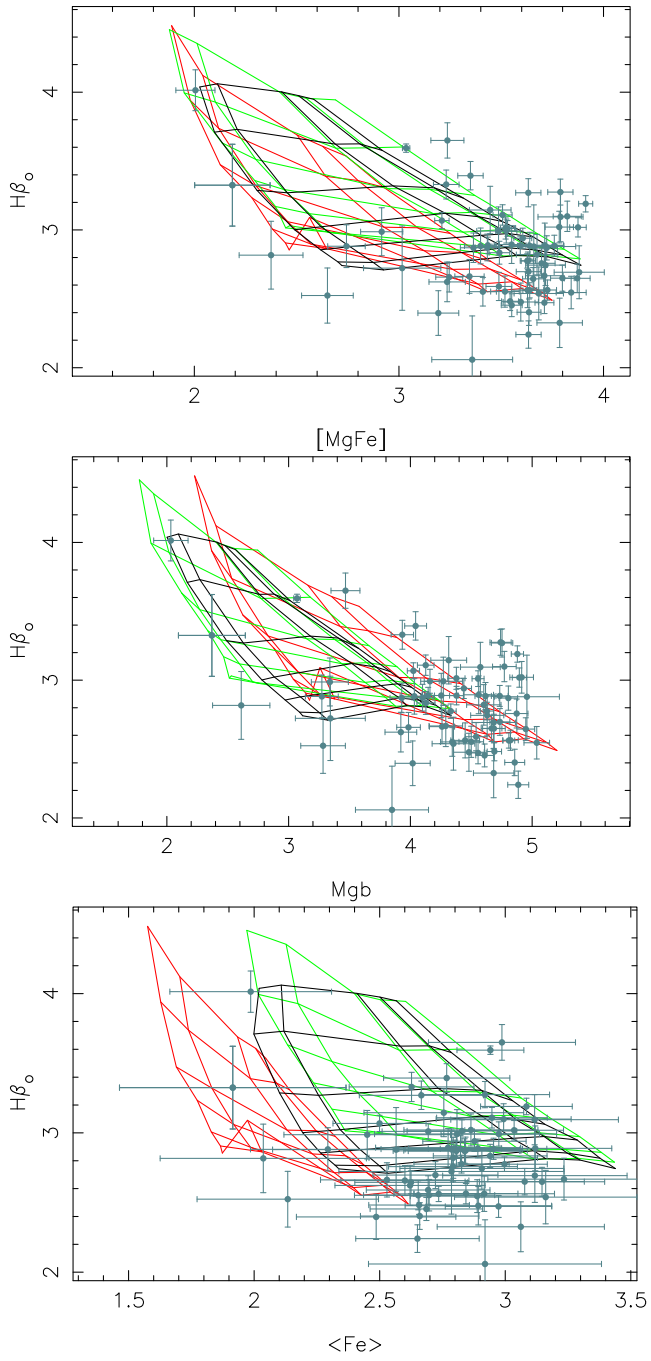

Figure 28. Various Mg and Fe index–index diagrams for three different model sets; the base models (black), the scaled-solar models (green) and the α-enhanced models (red), with [Mg/Fe] = +0.4. Overplotted are the line-strength indices measured in the sample of Sánchez-Blázquez et al. (2006b). The metallicity increases from left to right $[M/H] = -0.35, -0.25, +0.06, +0.15, +0.26$, whereas the age increases from top to bottom 2.0, 2.75, 5.0, 7.5, 10.0, 12.5, 14.0 Gyr. All the models have a Kroupa Universal IMF and have been smoothed to match the LIS-8.4 Å.

higher metallicity with respect to the two, the scaled-solar and the α-enhanced model lines (top panel, Fig. 28). Note that for the base models the stars are selected according to their [Fe/H] values. However, at these metallicities, the MILES stars are overenhanced in the [Mg/Fe] abundance. Therefore, the stars have a total metallicity

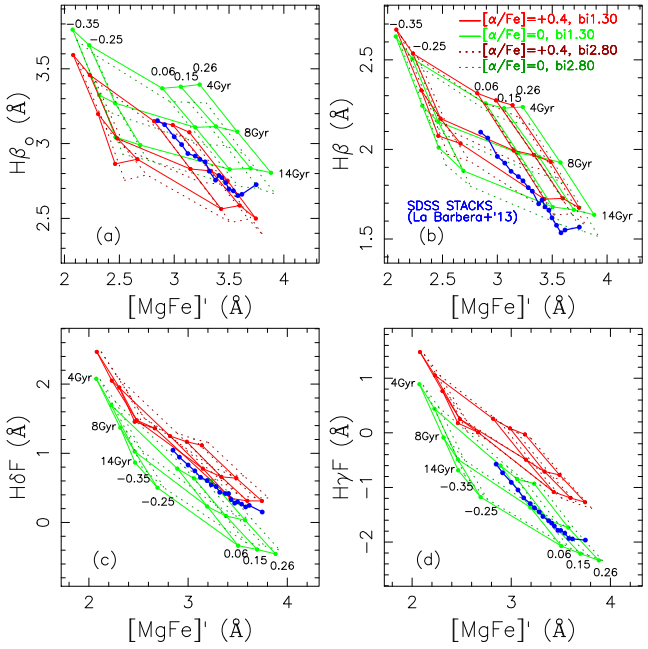

Figure 29. Line strengths of Balmer lines, Hβ, Hβ_o, Hδ_F, and Hγ_F are plotted as a function of the total metallicity indicator [MgFe]′, for scaled-solar (green) and α-enhanced SSP models (red). Light-solid and dark-dotted grids correspond to models with standard (bimodal; $\Gamma_b = 1.3$) and bottom-heavy (bimodal; $\Gamma_b = 2.8$) IMF, respectively. The grids show the effect of changing total metallicity (moving from left to right in each panel) and age (increasing from top to bottom in each panel), respectively, as labelled. Blue dots, connected by a blue line, mark the line strengths for 18 SDSS stacked spectra of ETGs, from La Barbera et al. (2013), in the range of galaxy velocity dispersion from ∼100 to ∼300 km s^{-1}. Line strengths have been corrected for all models and spectra to the same σ of 200 km s^{-1} (i.e. the same resolution employed in La Barbera et al. 2013), summed up in quadrature to the SDSS spectral resolution.

that is higher than that of the stars employed in the scaled-solar and α-enhanced models according to equation (4).

Fig. 29 is similar to Fig. 28 but shows representative Balmer lines, Hβ_o, Hβ, H$\delta_F$and Hγ_F (panels a–d), as a function of the total metallicity indicator [MgFe]′. The grids with dotted line type in the figure show models with a bottom-heavy, rather than Kroupa-like, IMF. Green and red grids correspond to scaled-solar and α-enhanced models, respectively. In each panel, we overplot data points for 18 stacked spectra of ETGs from La Barbera et al. (2013), ranging from a galaxy velocity dispersion of ∼100 to ∼300 km s^{-1}. Both model and data line-strengths are plotted at the same spectral resolution of 200 km s^{-1}, added in quadrature to the native resolution of the SDSS spectrograph (∼2.8 Å at $\lambda \sim 5000$ Å). The comparison of models and data can be summarized as follows.

(i). The model Hβ and Hβ_o indices behave differently with α-enhancement, in that the former is nearly independent of [α/Fe], while Hβ_o decreases with α-enhancement. As a result, one can explain the observed Hβ_o of our stacked spectra of ETGs with α-enhanced models, while for Hβ a bottom-heavy IMF (see dotted grids in panel b of the figure) seems to be required to account for the observed line strengths. However, as noted above (Section 7), the behaviour of Hβ with [α/Fe] is also quite model dependent, as the CvD12 models predict that this index will increase, rather than remain constant, with [α/Fe]. Also, as reported in Cervantes & Vazdekis (2009), different theoretical stellar libraries lead to different predictions for the response of Hβ and Hβ_o to [α/Fe].

Indeed, using Munari et al. (2005), rather than Coelho et al. (2005) stellar models, one would predict the opposite [α/Fe] dependence of Hβ and Hβ_o than that seen in Fig. 29 (see section 4 of Cervantes & Vazdekis 2009). These differences originate, at least in part, in the residual seen towards the red end of the feature bandpass of the Hβ and Hβ_o index definitions, as illustrated in the flux ratio of Fig. 16. This residual corresponds to a metallic contamination within the red wing of the Hβ feature, which includes Fe-peak elements such as chromium (see also Section 5.3). The discrepancies between the predictions for the Hβ and Hβ_o lines based on the Munari et al. (2005) and Coelho et al. (2005) stellar spectra likely stem from differences in the adopted line lists employed for the computation of these two sets of model spectra, and are presently being investigated (Sansom & Coelho, in preparation).

(ii) The position of the stacked spectra with respect to scaled-solar model grids is approximately the same in both the Hβ versus [MgFe]′and Hβ_o versus [MgFe]′ diagrams. This, together with the fact that both Hβ and Hβ_o exhibit a similar variation with [α/Fe] at fixed velocity dispersion in the stacked spectra of ETGs (see Section 7), suggests that both Hβ and Hβ_o have more similar dependences on [α/Fe] than suggested by the models.

(iii) The Hδ_F index behaves consistently with Hβ_o in the sense that both indices, in the stacked spectra of ETGs, could be explained by a metal-rich, old and significantly α-enhanced ([α/Fe] $\sim +0.3$ dex) SSP.

(iv) In contrast, the behaviour of Hγ_F with [α/Fe] seems to be too extreme in the models. The observed Hγ_F of the stacked spectra would require [α/Fe]$\sim$0.2 dex for an old ($\sim$14 Gyr) and metal-rich ([M/H] $\sim +0.3$) SSP, in contrast to the higher [α/Fe] implied by Hβ_o and Hδ_F. The position of the stacked spectra with respect to the scaled-solar Hγ_F grid suggests that the 'true' dependence of Hγ_F on [α/Fe] should indeed be mild. Note however that the blue pseudo-continuum of the Hγ_F line is located on a strong CH absorption, i.e. the *G* band at $\sim$4300 Å. Therefore, non-solar carbon (and nitrogen) abundance ratios reported in massive galaxies (e.g. Conroy et al. 2014; Worthey, Baitian & Serven 2014), which might depend on environment (Sánchez-Blázquez et al. 2003; Carretero et al. 2004; Carretero, Vazdekis & Beckman 2007), may have a noticeable effect on measured Hγ_F index strength.

In summary, Fig. 29 points to the well-known issue that SSP model predictions for different Balmer lines (and indeed also different definitions of the same line, e.g. Hβ and Hβ_o) provide different estimates of the age of the old stellar populations of ETGs (see also Schiavon et al. 2004 for an alternative view, who argues that the disagreement between high-order Balmer lines might be related to the presence of young stellar populations.) The figure shows that neither the α-enhanced models nor models with a varying IMF seem able to solve this issue. Some clues come from the comparison of the [α/Fe] dependence of Balmer lines among different models (see Fig. 22) and the observed line strengths of ETGs, as reported above. However, these clues should be only interpreted in a qualitative manner and a more quantitative comparison of models and data is desirable. In fact, the discrepancies between data and models in Fig. 29 might occur due to different effects, such as a variation of abundances ratios of specific chemical species in the stellar atmospheres, and/or more complex SFHs than pure SSPs. Also, the observed differences in the predictions from the various models suggest differences in the theoretical stellar spectra that are employed to obtain the differential corrections, which might come in part from the adopted line lists.

8.2.4 The proxy for [Mg/Fe]

As discussed above (Section 8.2.2), our new α-enhanced models can be used to estimate the [Mg/Fe] of ETGs through spectral fitting, provided one defines carefully the spectral range to fit. In this section, we discuss alternative methods to estimate [Mg/Fe], by either comparing the line strengths of selected (Mg and Fe) spectral features to predictions of either α-enhanced (as in e.g. TMJ11) or base models (see La Barbera et al. 2013). To this end, we rely on a subsample of 4671 nearby ($z \sim 0.07$) ETGs from the SDSS-based Spheroids Panchromatic Investigation in Different Environmental Regions (SPIDER) sample, restricting the analysis to the best-quality spectra, with S/N > 25 per Å in the spectral regions of the Mg*b*, Fe 5270 and Fe 5335 features (see La Barbera et al. 2013 and references therein). For each spectrum, we obtain different estimates of [Mg/Fe] as follows:

'True' – we fit [MgFe]′, Mg*b* and Fe3[14] line strengths with either TMJ11 or our α-enhanced models, fixing the age of the SSP models in the fit to the luminosity-weighted age measured with the software STARLIGHT for each galaxy (see La Barbera et al. 2013 for details).

Proxy for – at fixed (STARLIGHT) age, we estimate the metallicity by fitting alternately the Mg*b* and Fe3 line strengths using either the base or the scaled-solar models, without the differential correction for the alpha-enhancement effect (i.e. $[M/H]_{Mgb}$ and $[M/H]_{Fe3}$). The difference of the two metallicity estimates, $[Z_{Mg}/Z_{Fe}] = [M/H]_{Mgb} - [M/H]_{Fe3}$, is the proxy for [Mg/Fe].[15] The computation is repeated for three sets of reference models, i.e. our scaled-solar, base models and base models constructed with the Padova00 isochrones. We refer to these three proxies as $[Z_{Mg}/Z_{Fe}]_{SS(BaSTI)}$, $[Z_{Mg}/Z_{Fe}]_{Base(BaSTI)}$ and $[Z_{Mg}/Z_{Fe}]_{Base(Padova00)}$, respectively.

As discussed in La Barbera et al. (2013), since for an α-enhanced population one has $[M/H]_{Mgb} > [M/H]_{Fe3}$, estimating the proxy may require some extrapolation of the reference models above the highest available [M/H] in the models. This may hamper the estimate of the proxy for extremely high [α/Fe]. On the other hand, as shown in fig. 6 of La Barbera et al. (2013), the $[Z_{Mg}/Z_{Fe}]_{Base(Padova00)}$ proxy correlates remarkably well with the [α/Fe] estimated from models (TMJ11) that take [α/Fe] explicitly into account. This suggests that for several applications one does not need to use α-enhanced models to estimate the [Mg/Fe], provided that a suitable calibration of the proxy into the 'true' [α/Fe] is performed. To this effect, Fig. 30 expands on fig. 6 of La Barbera et al. (2013), comparing the [α/Fe] estimate from our new models with the three proxies $[Z_{Mg}/Z_{Fe}]_{SS(BaSTI)}$, $[Z_{Mg}/Z_{Fe}]_{Base(BaSTI)}$and $[Z_{Mg}/Z_{Fe}]_{Base(Padova00)}$ (panels a-c, respectively), and comparing it to the [α/Fe] from the TMJ11 models ($[\alpha/Fe]_{TMJ11}$; panel d). Solid lines in the figure show best-fitting lines to the data, while dashed lines mark the $\pm 1\sigma$ scatter around median trends. The figure confirms the remarkable correlation of the true [α/Fe] with the proxies. However, differences do exist among different proxy estimates, in that (i) the slope and zero-point of the best-fitting line are slightly different from one proxy to another, the former ranging from $\sim$0.56 to $\sim$0.62,[16]

[14] Fe3 = $\frac{1}{3}$(Fe4383 + Fe5270 + Fe5335); Kuntschner (2000).

[15] Note that we keep for the proxy the same notation we employed in our previous works (e.g. Yamada et al. 2006; La Barbera et al. 2013).

[16] Note that in fig. 6 of La Barbera et al. (2013) we reported a gradient of $\sim$0.55, which is different from the values in Fig. 30. In that paper, we compared the proxy to the TMJ11 [α/Fe] estimates, and did not apply the same S/N cut to select ETGs, as in this work.

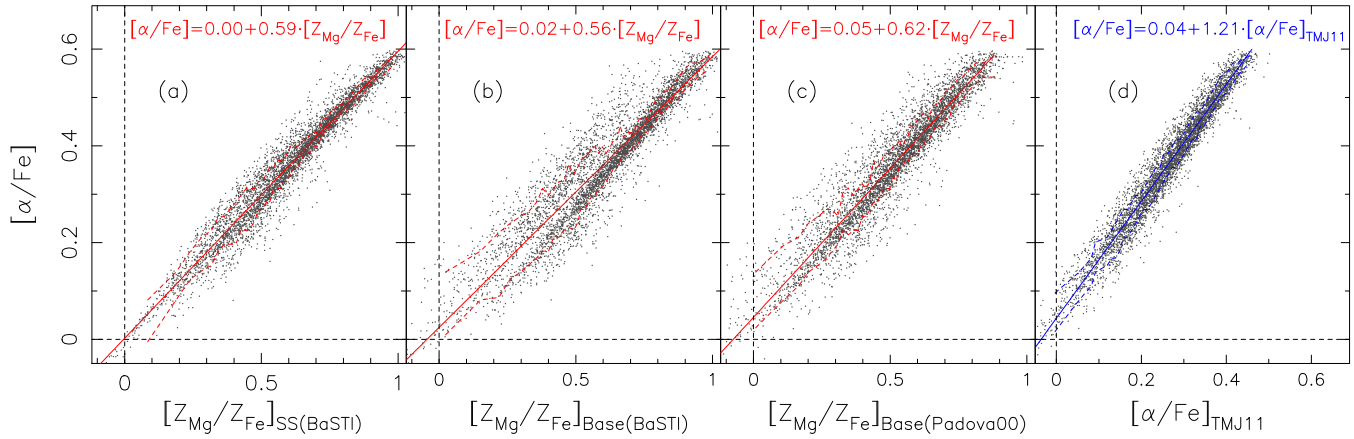

Figure 30. The 'true' [α/Fe], as estimated by our new models (see the text), is compared to different proxies for [α/Fe] (panels a–c), and the [α/Fe] estimated with the TMJ11 models (panel d). We compare [α/Fe] to the proxy for scaled-solar (a), base-BaSTI (b) and base-Padova (c) models. For each panel, grey dots correspond to a sample of 4671 ETGs selected from the SPIDER sample (see the text), solid curves are the best-fitting lines to the data (using [α/Fe] as dependent variable in the fitting), dashed curves are the $\pm 1\sigma$ scatter around the median trends, while horizontal and vertical dashed lines mark the values of zero on the *x*- and *y*-axes. The scatter in [α/Fe] around the best-fitting lines amounts to 0.025, 0.05, 0.04 and 0.025 dex for panels (a) to (d), respectively.

and the latter from ∼0 to ∼0.05. Note also that the scatter around the proxy – [α/Fe] best-fitting lines is smallest for our scaled-solar models (∼0.025 dex in [α/Fe]), and increases to ∼0.04 dex for $[Z_{Mg}/Z_{Fe}]_{Base(Padova00)}$, and to ∼0.05 dex for $[Z_{Mg}/Z_{Fe}]_{Base(BaSTI)}$. The scatter is largest for the base-BaSTI models because of a prominent tail of objects having too low $[Z_{Mg}/Z_{Fe}]_{Base(BaSTI)}$ at given [α/Fe] in panel (b) (relative to panel a) of Fig. 30. The origin of this tail can be understood through Fig. 31, comparing the dependence of Mg*b* and Fe3 line strengths on total metallicity for different non-α-enhanced models. While the slope of the Fe3–[*M*/H] relation turns out to be approximately the same for all models, the behaviour of Mg*b* versus [*M*/H] is more model dependent, with the shallowest slope for the base-BaSTI models. As seen by comparing the green and black curves in the top panel of Fig. 31, at high [*M*/H] ($\gtrsim$0) one obtains similar $[M/H]_{Mgb}$ and $[M/H]_{Fe3}$ estimates when using either base-BaSTI or scaled-solar models. In contrast, at low [*M*/H], the $[M/H]_{Mgb}$ estimate is always lower (for given Mg*b* line strength) for base-BaSTI than scaled-solar models, leading to lower $[Z_{Mg}/Z_{Fe}]$s, explaining the tail of low proxy values in panel (b), relative to panel (a), of Fig. 30.

Fig. 30, panel (d), also shows that a tight correlation exists between the 'true' [α/Fe] estimates from our models and from the TMJ11 α-enhanced models, with a scatter of only 0.025 dex in $[\alpha/Fe]_{TMJ11}$. Note that the slope of the best-fitting relation between the two estimates of [α/Fe] is larger than one (∼1.2), implying that using our models leads to values of [α/Fe] larger than those from the TMJ11 models.

In summary, we find that relative estimates of [Mg/Fe], with accuracy <0.05 dex, may not require (for most applications) stellar population models with enhanced [α/Fe], while absolute estimates of [α/Fe] require 'truly' α-enhanced models. However, absolute estimates of [α/Fe] are affected by differences in the adopted stellar populations models (consistent with what found, e.g. by Conroy et al. 2014).

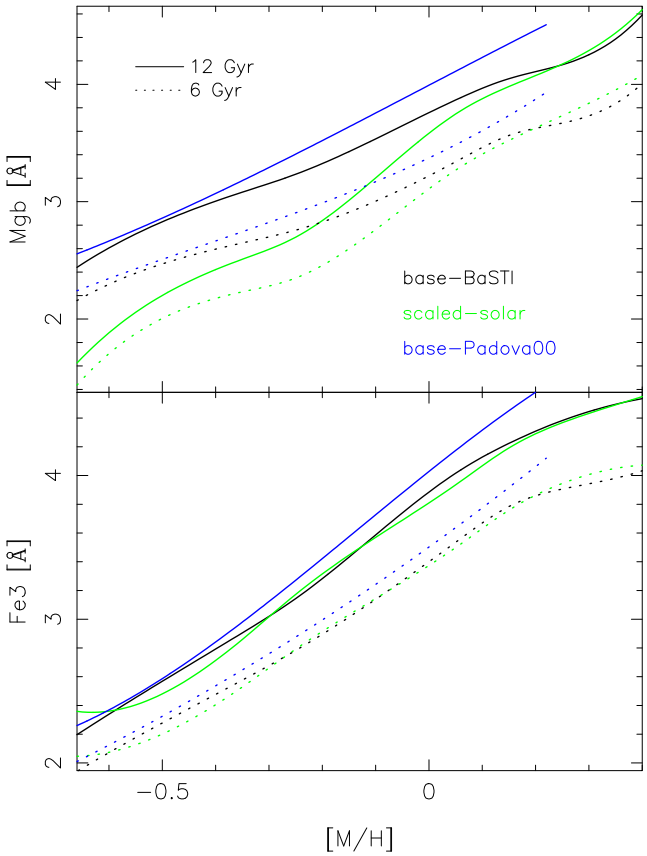

Figure 31. Behaviour of Mg*b* (top) and Fe3 (bottom) as a function of total metallicity for the base-BaSTI, scaled-solar, and base-Padova models, as labelled in the upper panel. Solid and dotted curves correspond to ages of 12 and 6 Gyr, respectively, typical for the spectra of ETGs used for Fig. 30.

9 THE MILES WEB PAGE

In an effort to facilitate the use of our models, we have integrated these new predictions into our dedicated website (http://miles.iac.es). The main new feature is the ability to compute spectra for more complex SFHs, with varying IMF and α-enhancement. As for the current set of models, our website will deliver spectra at the desired instrumental setup decided by the user, as well as provide line strength and colour predictions among other observables.

9.1 Complex models with multiple bursts

The complex SFHs used for Fig. 25 have been obtained through the SFH facility implemented in the MILES website. This tool allows the user to retrieve the model spectrum corresponding to a given SFH, having an arbitrary number of bursts, with different ages, metallicities and burst strengths (see section 3 in Ricciardelli et al. 2012). The SFH required by the user can either follow some parametric description or be user-defined. For the parametric SFHs, four different cases are allowed: multiple bursts (analogous to the user-defined case but limited to five bursts only), a truncated SFH, in which the star formation rate (SFR) is assumed to be constant between the time of formation and truncation, an exponential SFH and an exponential plus bursts, where up to five bursts can be added on top of the exponential SFR. The user-defined SFHs are designed to handle complex SFHs, with an arbitrary number of bursts permitted. In the new web implementation, the user-defined SFH has been upgraded to include also variable IMF slope and α-enhancement.

Given the mass fraction, the metallicity, the IMF slope and the α-enhancement at different ages, the tool computes the corresponding SED, S_λ, according to

$$S_\lambda = \sum_{i=1}^{N_b} f_{m_i} S_\lambda(t_i, [M/H]_i, [\alpha/Fe]_i, \Phi(\Gamma_i), I_{\alpha_i}), \quad (7)$$

where N_b is the number of input bursts, f_{m_i} is the fraction of mass formed in the ith burst, at age t_i, with metallicity $[M/H]_i$, IMF slope Γ_i (or Γ_{b_i} in the case of a bimodal IMF) and enhancement $[\alpha/Fe]_i$, which in this study can be $+0.0$ and $+0.4$. $S_\lambda(t_i, [M/H]_i, [\alpha/Fe]_i, \Phi(\Gamma_i), I_{\alpha_i})$ is the ith SSP spectrum, which is computed with an isochrone, I_{α_i}, with similar α-enhancement.

10 SUMMARY

This paper is the second, and last, of a series where we present evolutionary stellar population synthesis models based on the empirical library MILES (Sánchez-Blázquez et al. 2006a; Cenarro et al. 2007b), which represents a significant improvement over previous empirical libraries. In the first paper (Paper I), we developed 'base models', employing the Padova00 scaled-solar isochrones (Padova00) and MILES to predict spectra of intermediate- and old-aged stellar populations in the range λλ 3540.5–7409.6 Å, at moderately high resolution (FWHM=2.51 Å). Following the abundance pattern of the solar neighbourhood, the computed model SEDs are enhanced in α-elements at low metallicity, whereas around solar metallicity these predictions are approximately scaled-solar. The base models are therefore inconsistent at low metallicities. In this work, we further developed our models based on the MILES library, as well as theoretical stellar spectral libraries used in a differential way, to provide self-consistent predictions at all metallicities. We emphasize that our models can be regarded as self-consistent in the sense that both ingredients, the theoretical stellar spectra and the isochrones are computed with the same overall α-enhancement. We summarize below these model developments and results.

(i) We computed fully theoretical models based on the stellar library of Coelho et al. (2005), with its extension to cool stars of Coelho et al. (2007), to obtain SSPs-based differential spectral corrections (Cervantes et al. 2007; Walcher et al. 2009). We employed the BaSTI isochrones (Pietrinferni et al. 2004, 2006), calculated with similar $[\alpha/Fe]$ abundance ratios to the stellar atmospheres, converted to the observational plane using extensive empirical photometric stellar libraries, mostly from Alonso et al. (1996, 1999). To improve the metallicity coverage around the solar value, we computed a new set of BaSTI isochrones with metallicity $Z = 0.024$ ($[M/H] = +0.15$). The obtained theoretical differential corrections are applied to the model SEDs computed with MILES, taking into account the [Mg/Fe] determinations of the library stars of Milone et al. (2011). Therefore, at solar metallicity, the scaled-solar models are truly scaled-solar and fully based on MILES, whereas for the α-enhanced models, we apply the differential corrections to the model SEDs computed with MILES. At low metallicities, the opposite is true; the MILES library is intrinsically α-enhanced and we correct the model SEDs using differential corrections to obtain scaled-solar SEDs at low metallicity. We therefore compute self-consistent models for two abundance ratio values: $[\alpha/Fe] = 0.0$ and $[\alpha/Fe] = +0.4$.

(ii) In addition to the scaled-solar and α-enhanced models, and to the models we published in Paper I using the Padova00 isochrones, we also computed base models employing the BaSTI scaled-solar isochrones.

(iii) We have assessed the quality of the new models, establishing the parameter space where the models are safe. The new models cover the metallicity range $-2.3 \leq [M/H] \leq +0.4$, although the model predictions, and in particular those of the scaled-solar and alpha-enhanced models, are generally safe within the range $-1.49 \leq [M/H] \leq +0.26$ (within the constraints listed in Table 2 and shown in Figs 6 and 7). Also, the spectral range blueward of 3800 Å is unsafe for the scaled-solar models with subsolar metallicities and for the α-enhanced models with solar and higher metallicities. We strongly suggest the interested user of these predictions to read the notes on the unsafe model parameter ranges that we provide in Tables 1 and 2. It is particularly important to do so when the obtained fits to the data fall within these unsafe ranges.

(iv) We provide SSP spectra for a suite of IMF shapes: single power-law (unimodal), low-mass ($\lesssim 0.5$ $M_\odot$) tapered IMF (bimodal) as defined in Vazdekis et al. (1996, 2003) and the Kroupa Universal and revised IMFs of Kroupa (2001). For the unimodal and bimodal IMFs, we have varied the logarithmic slope from 0.3 (top-heavy) to 3.3 (very bottom-heavy). A unimodal shape with slope 1.3 matches approximately the Salpeter IMF, whereas a bimodal shape with the same slope is very close to the Kroupa Universal IMF. The predictions for the models adopting a unimodal IMF are safe for slopes smaller than 2.3, taking into account the above constraints.

(v) We have characterized the behaviour of the newly synthesized SSP model spectra. We find that, at constant total metallicity, $[M/H]$, the α-enhanced models, which have lower iron content and therefore have lower opacities, show an excess of flux blueward of ∼4500 Å with respect to the scaled-solar models. Besides this excess in flux, the α-enhanced and the scaled-solar models differ significantly in prominent features that are mainly related to the Ca II H–K and several CN and CH molecular absorptions. Both the blue flux excess and the differences seen in these features, which mostly originate in the stellar atmospheres, increase with increasing age and increasing metallicity. In comparison to the effects of the stellar spectra, the effects of the isochrones are of second order, and mostly impact on the continuum over the whole spectral range covered by the models, confirming the results by Coelho et al. (2007).

(vi) We confirm previous results that the combined [MgFe] and [MgFe]′ are virtually insensitive to the $[\alpha/Fe]$ abundance ratio, and therefore are suitable for measuring the total metallicity.

(vii) We also confirm previous findings that the Hγ and Hδ Balmer-line indices are more sensitive to [α/Fe] than Hβ. However, we show that such sensitivity is due to the pseudo-continua employed for the higher order Balmer index definitions, which are placed on relevant features within the blue flux excess of the α-enhanced models. The narrower the Balmer index definition, the lesser the sensitivity to [α/Fe].

(viii) As expected, the Fe-dominated indices, such as Fe 4383, Fe 5015, Fe 5270 and Fe 5335 are weaker, and Mg*b* stronger in the α-enhanced models. This behaviour becomes more pronounced with increasing age and increasing metallicity. Such trends do not apply to Mg_1 and Mg_2, which are stronger in the scaled-solar models, as these indices show a greater sensitivity to carbon than [α/Fe]. These and all the other non-α elements are depleted with respect to the scaled-solar models. A similar behaviour is seen for C_2 4668 and CN_2 (and CN_1), which depend on C and N abundances, respectively. Also in our models, the NaD index behaves as the Fe-dominated indices.

(ix) We also see that at ages less than ∼0.1 Gyr, there is a significant increase in the strengths of various lines, most noticeably for the IMF-sensitive indices. This is as a consequence of the influence of supergiant stars at these young ages. Among the IMF indicators we find that, unlike TiO_1, the TiO_2 index is almost insensitive to [α/Fe], in good agreement with other authors. We also find that the TiO_2 index, and other indices that show little sensitivity to age when employing a standard IMF slope (i.e 1.3), become more sensitive to this parameter for bottom-heavier IMFs.

(x) The base models, which approximately follow the abundance pattern of the Milky Way (MILES) stars, show index values that are more similar to those of the α-enhanced models at low metallicities ($[M/H] \lesssim -0.4$), despite the fact that the employed isochrones are scaled-solar. On the other hand, at high metallicities the base models provide index values that are very close to the scaled-solar ones. In general, the indices of the base models computed with BaSTI and Padova00 isochrones are very similar, with the line strengths obtained with BaSTI being slightly larger for the Balmer lines and slightly smaller for the metallicity indices. Therefore, for a given data set, somewhat older ages and higher metallicities would be inferred from the BaSTI-based models than from Padova00-based models.

(xi) A similar behaviour is seen for the colours, with the models based on BaSTI being bluer than those based on Padova00. Overall, the agreement is good for the old stellar populations. For ages where the AGB contribution is more significant, we find the larger discrepancies as a result of the varying descriptions for this evolutionary phase.

(xii) We use the base models as a reference for assessing the behaviour of the scaled-solar and α-enhanced colours. We find that the α-enhanced models are bluer in the blue, by ∼0.2 mag in $u-g$ and ∼0.05 mag in $g-r$ for old populations, and redder in the red, by ∼0.02 mag in $r-i$, with respect to the base models. The best agreement between the base and α-enhanced models is reached at low metallicities. On the other hand, for the scaled-solar models, the best agreement is reached at high metallicities.

(xiii) We compared our newly synthesized SSP spectra and line strengths with other models in the literature. In particular, we find that there is an overall agreement with the SSP spectra of the CvD12 models. We find that the overall effect of increasing [α/Fe] is similar to our models, although there are significant differences in the relative effect on different spectral features. We also compared our line-strength indices with the predictions of the TMJ11 and S07 models. As expected, we find significant offsets among the predictions of the various models, even at scaled-solar abundance. At fixed [Fe/H], the amount of increase of the Mg*b* index is larger, by ∼0.2 Å, for our models and the TMJ11 models, relative to the S07 and CvD12 models. The iron lines show a mild dependence on [α/Fe], but we find that differences exist among the various models. Whereas all the models agree on Fe 5335 and Fe 4383, which decrease with [α/Fe] (although with varying sensitivities), the Fe 5270 and Fe 5015 indices are more model dependent. Although differences remain among predictions from different models on the dependence of Balmer lines on [α/Fe], our new models agree well with expectations from most models compared here, i.e. that Hβ remains constant (as in S07 and TMJ11), $H\gamma_F$ increases (as in CvD12 and S07) and $H\delta_F$ increases (for all models) with [α/Fe]. Finally, our models agree remarkably well with CvD12 models on the expected sensitivity of commonly used IMF-sensitive features (TiO1, TiO2, and NaD) to [α/Fe].

(xiv) We compared the line strengths of the new models with GGC data. We find good agreement with [Mg/Fe] determinations obtained from individual stars in these clusters. The clusters with the highest metallicities fall in between the α-enhanced and the scaled-solar model predictions in the Mg*b*–⟨Fe⟩ index–index diagram. At very low metallicities, the differences between the index values obtained from the various models, i.e. base, α-enhanced and scaled-solar, are far less prominent. This allows us to conclude that the base models are also suitable for studying the line strengths of such metal-poor stellar systems. We find that all the models fit the $C_2$4668 index very well, but not CN_2 (CN_1). This is possibly related to the general presence of two stellar generations in GCs, the first with a canonical α-enhanced heavy element distribution and the second characterized by an anticorrelated CN–ONa abundance pattern.

(xv) We match reasonably well the $u-g$ versus $g-r$ and $r-i$ versus $g-r$ optical colour–colour diagrams of luminous SDSS ETGs simultaneously if we use appropriate combinations of α-enhanced models and a varying IMF. Note that this is not possible using base models with a standard IMF. This result is in good agreement with our previous results obtained with the MIUSCAT base models (Ricciardelli et al. 2012).

(xvi) We obtain good fits to ETG spectra with varying mass and α-enhancement. The SSP spectra are able to match the Fe- and Mg-dominated features with great accuracy. However, we also find that in order to recover the α-enhancement with this fitting technique it is necessary to perform the fit within a spectral range that encompasses these α-enhancement sensitive features. Within a larger spectral range, this information is in part washed out.

(xvii) The model grids obtained when plotting $H\beta_o$ against Mg*b*, ⟨Fe⟩ and [MgFe] indices, which are sensitive to Mg, Fe and total metallicity [M/H], respectively, provide consistent age/metallicity solutions for the most massive galaxies.

(xviii) Using SDSS ETG spectra stacked by velocity dispersion, we find that different Balmer-line indices (and also different definitions of the same line) provide different estimates of the age for old stellar populations. Neither the α-enhanced models nor models with varying IMF are able to solve these discrepancies, which might be due to different effects such as a variation of abundance ratios of specific chemical species in the stellar atmospheres, and/or more complex SFHs than pure SSPs. In addition, these differences may originate in the theoretical stellar spectra used to obtain the differential corrections employed to synthesize the α-enhanced SSP spectra.

(xix) Using ∼5000 high-quality SDSS ETG galaxy spectra, with S/N > 25 per Å, we find a linear relation between a proxy for the abundance obtained using solely scaled-solar models, $[Z_{Mg}/Z_{Fe}]_{SS}$,

and the [Mg/Fe] derived when employing our new models with varying abundance. We obtain the following relation:

$$[\mathrm{Mg/Fe}] = 0.59[Z_{\mathrm{Mg}}/Z_{\mathrm{Fe}}]_{\mathrm{SS(BaSTI).}} \quad (8)$$

Very similar relations are obtained when using the base model grids, either based on BaSTI or Padova00 isochrones. The method consists of plotting a good age indicator (such as e.g. Hβ or Hβ_{o}, or any other approach that provides us a reliable age estimate) against Mg*b*, and against $\langle$Fe$\rangle$, using a scaled-solar model grid as a reference. The difference in metallicity obtained from these two diagrams, i.e. the proxy $[Z_{\mathrm{Mg}}/Z_{\mathrm{Fe}}]$, which is non-zero when the object is [Mg/Fe] enhanced, is appropriate for estimating the 'true' abundance, without making any use of α-enhanced models.

All these models can be retrieved from the MILES web page at http://miles.iac.es. The link includes a user-friendly web-tool facility that, among other things, allows for the construction of SED models for a variety of SFHs. This includes a user-defined SFH, where it is possible to combine bursts with varying IMFs and [α/Fe] abundance ratios.

ACKNOWLEDGEMENTS

We are indebted to the Padova group for making their isochrone calculations available to us. We are grateful to A. de C. Milone for providing us with his [Mg/Fe] estimates for the stars of the MILES library before publication. We also are grateful to H.-S. Kim, J. Cho, R. M. Sharples and S.-J. Yoon, who provided us with GGC line-strength measurements prior to publication. We are grateful to B. Barbuy, J. L. Cervantes, I. G. de la Rosa, M. Koleva, R. Peletier and A. Sansom for very useful discussions. We thank the referee H.-C. Lee for a careful reading of the manuscript and for very valuable clarifications that helped us to improve the manuscript. We also would like to thank J. A. Perez Prieto for helping us in the construction of the web page for the models. The MILES library was observed at the INT on the island of La Palma, operated by the Isaac Newton Group at the Observatorio del Roque de los Muchachos of the Instituto de Astrofísica de Canarias. This research has made an extensive use of the SIMBAD data base and VizieR catalogue access tool (both operated at CDS, Strasbourg, France), the NASA's Astrophysics Data System Article Service. We made use of data retrieved from the Sloan Digital Sky Survey archives (http://www.sdss.org). Funding for the SDSS and SDSS-II has been provided by the Alfred P. Sloan Foundation, the Participating Institutions, the National Science Foundation, the US Department of Energy, the National Aeronautics and Space Administration, the Japanese Monbukagakusho, the Max Planck Society and the Higher Education Funding Council for England. PC acknowledges the financial support by FAPESP via project 2008/58406-4 and fellowship 2009/09465-0. JFB acknowledges support from the Ramón y Cajal programme by the Spanish Ministry of Economy and Competitiveness (MINECO). This work has been supported by the Programa Nacional de Astronomía y Astrofísica of MINECO, under grants AYA2013-48226-C3-1-P, AYA2013-48226-C3-2-P, AYA2013-48226-C3-3-P and by the Generalitat Valenciana under grant PROMETEOII2014-069.

REFERENCES

Alexander D. R., Ferguson J. W., 1994, ApJ, 437, 879
Alonso A., Arribas S., Martínez-Roger C., 1995, A&A, 297, 197
Alonso A., Arribas S., Martínez-Roger C., 1996, A&A, 313, 873
Alonso A., Arribas S., Martínez-Roger C., 1999, A&AS, 140, 261
An D. et al., 2009, ApJ, 700, 523
Arimoto N., 1986, in Leitherer U., Fritze-von-Alvensleben U., Huchra J., eds. Proc. ASP Conf. Ser. Vol. 98, From Stars to Galaxies: The Impact of Stellar Physics on Galaxy Evolution. Astron. Soc. Pac., San Francisco, p, 287
Arimoto N., Yoshii Y., 1986, A&A, 164, 260
Barbuy B., Castro S., Ortolani S., Bica E., 1992, A&A, 259, 607
Barbuy B., Perrin M. N., Katz D., Coelho P., Cayrel R., Spite M., Vaní Veer-Menneret C., 2003, A&A, 404, 661
Beasley M. A., Brodie J. P., Strader J., Forbes D. A., Proctor R. N., Barmby P., Huchra J. P., 2004, AJ, 128, 1623
Behr B. B., 2003, ApJS, 149, 67
Bertelli G., Bressan A., Chiosi C., Fagotto F., Nasi E., 1994, A&AS, 106, 275
Bertone E., Buzzoni A., Chávez M., Rodríguez-Merino L. H., 2008, A&A, 485, 823
Bessell M. S., Brett J. M., Wood P. R., Scholz M., 1989, A&AS, 77, 1
Bessell M. S., Brett J. M., Scholz M., Wood P. R., 1991, A&AS, 89, 335
Blakeslee J. P., Vazdekis A., Ajhar E. A., 2001, MNRAS, 320, 193
Bressan A., Chiosi C., Fagotto F., 1994, ApJS, 94, 63
Brodie J. P., Huchra J. P., 1991, ApJ, 379, 157
Bruzual G., 1983, ApJ, 273, 105
Bruzual G., Charlot S., 2003, MNRAS, 344, 1000
Burstein D., Faber S. M., Gaskell C. M., Krumm N., 1984, ApJ, 287, 586
Buser R., Kurucz R. L., 1978, A&A, 70, 555
Buzzoni A., 1995, ApJS, 98, 69
Buzzoni A., Bertone E., Chávez M., Rodríguez-Merino L. H., 2009, in Chávez D., Bertone E., González-Delgado R., Rodríguez-Merino L. H., eds, New Quests in Stellar Astrophysics II. Ultraviolet Properties of Evolved Stellar Populations. Springer-Verlag, Berlin, p. 263.
Cannon R. D., Croke B. F. W., Bell R. A., Hesser J. E., Stathakis R. A., 1998, MNRAS, 298, 601
Cantiello M., Raimondo G., Brocato E., Capaccioli M., 2003, AJ, 125, 2783
Cappellari M., Emsellem E., 2004, PASP, 116, 138
Carretero C., Vazdekis A., Beckman J., Sánchez-Blázquez P., Gorgas J., 2004, ApJ, 609, L45
Carretero C., Vazdekis A., Beckman J., 2007, MNRAS, 375, 1025
Carretta E., Cohen J. G., Gratton R. G., Behr B. B., 2001, AJ, 122, 1469
Cassisi S., 2004, in Kurtz D. W., Pollard K., eds, ASP Conf. Ser. Vol. 310, IAU Colloq. 193: Variable Stars in the Local Group. Astron. Soc. Pac., San Francisco, p. 489
Cassisi S., Salaris M., 2013, Old Stellar Populations: How to Study the Fossil Record of Galaxy Formation. Wiley-VCH, Berlin
Cassisi S., Castellani V., Ciarcelluti P., Piotto G., Zoccali M., 2000, MNRAS, 315, 679
Cassisi S., Salaris M., Castelli F., Pietrinferni A., 2004, ApJ, 616, 498
Cassisi S., Mucciarelli A., Pietrinferni A., Salaris M., Ferguson J., 2013, A&A, 554, A19
Castelli F., Kurucz R. L., 2003, in Piskunov N., Weiss W. W., Gray D. F., eds, Proc. IAU Symp. 210, Modelling of Stellar Atmospheres. Astron. Soc. Pac., San Francisco, p. A20
Cayrel R., Perrin M., Barbuy B., Buser R., 1991, A&A, 247, 108
Cenarro A. J., Cardiel N., Gorgas J., Peletier R. F., Vazdekis A., Prada F., 2001a, MNRAS, 326, 959
Cenarro A. J., Gorgas J., Cardiel N., Pedraz S., Peletier R. F., Vazdekis A., 2001b, MNRAS, 326, 981
Cenarro A. J., Gorgas J., Cardiel N., Vazdekis A., Peletier R. F., 2002, MNRAS, 329, 863
Cenarro A. J., Gorgas J., Vazdekis A., Cardiel N., Peletier R. F., 2003, MNRAS, 339, L12
Cenarro A. J., Cardiel N., Vazdekis A., Gorgas J., 2009, MNRAS, 396, 1895
Cenarro A. J., Beasley M. A., Strader J., Brodie J. P., Forbes D. A., 2007a, AJ, 134, 391
Cenarro A. J. et al., 2007b, MNRAS, 374, 664
Cervantes J. L., Vazdekis A., 2009, MNRAS, 392, 691
Cervantes J. L., Coelho P., Barbuy B., Vazdekis A., 2007, in Vazdekis A., Peletier R., eds, Proc. IAU Symp. 241, Stellar Populations as Building Blocks of Galaxies. Cambridge Univ. Press, Cambridge, p. 167

Cezario E., Coelho P., Alves-Brito A., Forbes D. A., Brodie J. P., 2013, A&A, 549, 60
Chen Y. P., Trager S. C., Peletier R. F., Lancon A., Vazdekis A., Prugniel P., Silva D. R., Gonneau A., 2014, A&A, 565, 117
Chilingarian I. V., Prugniel P., Sil'Chenko O. K., Koleva M., 2007, in Vazdekis A., Peletier R. eds. Proc. IAU Symp. 241, Stellar Populations as Building Blocks of Galaxies. Cambridge Univ. Press, Cambridge, p. 175
Chung C., Yoon S.-J., Lee S.-Y., Lee Y.-W., 2013, ApJS, 204, 3
Cid Fernandes R., Mateus A., Sodré L., Stasińska G., Gomes J. M., 2005, MNRAS, 358, 363
Coelho P., 2014, A&A, 440, 1027
Coelho P., Barbuy B., Perrin M.-N., Idiart T., Schiavon R. P., Ortolani S., Bica E., 2001, A&A, 376, 136
Coelho P., Barbuy B., Melendez J., Schiavon R., Castilho B., 2005, A&A, 443, 735
Coelho P., Bruzual G., Charlot S., Weiss A., Barbuy B., Ferguson J. W., 2007, MNRAS, 382, 498
Coelho P., Percival S., Salaris M., 2011, ApJ, 734, 72
Conroy C., 2013, ARA&A, 51, 393
Conroy C., Gunn J. E., 2010, ApJ, 712, 833
Conroy C., van Dokkum P., 2012a, ApJ, 747, 69 (CvD12)
Conroy C., van Dokkum P., 2012b, ApJ, 760, 61
Conroy C., Graves G., van Dokkum P., 2014, ApJ, 780, 33
Cordier D., Pietrinferni A., Cassisi S., Salaris M., 2007, AJ, 133, 468
Covino S., Galletti S., Pasinetti L. E., 1995, A&A, 443, 735
Cristallo S., Straniero O., Lederer M. T., Aringer B., 2007, ApJ, 667, 489
Cushing M. C., Raynier J. T., Vacca W. D., 2005, ApJ, 623, 1115
de la Rosa I. G., de Carvalho R. R., Vazdekis A., Barbuy B., 2007, AJ, 133, 330
de Laverny P., Recio-Blanco A., Worley C. C., Plez B., 2012, A&A, 544, 126
Dotter A., Chaboyer B., Jevremović D., Kostov V., Baron E., Ferguson J. W., 2008, ApJS, 178, 89
Edvardsson B., Andersen J., Gustafsson B., Lambert D. L., Nissen P. E., Tomkin J., 1993, A&AS, 102, 603
Faber S. M., Friel E. D., Burstein D., Gaskell G. M., 1985, ApJS, 57, 711
Falcón-Barroso J., Balcells M., Peletier R., Vazdekis A., 2003a, A&A, 405, 455
Falcón-Barroso J., Peletier R., Vazdekis A., Balcells M., 2003b, ApJ, 588, L17
Falcón-Barroso J., Sánchez-Blázquez P., Vazdekis A., Ricciardelli E., Cardiel N., Cenarro A. J., Gorgas J., Peletier R. F., 2011, A&A, 532, 95
Ferreras I., La Barbera F., de la Rosa I. G., Vazdekis A., de Carvalho R. R., Falcón-Barroso J., Ricciardelli E., 2013, MNRAS, 429, L15
Fioc M., Rocca-Volmerange B., 1997, A&A, 326, 950
Fluks M. A., Plez B., Thé P. S., de Winter D., Westerlund B. E., Steenman H. C., 1994, A&AS, 105, 311
Frémaux J., Kupka F., Boisson C., Joly M., Tsymbal V., 2006, A&A, 449, 109
Fritze-Von Alvensleben U. A., Gerhard O. E., 1994, A&A, 285, 751
Fukugita M., Shimasaku K., Ichikawa T., 1995, PASP, 107, 945
Gibson B. K., Madgwick D. S., Jones L. A., Da Costa G. S., Norris J. E., 1999, AJ, 118, 1268
Girardi L., Bressan A., Bertelli G., Chiosi C., 2000, A&AS, 141, 371 (Padova00)
González-Delgado R. Cerviño M., Martins L. P., Leitherer C., Hauschildt P. H., 2005, MNRAS, 357, 945
Gorgas J., Faber S. M., Burstein D., Gonzalez J. J., Courteau S., Prosser C., 1993, ApJS, 86, 153
Gorgas J., Cardiel N., Pedraz S., González J. J., 1999, ApJS, 139, 29
Gratton R. G., Carretta E., Bragaglia A., 2012, ARA&A, 20, 50
Graves G. J., Schiavon R. P., 2008, ApJS, 177, 446
Grevesse N., Sauval A. J., 1998, Space Sci. Rev., 85, 161
Guiderdoni B., Rocca-Volmerange B., 1987, A&A, 186, 1
Hayes D. S., 1985, in Hayes D. S., Pasinetti L. E., Philip A. G. D., eds, Proc. IAU Symp. 111, Calibration of Fundamental Stellar Quantities. Dordrecht, Reidel, p. 225
Iben I., Truran J. W., 1978, ApJ, 220, 980
Jeong H., Sukyoung Y. K., Kyeong J., Sarzi M., Sung E., Oh K., 2013, ApJS, 208, 7
Johansson J., Thomas D., Maraston C., 2012, MNRAS, 421, 1908
Johnson C. I., Kraft R. P., Pilachowski C. A., Sneden C., Ivans I. I., Benman G., 2005, PASP, 117, 1308
Jones L. A., 1999, PhD thesis, Univ. North Carolina
Kacharov N., Koch A., McWilliam A., 2013, A&A, 554, A81
Kholopov P. N. et al., 1998, The Combined General Catalogue of Variable Stars 4th Edition. Sternberg Astronomical Institute, Moscow (http://vizier.u-strasbg.fr/viz-bin/VizieR?-source=II%2F214)
Kim Y., Demarque P., Yi S., Alexander D. R., 2002, ApJS, 143, 499
Kirby E. N., 2011, PASP, 123, 531
Kodama T., Arimoto N., 1997, A&A, 320, 41
Koleva M., Vazdekis A., 2012, A&A, 538, 143
Koleva M., Prugniel P., Bouchard A., Wu Y., 2009, A&A, 501, 1269
Korn A. J., Maraston C., Thomas D., 2005, A&A, 438, 685
Kraft R. P., Sneden C., Smith G. H., Shetrone M. D., Fulbright J., 1998, AJ, 115, 1500
Kroupa P., 2001, MNRAS, 322, 231
Kuntschner H., 2000, MNRAS, 315, 184
Kuntschner H., Ziegler B. L., Sharples R. M., Worthey G., Fricke K. J., 2002, A&A, 395, 761
Kuntschner H. et al., 2006, MNRAS, 369, 497
Kurucz R. L., 1970, SAO Special Report, 309
Kurucz R. L., 1993, in Kurucz R. L., ed., SYNTHE Spectrum Synthesis Programs and Line Data. Smithsonian Astrophysical Observatory, Cambridge, MA
La Barbera F., Ferreras I., Vazdekis A., de la Rosa I. G., de Carvallo R. R., Trevisan M., Falcón-Barroso J., Ricciardelli E., 2013, MNRAS, 433, 3017
Le Borgne J.-F. et al., 2003, A&A, 402, 433
Le Borgne J.-F., Rocca-Volmerange B., Prugniel P., Lancon A., Fioc M., Soubiran C., 2004, A&A, 425, 881
Lee H.-C., Worthey G., 2005, ApJS, 160, 176
Lee H.-C., Yoon S.-J., Lee Y.-W., 2000, AJ, 120, 176
Lee H.-C. et al., 2009a, ApJ, 694, 902
Lee H.-C., Worthey G., Dotter A., 2009b, AJ, 138, 1442
Lee H.-C., Worthey G., Blakeslee J. P., 2010, ApJ, 710, 421
Leitherer C. et al., 1999, ApJS, 123, 3
Leitherer C., Ortiz-Otálvaro P. A., Bresolin F., Kudritzki R.-P., Lo Faro B., Pauldrach A. W. A., Pettini M., Rix S. A., 2010, ApJS, 189, 309
Lejeune T., Cuisinier F., Buser R., 1997, A&AS, 125, 229
Lejeune T., Cuisinier F., Buser R., 1998, A&AS, 130, 65
Liu M. C., Charlot S., Graham J. R., 2000, ApJ, 543, 644
Liu M. C., Graham J. R., Charlot S., 2002, ApJ, 564, 216
MacArthur L. A., 2005, ApJ, 623, 795
McWilliam A., 1997, ARA&A, 35, 503
McWilliam A., Matteucci F., Ballero S., Rich R. M., Fulbright J. P., Cescutti G., 2008, AJ, 136, 367
Maraston C., 1998, MNRAS, 300, 872
Maraston C., 2005, MNRAS, 362, 799
Maraston C., Strömbäck G., 2011, MNRAS, 418, 2785
Maraston C., Strömbäck G., Thomas D., Wake D. A., Nichol R. C., 2009, MNRAS, 394, L107
Marigo P., Girardi L., Bressan A., Groenewegen M. A. T., Silva L., Granato G. L., 2008, A&A, 482, 883
Mármol-Queraltó E., Cardiel N., Cenarro A. J., Vazdekis A., Gorgas J., Pedraz S., Peletier R. F., Sánchez-Blázquez P., 2008, A&A, 489, 885
Martins L. P., Coelho P., 2007, MNRAS, 381, 1329
Martins L. P., Delgado R. M. G., Leitherer C., Cerviño M., Hauschildt P., Coelho P., 2005, MNRAS, 358, 49
Mayya Y. D., 1997, ApJ, 482, L149
Mendel J. T., Proctor R. N., Forbes D. A., 2007, MNRAS, 379, 1618
Michielsen D. et al., 2008, MNRAS, 385, 1374
Milone A. de C., Sansom A. E., Sánchez-Blázquez P., 2011, MNRAS, 414, 1227

Munari U., Sordo R., Castelli F., Zwitter T., 2005, A&A, 442, 1127
Murphy T., Meiksin A., 2004, MNRAS, 351, 1430
Noël N. E. D., Greggio L., Renzini A., Carollo C. M., Maraston C., 2013, ApJ, 772, 58
Ocvirk P., Pichon C., Lancon A., Thiébaut E., 2006a, MNRAS, 365, 46
Ocvirk P., Pichon C., Lancon A., Thiébaut E., 2006b, MNRAS, 365, 74
Palacios A., Gebran M., Josselin E., Martins F., Plez B., Belmas M., Lébre A., 2010, A&A, 516, 13
Panter B., Heavens A. F., Jimenez R., 2003, MNRAS, 343, 1145
Peacock M. B., Zepf S. E., Maccarone T. J., Kundu A., 2011, ApJ, 737, 5
Peletier R., 1989, PhD thesis, Univ. Groningen
Percival S. M., Salaris M., Cassisi S., Pietrinferni A., 2009, ApJ, 690, 427
Pietrinferni A., Cassisi S., Salaris M., Castelli F., 2004, ApJ, 612, 168
Pietrinferni A., Cassisi S., Salaris M., Castelli F., 2006, ApJ, 642, 797
Pietrinferni A., Cassisi S., Salaris M., Percival S., Ferguson J. W., 2009, ApJ, 697, 275
Pietrinferni A., Cassisi S., Salaris M., Hidalgo S., 2013, A&A, 558, 46
Piotto G. et al., 2012, ApJ, 760, 39
Plez B., 1992, A&AS, 94, 527
Pols O. R., Tout C. A., Eggleton P. P., Han Z., 1995, MNRAS, 274, 964
Proctor R., Sansom A. E., 2002, MNRAS, 333, 517
Proctor R., Forbes D., Beasley M. A., 2004, MNRAS, 355, 1327
Prugniel P., Soubiran C., 2001, A&A, 369, 1048
Prugniel P., Soubiran C., Koleva M., Le Borgne D., 2007, preprint (astro-ph/0703658)
Raynier J. T., Cushing M. C., Vacca W. D., 2009, ApJS, 185, 289
Reimers D., 1977, A&A, 57, 395
Renzini A., 2006, ARA&A, 44, 141
Ricciardelli E., Vazdekis A. Cenarro A. J., Falcón-Barroso J., 2012, MNRAS, 424, 172
Rodgers A. W., Harding P., 1990, PASP, 102, 235
Rodríguez-Merino L. H., Chavez M., Bertone E., Buzzoni A., 2005, ApJ, 626, 411
Roediger J. C., Courteau S., Graves G., Schiavon R. P., 2014, ApJS, 210, 10
Rose J. A., 1985, AJ, 90, 1927
Rose J. A., 1994, AJ, 107, 206
Saglia R. P., Maraston M., Thomas D., Bender R., Colless M., 2002, ApJ, 579, L13
Salaris M., Weiss A., 1998, A&A, 335, 943
Salaris M., Groenewegen M., Weiss A., 2000, A&A, 355, 299
Salaris M., Weiss A., Cassarà L. P., Piovan L., Chiosi C., 2014, A&A, 565, A9
Salasnich B., Girardi L., Weiss A., Chiosi C., 2000, A&A, 361, 1023
Salpeter E. E., 1955, ApJ, 121, 161
Sánchez-Blázquez P., Gorgas J., Cardiel N., Cenarro J., González J. J., 2003, ApJ, 590, L91
Sánchez-Blázquez P. et al., 2006a, MNRAS, 371, 703
Sánchez-Blázquez P., Gorgas J., Cardiel N., González J. J., 2006b, A&A, 457, 787
Sánchez-Blázquez P., Gorgas J., Cardiel N., González J. J., 2006c, A&A, 457, 809
Sansom A. E, de Castro Milone A., Vazdekis A., Sánchez-Blázquez P., 2013, MNRAS, 435, 952
Sarzi M. et al., 2006, MNRAS, 366, 1151
Sbordone L., Bonifacio P., Castelli F., Kurucz R. L., 2004, Mem. Soc. Astron. Ital. Suppl., 5, 93
Sbordone L., Salaris M., Weiss A., Cassisi S., 2011, A&A, 534, A9
Schiavon R. P., 2007, ApJS, 171, 146 (S07)
Schiavon R. P., Barbuy B., Bruzual G., 2000, ApJ, 532, 453
Schiavon R. P., Faber S. M., Castilho B. V., Rose J. A., 2002, ApJ, 580, 850
Schiavon R. P., Rose J. A., Courteau S., MacArthur L. A., 2004, ApJ, 608, L33
Schiavon R. P., Rose J. A., Courteau S., MacArthur L., 2005, ApJS, 160, 163
Schiavon R. P., Caldwell N., Conroy C., Graves G. J., Strader J., MacArthur L. A., Courteau S., Harding P., 2013, ApJ, 776, L7
Serven J., Worthey G., Briley M. M., 2005, ApJ, 627, 754
Soubiran C., Girard P., 2005, A&A, 438, 139
Soubiran C., Katz D., Cayrel R., 1998, A&AS, 133, 221
Spiniello C., Trager S., Koopmans L. V. E., Chen Y. P., 2012, ApJ, 753, L32
Spiniello C., Trager S., Koopmans L. V. E., Conroy C., 2014, MNRAS, 438, 1483
Strader J., Brodie J. P., Schweizer F., Larsen S. S., Seitzer P., 2003, AJ, 125, 626
Takeda Y., Honda S., 2005, PASJ, 57, 65
Tantalo R., Chiosi C., 2004, MNRAS, 353, 917
Tantalo R., Chiosi C., Bressan A., 1998, A&A, 333, 419
Tantalo R., Chiosi C., Piovan L., 2007, A&A, 462, 481
Thomas D., Maraston C., Bender R., 2003a, MNRAS, 339, 897
Thomas D., Maraston C., Bender R., 2003b, MNRAS, 343, 279
Thomas D., Maraston C., Bender R., Mendes de Oliveira C., 2005, ApJ, 621, 673
Thomas D., Maraston C., Johansson R., 2011, MNRAS, 412, 2183 (TMJ11)
Tinsley B. M., 1980, Fundam. Cosm. Phys., 5, 287
Tojeiro R., Percival W. J., Heavens A. F., Jimenez R., 2011, MNRAS, 413, 434
Trager S. C., Worthey G., Faber S. M., Burstein D., González J. J., 1998, ApJS, 116, 1
Trager S. C., Faber S. M., Worthey G., González J. J., 2000, AJ, 119, 1645
Treu T., Schmidt K. B., Trenti M., Bradley L. D., Stiavelli M., 2013, ApJ, 775, L29
Tripicco M. J., Bell R. A., 1995, AJ, 110, 3035
Valdes F., Gupta R., Rose J. A., Singh H. P., Bell D. J., 2004, ApJS, 152, 251
VandenBerg D. A., Swenson F. J., Rogers F. J., Iglesias C. A., Alexander D. R., 2000, ApJ, 532, 430
VandenBerg D. A., Bergbusch P. A., Ferguson J. W., Edvardsson B., 2014, ApJ, 794, 72
Vassiliadis E., Wood P. R., 1993, ApJ, 413, 641
Vazdekis A., 1999, ApJ, 513, 224
Vazdekis A., Arimoto N., 1999, ApJ, 525, 144
Vazdekis A., Casuso E., Peletier R. F., Beckman J. E., 1996, ApJS, 106, 307
Vazdekis A., Peletier R. F., Beckman J. E., Casuso E., 1997, ApJS, 111, 203
Vazdekis A., Salaris M., Arimoto N., Rose J. A., 2001a, ApJ, 549, 274
Vazdekis A., Kuntschner H., Davies R. L., Arimoto N., Nakamura O., Peletier R., 2001b, ApJ, 551, L127
Vazdekis A., Cenarro A. J., Gorgas J., Cardiel N., Peletier R. F., 2003, MNRAS, 340, 1317
Vazdekis A., Sánchez-Blázquez P., Falcón-Barroso J., Cenarro A. J., Beasley M. A., Cardiel N., Gorgas J., Peletier R. F., 2010, MNRAS, 404, 1639 (Paper I)
Vazdekis A., Ricciardelli E., Cenarro A. J., Rivero-González J. G., Díaz-García L. A., Falcón-Barroso J., 2012, MNRAS, 424, 157
Wagenhuber J., 1996, PhD thesis, Techn. Univ. Mnchen
Wagenhuber J., Groenewegen M. A. T., 1998, A&A, 340, 183
Walcher C. J., Coelho P., Gallazzi A., Charlot S., 2009, MNRAS, 398, L44
Weiss A., Ferguson J. W., 2009, A&A, 508, 1343
Weiss A., Peletier R., Matteucci F., 1995, A&A, 296, 73
Wild V., Walcher C. J., Johansson P. H., Tresse L., Charlot S., Pollo A., Le Fevre O., de Ravel L., 2009, MNRAS, 395, 144
Worthey G., 1994, ApJS, 95, 107
Worthey G., 1998, PASP, 110, 888
Worthey G., Lee H.-C., 2011, ApJS, 193, 1
Worthey G., Ottaviani D. L., 1997, ApJS, 111, 377
Worthey G., Faber S. M., González J. J., 1992, ApJ, 398, 69
Worthey G., Faber S. M., Gonzalez J. J., Burstein D., 1994, ApJS, 94, 687
Worthey G., Ingermann B. A., Serven J., 2011, ApJ, 729, 148
Worthey G., Baitian T., Serven J., 2014, ApJ, 783, 20
Yamada Y., Arimoto N., Vazdekis A., Peletier R. F., 2006, ApJ, 637, 200
Zwitter T., Castelli F., Munari U., 2004, A&A, 417, 1055

This paper has been typeset from a TEX/LATEX file prepared by the author.